PL-TR-96-2237

OPTICAL CONTAMINATION AND SIGNATURES IN THE NEAR-SPACE ENVIRONMENT

J. A. Gardner
D. L. A. Rall
I. L. Kofsky

PhotoMetrics, Inc
4 Arrow Drive
Woburn, MA 01801-2067

30 September 1996

Final Report
18 June 1991-18 June 1996

Approved for public release; distribution unlimited

DTIC QUALITY INSPECTED 2

**PHILLIPS LABORATORY
DIRECTORATE OF GEOPHYSICS
AIR FORCE MATERIEL COMMAND
HANSCOM AIR FORCE BASE, MA 01731-3010**

19970218 070

"This technical report has been reviewed and is approved for publication"

EDMOND MURAD
Contract Manager

DANIEL H. KATAYAMA
Chief
Ionospheric Interactions Branch

CHARLES P. PIKE
Director
Ionospheric Effects Division

This report has been reviewed by the ESC Public Affairs Office (PA) and is releasable to the National Technical Information Service (NTIS).

Qualified requestors may obtain additional copies from the Defense Technical Information Center (DTIC). All others should apply to the National Technical Information Service (NTIS).

If your address has changed, if you wish to be removed from the mailing list, or if the addressee is no longer employed by your organization, please notify PL/TSB, 29 Randolph Road, Hanscom AFB, MA 01731-3010. This will assist us in maintaining a current mailing list.

Do not report copies of this report unless contractual obligations or notices on a specific document require that it be returned.

REPORT DOCUMENTATION PAGE

1. AGENCY USE ONLY (Leave Blank)	2. REPORT DATE 30 September 1996	3. REPORT TYPE AND DATES COVERED Final, 18 June 1991 - 18 June 1996

4. TITLE AND SUBTITLE	5. FUNDING NUMBERS
Optical Contamination and Signatures in the Near-Space Environment	PE 62101F PR 7601 TA 30 WU CP Contract No. F19628-91-C-0061

6. AUTHORS

J. A. Gardner
D. L. A. Rall
I. L. Kofsky

7. PERFORMING ORGANIZATION NAME(S) AND ADDRESS(ES)	8. PERFORMING ORGANIZATION REPORT NUMBER
PhotoMetrics, Inc. 4 Arrow Drive Woburn, MA 01801-2067	

8. SPONSORING/MONITORING AGENCY NAME(S) AND ADDRESS(ES)	10. SPONSORING/MONITORING AGENCY REPORT NUMBER
Phillips Laboratory 29 Randolph Road Hanscom AFB, MA 01731-3010 Contract Manager: Edmond Murad/GPID	PL-TR-96-2237

11. SUPPLEMENTARY NOTES

12a. DISTRIBUTION/AVAILABILITY STATEMENT	12b. DISTRIBUTION CODE
Approved for public release; distribution unlimited	

13. ABSTRACT (Maximum 200 words)

Research supporting the USAF Phillips Laboratory Spacecraft Interactions Branch (WSAI) mission to characterize the environment of spacecraft and the interactions of their effluents with the atmosphere is reported. The principal issues investigated are optical emissions associated with spaceborne and powered suborbital vehicles; excitative reactions between neutral and ionized aeronomic and thruster-associated species; and ultraviolet airglow, which besides providing critical information about thermospheric composition and transport degrades performance of surveillance systems. The work, done in collaboration with WSAI scientists between June 1991 and June 1996, is further documented in six earlier interim reports.

The principal optically-active gaseous effluents from Shuttle Orbiter are combustion products of its liquid bipropellant attitude- and orbit-controlling rocket motors (which DoD vehicles also use), and H_2O evaporated from its surfaces and/or released in bulk in connection with housekeeping. The emissions, which as scene foregrounds hinder and as targets assist surveillance, include electronic and vibrational bands of these species and chemiluminescence from their reactions with the low-density atmosphere; in addition the nearby gases attenuate atmospheric and astronomical radiations. Data on these glows were obtained from both onboard and a mountaintop station (the Air Force Maui Optical Site) by the "GLO" multichannel imaging spectrograph, several electronic array-detector cameras, and an infrared scanning spectrometer. GLO also surveyed the ~80-400 km altitude Earth limb between ~1200 and 11000Å, during several-10's-hr segments of four shuttle

14. SUBJECT TERMS		15. NUMBER OF PAGES 112
Spacecraft contamination Spacecraft optical signatures Thruster exhaust reactions	Thruster exhaust hydrodynamics Ion-neutral reactions Ultraviolet airglow	16. PRICE CODE

17. SECURITY CLASSIFICATION OF REPORT	18. SECURITY CLASSIFICATION OF THIS PAGE	19. SECURITY CLASSIFICATION OF ABSTRACT	20. LIMITATION OF ABSTRACT
UNCLASSIFIED	UNCLASSIFIED	UNCLASSIFIED	SAR

CLASSIFIED BY:

DECLASSIFY ON:

13. ABSTRACT (Continued)

missions that provided a range of latitude and local time distributions at these tangent intercepts. The unique terminator-following trajectory of STS-53 (GLO-1, December 1992) led to measurement of the concentrations of metal atoms and ions in the E- and lower F-region, along with the first simultaneous detection of a neutral trace species (Mg) and its ion; these altitude profiles apply in validating models of ionosphere dynamics and chemistry. GLO also verified that scattering of solar photons from minor component nitric oxide and photoelectron excitation of major species molecular nitrogen result in the most intense natural ultraviolet backgrounds/foregrounds from the daytime thermosphere.

Electronic images from the Air Force Maui Optical Site showed aluminized solid composite rocket engine exhaust producing both persisting visible wake trails and previously-undetected short wavelength infrared emission from its shock-like interaction with the oxygen atom-rich air near 110 km. The principal reactions studied in the laboratory were suprathermal charge and atom exchange between effluent species (H_2O and hydrazine compounds) and positive ions present at orbital altitudes. These experiments resulted in seven journal articles and conference presentations, and the field programs were reported in a further twenty-one such publications.

TABLE OF CONTENTS

TABLE OF CONTENTS (concluded)

LIST OF FIGURES

LIST OF FIGURES (concluded)

LIST OF TABLES

FOREWORD

This Final Report with USAF Phillips Laboratory's Spacecraft Interactions Branch (Data Item A004-5) documents research by PhotoMetrics on optical emissions associated with spacecraft, chemical reactions that convey information about the processes exciting these emissions, and ultraviolet backgrounds/foregrounds presented by Earth's limb. These artificially-induced and naturally-occurring radiations both interfere with–"contaminate"–and assist in spaceborne surveillance and, in another sense, serve in characterizing the thermospheric-ionospheric orbital environment. Six Interim Reports (Data Items A003) issued previously, identified in References 1-6, are summarized in Section 1.

Twenty-nine articles in technical journals and oral or poster presentations at conferences resulted from the program, and are referenced under the four general research topics volatile liquid releases[3,7-9], thruster rocket exhaust[4,10-14], airglow[15-24], and laboratory investigations.[25-32] (Some of the results reported are from projects initiated before the June 1991 contract period start.) They refer to team efforts under Phillips Lab/Spacecraft Interactions (WSAI) direction, in most of which other contractor groups also participated. Where the name of a staff member (the authors of this Final Report) appears first, PhotoMetrics took responsibility for the initial draft and final editing of the written publication and/or for preparing and presenting the conference paper; we wrote also the initial version of Ref's 13, 15, and 16.

Section 2 reviews reduction and analysis to date of intensified-video photographs of exhaust from a Primary Reaction Control System thruster engine in six defined wavelength intervals, viewing from Orbiter's crew cabin. These liquid-bipropellant rocket motors are closely similar to those applied for some DoD boost and aspect-control purposes. The spatial distributions extend 1-D imaging spectra of the "vacuum-core" volume previously obtained by WSAI[33,34] in sensibly the same view projection, in characterizing its optical signature. The analysis leads to several recommendations for improved future application of the new camera system ("WINDEX"), as well as for refining the guiding flowfield-chemical kinetics model.

Section 3 is an overview of the measurements of UV-visible spectral radiances of the lower thermosphere and mesosphere made in four space shuttle flights between

December 1992 and November 1995. The sensor was WSAI's "GLO" multi-channel imaging spectrograph[35], operated with its associated filter cameras ("spectral imagers") as a Hitchhiker package in Orbiter's payload bay. Its pointing to assemble altitude profiles was controlled around-the-clock from NASA's Goddard Space Flight Center, by a team that included PhotoMetrics staff member J. A. Gardner. In connection with these shuttle missions, the GLO instrument also made measurements (not considered here) of the self-luminosity, local atmosphere interaction, sunlight scattering, and occultation of exhaust from Orbiter's control thruster rockets, and also viewed off-surface radiations induced by the spacecraft's passage. In practice, as GLO could be operated remotely and autonomously during crew rest periods, most of its measurement time was devoted to natural airglow.

Section 4 describes proposed use of several optical sensors now on hand, in space and at ground stations, for identifying the molecular species primarily responsible for the emission(s) near 2.8 µm excited when liquid-thruster exhaust interacts with the low-orbital atmosphere. While this infrared radiation is believed to result from collisions of high translational energy combustion-product water vapor on the background oxygen atoms, the relative cross-sections for non-adiabatic excitation of the stretch bands of H_2O and for atom exchange reactions that produce the spectrally-overlapping vibrational-fundamental bands of OH remain poorly understood. Spectra of the emissions resulting from the lower center-of-mass energy collisions of water routinely released from spacecraft also apply in identifying the radiative and precursor processes taking place in exhaust-interaction volumes.

Section 3 of Ref 2 and Section 2 of Ref 5 describe the principal experiments performed in WSAI's laboratory at Hanscom AFB, MA to which PhotoMetrics (specifically, Gardner) contributed[25-32]. Prof. S. T. Graul of Carnegie-Mellon University consulted for several weeks, performing the experiments that she documents in Appendix D (which the authors of this report have edited).

Two journal publications[3,4] representing Data Item A003 for the program year ending June 1993 are included here as Appendixes A and B. (Ref's 2, 5, and 6 report work done in the other one-year contract periods.) These articles have not previously appeared as (or been included in) USAF reports.

We also completed several smaller-scale tasks, whose results were communicated in Quarterly Progress Reports (Data Items A001) and informally. Appendix C briefly summarizes planning for use of the GLO imaging spectrograph-spectral imagers to characterize vehicle-associated contaminant radiations in connection with rendezvous and docking of Orbiter with the "MIR" manned spacecraft. Other such projects included

-- similar planning to apply GLO, and WSAI's newly-acquired multichannel infrared camera "IRIM", to surveillance and identification of space objects;

-- radiometric analysis of the gray-body visible and short wavelength-IR emissions from the radiatively cooling stream of Al_2O_3 droplets exhausted by solid-propellant thruster motors, to derive their dimensions and emissivities (Abel inversions of the surface brightness profiles measured from the Air Force Maui Optical Site showed a somewhat hollow ~45°-conical volume distribution of these alumina particles);

-- simulation of the performance of a wavelength-agile spectral imager in detection of distant booster rocket plumes against the thermally-radiating troposphere-lower stratosphere, as an adjunct to AWACS in theater missile defense.

Previous related contract work by PhotoMetrics is summarized in References 36-39, which reference further journal publications and interim reports. Thruster exhausts and vented water were the principal optical contaminants/signature elements considered.

SECTION 1

RESEARCH PROJECTS

The principal projects in the contract period June 1991 to June 1996 have been documented in Ref's 1 - 6, which we summarize here.

Scientific Report No. 1

This interim report[1] covers reduction and interpretation of infrared emission spectra (in segments between 2.5 μm and 17.5 μm) from exhaust gases of Shuttle Orbiter's attitude-controlling monomethyl hydrazine/nitrogen tetroxide thruster motors, obtained from onboard with USAF's Infrared Background Signature Survey (IBSS) sensor.[40] This high-resolution, narrow-field, multichannel spectrometer viewed both the expanding combustion products within a few engine exit plane diameters and (to some extent) through the volume in which they react with atmospheric species. The optical-contamination measurements, for which IBSS was mounted on the Remote Manipulator System arm near the crew cabin end of the payload bay, are an element of the Orbiter Environment Experiment performed on mission STS-39 (04 May 1991).

We compared the data with synthetic spectra compiled from USAF's "HITRAN" computer model of equilibrium radiations from atmospheric gases. The excited-state temperatures fit the 800-1200K range. By contrast, the absolute infrared radiances appear to be less than predicted by standard exhaust-plume models such as CONTAM, perhaps because of collision limiting. The IBSS spectra were found to show vibrational and rotational emission from known infrared-active combustion species H_2O and CO_2, with no other molecular features unambiguously identifiable.

Scientific Report No. 2

This annual report[2] interprets the two essentially-unrelated glow phenomena imaged by WSAI in connection with the Bow Shock 2 or UV Diagnostic Experiment[41,42] of 19 February 1991. The data were taken by long-focus radiometric cameras operated at the Air Force Maui Optical Site, tracking a three solid-composite stage "Strypi" research rocket launched some 350 km away in a trajectory that near apogee was about perpendicular to their line of view.

Persisting (for 10's s) visible wake trails appeared as the these rocket motors passed altitudes near 100 km. We interpreted them as due to chemiluminescent reactions with the ambient oxygen of a so far-unidentified minor Al atom-containing

1

species in the exhausted gas. Self-luminous 10's km-long clouds were also produced after engine burnout, with a spatial and temporal dependence that conveys further information about the dynamics of the interaction between the combustion products and atomic oxygen-rich atmosphere. Our conclusions draw heavily on experience from metallized-chemical releases and explosions in the thermosphere, in particular those organized and investigated by Phillips Laboratory/Hanscom's predecessor AF Geophysics Laboratory. While similar long-lived trails have been seen along the wake of at least two other solid composite thruster motors,[43,44] their photographs have not lent themselves to quantification. The results of our reduction and analysis of these unique optical data are further documented in Ref's 3 (Appendix A herein) and 13.

Second, images of the short wavelength-infrared radiation that is excited as this hypersonic thruster exhaust gas becomes reheated in its "bow shock" or contact surface with the background atmosphere were analyzed and heuristically scaled to other vehicle velocities and air densities. (These results were presented to the infrared surveillance community in Ref 12.) The species responsible for this radiation is very provisionally identified (in part by default) as combustion-product H_2O.

Development of both these emitting regions is found to be reasonably well predicted by "classical" similarity hydrodynamics for static explosions in rarefied atmospheres. The shocked exhaust gas, is of course, also treated by DoD numerical models, such as CHARM; nonetheless infrared emission from it appears not to have previously been quantified experimentally. Furthermore, this glow phenomenon was not explicitly addressed in planning for the rocket experiment, which focused on ultraviolet excited by passage of the hard body. Similarly, the chemically-unrelated persisting visible emission from solid-composite thruster exhaust volumes has been only peripherally considered in the literature, and also was not predicted prior to otherwise carefully-planned Bow Shock 2. Both the 100's-m, short-lived infrared-emitting region associated with the shock and the 10's-km long-lived visible trails represent targets for optical surveillance, as well as potentially interfering with measurements of Earth and atmosphere radiations from onboard powered suborbital vehicles.

Also documented in Scientific Report No. 2, are experiments performed in WSAI's Hanscom AFB laboratory on chemiluminescence of hydroxyl[26,27,29] from water vapor, and on reactions of hydrazine[28] (whose methylated derivatives fuel liquid thruster motors) with atomic oxygen ions (abundant in the thermosphere). This effort is part of WSAI's ongoing program of investigation of reactions between ionic and neutral species at the collision velocities prevalent in near-space.

Scientific Reports No. 3 and 4

These technical journal papers,[3,4] submitted as Data Item A003 for the second program year, are included here as Appendixes A and B. The first (as mentioned just above) reports our photometric-photogrammetric analysis of intensified tracking camera images of the persisting self-luminous wake trails from aluminized solid thruster firings at altitudes of high atomic oxygen abundance. We determined the efficiency with which energy of these rocket engines is converted to visible photons by calibrating the camera against images of catalogued stars, and reported the dimensions and fluctuation structure of this element of these commonly-used rockets' optical signature. The hydrodynamics of exhaust from operating rocket engines leads to radiance distributions and time dependences significantly different from those of these engines' lower-density smolder products. The latter chemiluminescent trails resemble previous rocket releases of Al atom-containing chemicals; the former brighter long-lived glows, like these artificially-produced clouds, are seen to drift with the upper-atmospheric wind.

The second of these papers reviews the phenomenology of releases of liquid water into the thermosphere, from a standpoint of contamination of spaceborne optical surveillance and measurement of atmospheric backgrounds. It summarizes the results from Ref 7 and previous WSAI-originated publications on this topic, extrapolating them to wavelengths other than the visible for which data exist – in particular, infrared. This journal article also discusses scaling the effects to the thermodynamic and related properties of other common liquids (equation of state, surface tension, heat capacity, temperature dependence of vapor pressure, ...). It further considers flow back to the spacecraft of vapor evolved from the initial coherent stream and the ~μm-diameter droplets into which it explosively bursts near the injection nozzle, that is, the physical contamination from dumping of surplus liquid water. A similar and even higher-flux impingement on Orbiter would result from its so-called flash-evaporated water.[45]

Reference is made to Ref's 8 and 9, preliminary designs for dispersal experiments in near-space to resolve questions that can not be directly addressed by WSAI's images of ventings of a single volatile material from Shuttle Orbiter enhanced by some long-past laboratory chamber investigations. Candidate liquids, whose aforementioned properties differ over wide ranges, include "doped" and dyes-containing water, ethanol, acetone, benzene, and n-hexane; the resulting sunlight scattering would be measured both at ground stations and from Orbiter. As briefly mentioned in the Foreword, ventings of liquid and gaseous water serve in investigating collisional and other excitation of thruster exhaust species (as of course do the already-performed ventings of "permanent" gases[46] in the wall-less laboratory of space).

3

Scientific Report No. 5

This report[5] covers 1) results of groundbased visible and infrared imaging by WSAI of radiations excited by high translational energy exhaust gases from a specially-designed firing of space shuttle's Primary Reaction Control System thruster motors, and 2) three related laboratory studies in which PhotoMetrics played a part. The 12 s-duration operation of two closely-located Orbiter engines directed into ram took place when STS-56 was near culmination at the Air Force Maui Optical Site. The sensors, an ISIT video with visible-range response and an InSb-array camera filtered for 2.3 - 3.6 µm, were coaligned on a tracking mount with fields-of-view set (on the basis of experience from previous such control thruster firings) to encompass the above-threshold volumes. These projected as somewhat flattened ellipses having essentially Gaussian radiance profiles parallel and perpendicular to the spacecraft trajectory, which extended to the hard body itself but not detectably upstream of it.

The SWIR glow initially extended axially more rapidly, at closely the (calculated) exhaust velocity relative to Orbiter; then by ~1 s after ignition it was overtaken by the visible glow, and thereafter both volumes continued to expand increasingly slowly. Local maximums in surface brightness appeared before ½ s, indicating peak volume emission rates one or two orders of magnitude above those during this later period of slow further growth. These brightness decreases are due to essentially-dynamic depletion of the ambient reactant, atomic oxygen. A largely unexpected finding is that the total power outputs within the two-wavelength intervals have functionally different dependences on time after thruster ignition, which identify the orders of the reactions that produce vibrational and electronic luminescence from the interaction volume. (The somewhat larger later extent of the visible glow results from diffusion of its precursor species.) The observed SWIR grow-in compares reasonably well with predictions from Phillips Laboratory's "SOCRATES" flowfield-excitation model.[47]

The laboratory effort during this third contract year included a study of the products of reactions of hyperthermal oxygen ions with monomethyl hydrazine[29], precise measurement of the ionization potentials of two alkaline-earth fluorides[30], and an investigation of production of water clusters by laser-beam vaporization of ice.

Scientific Report No. 6

This report[6] reviews work on far- and middle-ultraviolet spectra of the Earth's limb obtained by WSAI in the solar terminator-following "GLO-1" experiment, which was performed on space shuttle mission STS-53 (December 1992).[15-23] Data on the

strong dayglow from minor component NO and the weak scattering from trace metal atoms/ions are reduced and analyzed, and an approach to accessing the sharply diurnally-varying intensities of radiation from major species N_2 is presented.

Orbiter's unique trajectory led to long-period sampling of airglow near dawn and dusk during this ~1 week mission. The space operations-degrading backgrounds/foregrounds resulting from scattering of mid- and far-UV sunlight by nitric oxide molecules were found to be about three times higher in the evening than in the morning sector, under the prevailing geophysical conditions. This result is due to the increase in densities of NO in the thermosphere and mesosphere as the Sun photodissociates N_2 into its precursor $N(^2D)$ and (^4S). We presented a procedure for assessing airglow radiances in individual γ (and the weaker δ and ϵ) bands of this low-concentration aeronomic species under conditions of significant attenuation of ultraviolet by NO along solar illumination or sensor sight paths.

The variation of sky brightnesses in the photoelectron impact-excited electronic bands of thermospheric N_2 with incoming flux of hard solar photons is shown to exceed substantially that due to the alteration of upper-atmosphere density profiles associated with solar and magnetospheric activity; these limb brightnesses change particularly rapidly as the Sun approaches the local horizon. By contrast, scattering of middle ultraviolet by NO in its generally optically-thin bands depends primarily on the fluences of these energetic photons over several previous days. We reviewed in detail the excitation of N_2, which leads to comparably-intense UV in two triplet and one singlet band systems; their ratios are expected to remain sensibly constant, except in sight paths where absorption by the atmosphere plays a part. Overall, the daytime limb backgrounds/foregrounds from relatively high concentration N_2 are comparable with those from NO.

The GLO imaging spectrograph[35] achieved the first simultaneous measurements of concentrations in the ionosphere of a metal atom (Mg) and its positive ion, which apply in validating models of plasma transport and chemistry near the geomagnetic equator. GLO-1's global altitude-profile survey showed several further features of the resonant scattering by charged and neutral atoms originating from cometary material, including strong dawn/dusk differences. Its ~6Å-resolution airglow data serve for determining upper-atmospheric densities and temperatures (we derived a density of NO, for example), as well as in planning optical surveillance for missile defense and validating DoD code models of ultraviolet sky background radiances such as AURIC.[48,49]

5

SECTION 2

SPATIAL/SPECTRAL DISTRIBUTION OF CHEMILUMINESCENCE
FROM SPACE SHUTTLE THRUSTER EXHAUST

Introduction

We started reduction and analysis of filter photographs of exhaust gases from one of Shuttle Orbiter's 870 lbf-thrust Precision Reaction Control System (PRCS) motors, taken onboard STS-63 with a new intensified multispectral video camera, "WINDEX." An example 4-ms exposure image, from a 20-nm FWHM channel centered at 736 nm (Figure 1), shows above-threshold radiances of the so-called "intrinsic core" exhaust region extending outward roughly 15 0.24-m exit plane diameters in a limb-brightened quasicone of initial half-angle near that of the thruster's nozzle (23°). The experiment was intended to extend the scope of 1-dimensional-spatial spectral distributions measured 4-1/3 years previously by WSAI[33,34], which served to identify the upper states of the principal visible-chemiluminescing species.

These electronic bands and lines were interpreted[33,34] as arising from excitative reactions among some of the combustion gases – in a sense, "afterburning"– as they adiabatically expand and cool. (Thruster exhausts are well known to radiate also in the ultraviolet and infrared, largely through different excitation processes.) This origin stands in contrast to the gases' "atmosphere interaction" further downstream that leads to the much larger area, lower volume emission rate optical features addressed in Section 4 and Ref's 10, 11, 14, and 16 (and of course elsewhere).

We limited this initial effort to that which we considered justified by the reliability of the provisional camera performance characteristics that we were able to extract from manufacturers' specifications. Further analysis indicated when WINDEX has been radiometrically and photogrammetrically calibrated, along with recommendations for improving both its application to determining the optical signature of liquid-bipropellant thruster motor firings and the numerical model that guides interpretation of these image data, is specified at the end of this Section.

Previous Imaging Spectra and Interpretation (in Ref's 33, 34)

An emission spectrum at nominally 1 m from the PRCS exit plane obtained by WSAI's Auroral Photography Experiment sensor is reproduced in Figure 2. The molecular features were identified spectrally, and their column emission rates predicted by a numerical model of the multizone reactive flowfield of low-concentration C_2H_2, OH, O, and NO and ("unoxidized") major exhaust species H and H_2. (Atomic oxygen forbidden lines, which appear strong in an essentially end-on projection of the intrinsic core and atmosphere-interaction region,[50] are
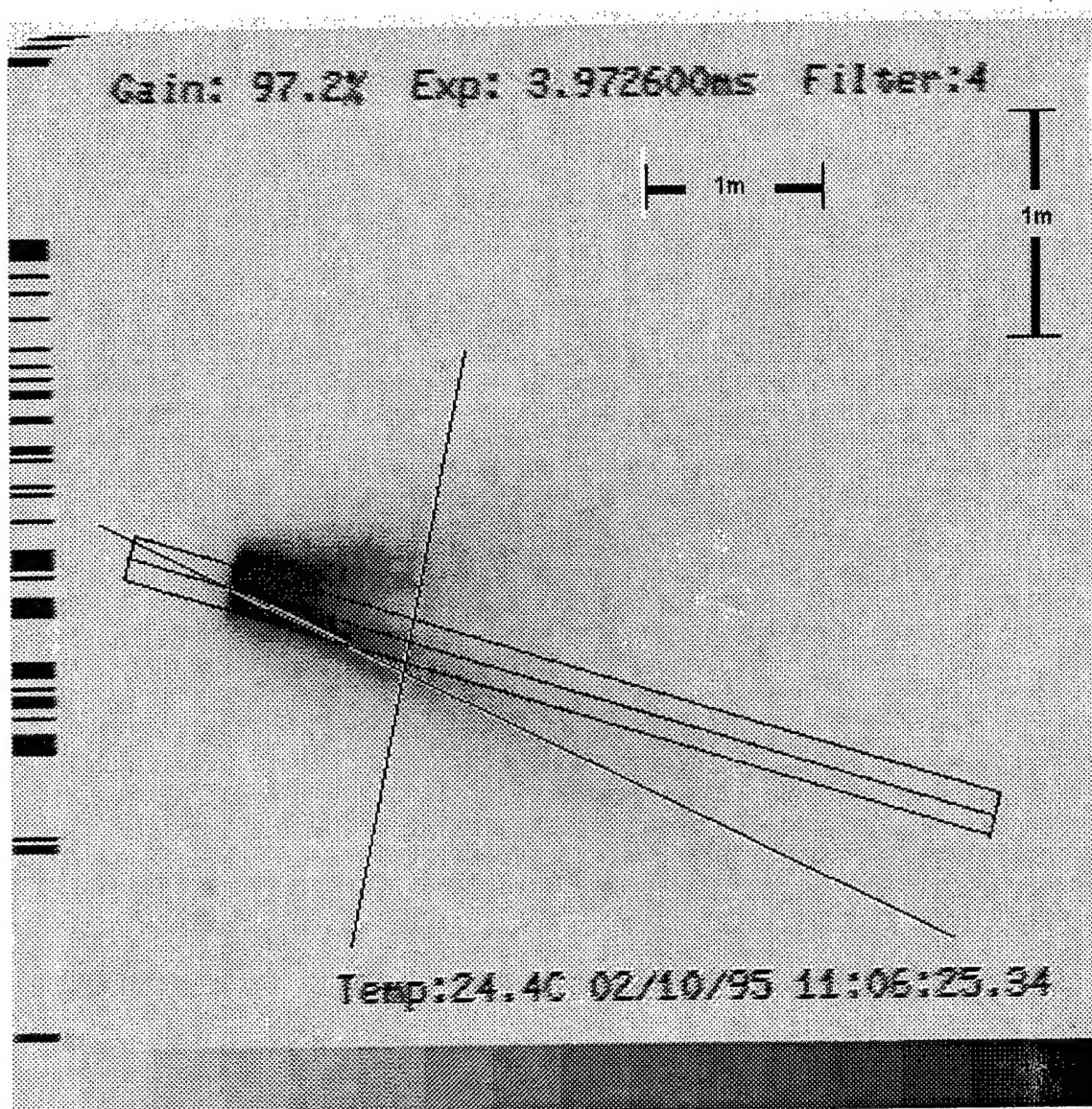
Figure 1. Channel 4 (736 ± 10 nm) image of single thruster firing A, identifying the scan lines and areas analyzed. The distance scales are provisional.

not considered in these chemical-kinetic calculations.) The emission is interpreted as dominated by bands of carbon atom-containing diatomics (whose several reaction steps-earlier precursor is <1/100% mole concentration C_2H_2) and the quasi-continuum from NO_2 ($^2B_1$, $\tilde{X}$ (v >> 0) $\rightarrow$ $\tilde{X}^2A_1$, v $\approx$ 0) at the shorter visible wavelengths, and by NO_2 and electronic bands of HNO ($^1A'' \rightarrow \tilde{X}^1A'$) longward of about 500 nm. These triatomic-molecule features have also been identified by WSAI in other views of PRCS exhaust;[50,51] their theoretical prediction results from adding on to a previous multispecies reaction model[52] the third body-stabilized recombination processes NO + O and H, assigned rate coefficients with the same functional form.

7
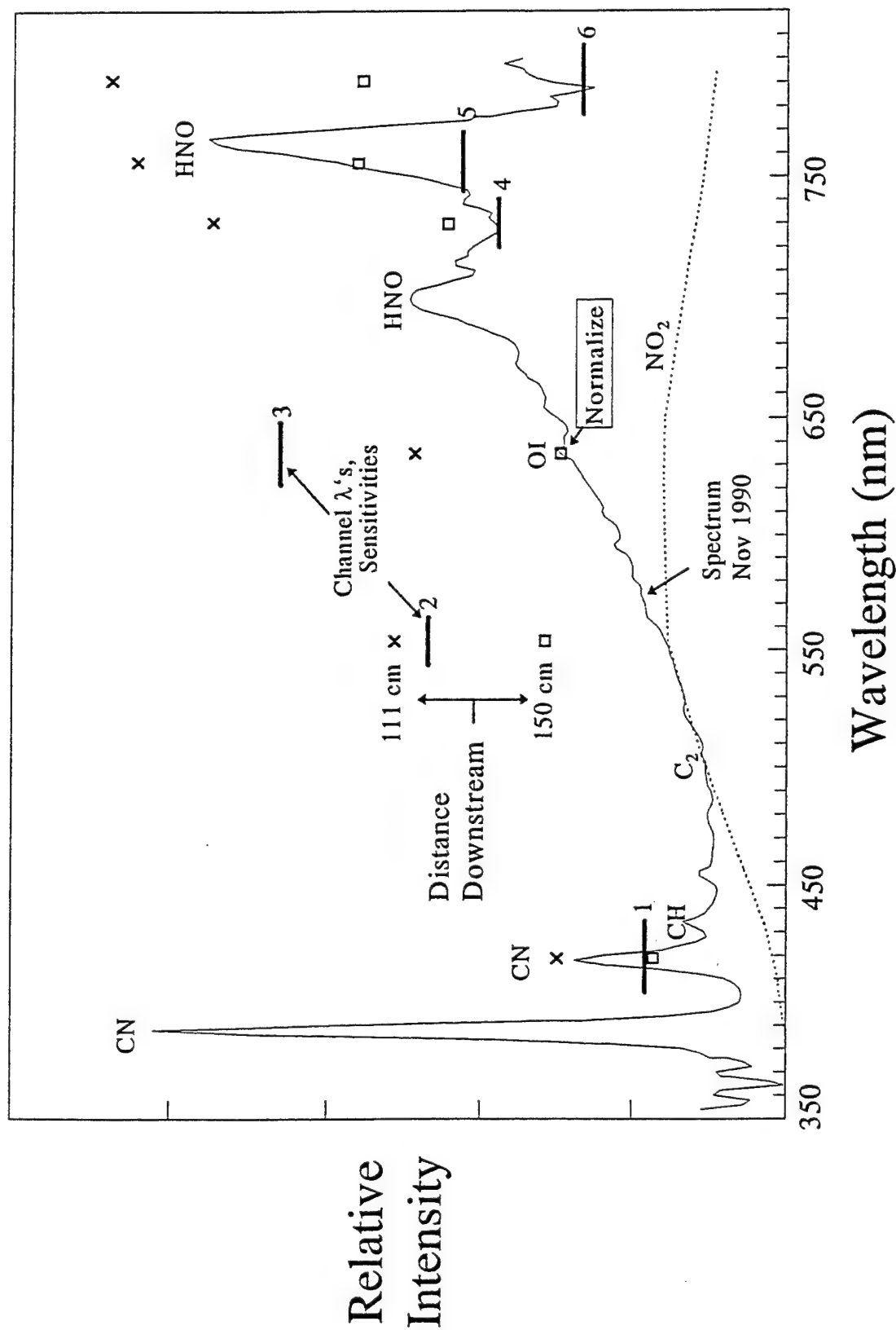
Figure 2. Spectrum of the thruster exhaust ~100 cm from the exit plane,[34] with relative camera channel sensitivities and FWHM spectral extents from Table 2. The ×'s and □'s are provisionally-calibrated brightnesses at 111 and 150 cm respectively, normalized to channel 3. The underlying NO_2 quasicontinuum is from Ref 62 (in energy units), normalized at 550 nm where other exhaust emission features appear weak.

The model spectral-spatial distributions are derived from expected radial gradients of oxidizer/fuel ratios and combustion chemistry that lead to more detailed output-species concentrations than those appearing in earlier characterizations of PRCS performance.[11,14,45] Axial brightnesses of NO_2*·† and HNO* would decrease relatively slowly downstream, as the recombination rate coefficients that lead to these excited molecules increase with decreasing gas temperature. By contrast, the brightnesses of bands from CN*, C_2*, and CH* radicals produced starting with high potential barrier reactions in the fuel components-rich region near the exit plane would decrease more rapidly. While the spectrographically-measured falloffs in perpendicular-to-axis-column emission of identified spectrum features were in general agreement with this idea[34], Figure 10 shows they in fact differ quantitatively from the predictions. (The initial increase in HNO radiance that was observed is thought to be an artifact of the projection of the slit on the luminescing volume[34]; that is, the imaging spectrograph was probably not accurately aligned along the bright lower limb shown in Figure 1.)

The flowfield model takes the species densities to be decreasing about as (distance downstream from the exhaust nozzle D)$^{-2}$ and temperature T to be varying as $D^{-2(\gamma-1)}$ or $D^{-\sim0.6}$, where γ is the ratio of specific heats of the expanding combustion gas. This isentropic-flow formulation does not consider alteration of concentrations by chemical reactions or the effects of finite radiative lifetimes on the observable, surface brightness. Since the cross-stream view path lengths increase about linearly with D, and the rate coefficients for NO + O and H recombinations are taken as depending on T^{-2} (the 1984 CODATA Task Group[53] recommends $T^{-1.6\pm0.3}$), where collisional deactivation can be neglected the axial brightnesses in these two termolecular features would vary with $D^{-1.8}$. In practice, the decreases with D in both total excitative NO_2 recombination rate coefficient and peak wavelength of the quasicontinuum play some part,[54-57] which we return to below. The computational-model axial brightnesses of these two features between D = 50 and 300 cm (extracted from Figures 8 - 9 of Ref 34) fit $D^{-1.6}$, and – rather better – (D + exit plane diameter D_o)$^{-2.0}$ and (D + D_o/2)$^{-1.8}$. In this regard, the mean downstream displacement of NO_2*·† molecules before they radiate is of order one (24-cm) exit plane diameter; the exact figure is uncertain due to their ill-defined radiative lifetime.[54,58] Similarly, the 25 ($\pm$4)-μs lifetime of HNO (^{1}A" 000)[59] leads to one-third this longitudinal smearing (and not inconceivably also some collisional deactivation, or spectrum alteration).

The inputs to Ref 34's kinetics model lead to its prediction of significant limb brightening in the CN violet ($B^2\Sigma \rightarrow X^2\Sigma$) band sequences but not in the NO_2 and HNO features, in disagreement with the WINDEX observation (as we will show). No CN red

($A^2\Pi \rightarrow X^2\Sigma$) radiation was detected by the Auroral Photography Experiment sensor despite its upper state having two orders of magnitude higher probability of being excited (in the same atom-exchange reaction, $C_2 + NO$), due to a combination of the rapid collisional quenching and broad spectral extent of this band system. The WINDEX camera, by contrast, showed excess signal in one of the CN-red wavelength intervals (as we will also discuss).

Filter Camera and View

As the thruster operation and the view projection differ negligibly from this earlier experiment (also performed at night, on STS-38), we describe them only briefly. The exhaust gases imaged emerge from attitude-controlling PRCS L1L, which is directed ~ 1-1/3° toward the spacecraft's +z axis (downward) from its –y (port-side) axis, from a position about 1 m aft of its portside Orbital Maneuvering System engine pod. WINDEX, mounted on an adjustable bracket at the rear of the aft crew cabin, pointed out its payload bay-facing window located closely 25.0 m from the thruster exit plane. The camera's view aspects were thus within 9 and 19 degrees ($\cos^{-1} 0.95$) from perpendicular to the "symmetry" axis of the above-sensor-threshold exhaust stream. We judged that correcting radiances for these slight changes in view path, much less for the <1% total difference among ranges to the camera, would not be indicated for this initial image reduction. The pod cowling obscures the first 50 ± 10 cm of the flowfield; while this obscuration hampers comparison between the numerically calculated and measured spatial distributions of near-perpendicular-column emission rates, it also protects WINDEX from the very high (predicted) exposures from exhaust gas this close to the exit plane.

The camera (Xybion [San Diego, CA] Model IMC-201) rotates a 6-position interference filter wheel through its optical system at 5 Hz, precisely synchronized with readout of its final-stage charge-coupled-detector array. This fast continuous sweep of 25.4 mm-diameter clear area filters across a 18 mm-diameter photoemissive image plane provides a 3.97-ms effective gating time for each video frame. (About 10-times-longer exposure durations could have been achieved by cycling the six filters to observe only "steady-state" emission from the intrinsic or vacuum core; refer to the radiant intensity plots in Figures 6 and 7.) Although the interference filters are placed in the f/1.4-converging beam of a 35 mm-focal length (Nikkor) objective lens, since their wavelength spans all exceed 20 nm off-axis rays would not alter their overall transmission. Changes in temperature shift the filter bandpasses by about 1½ nm per 10 C°, and thus also have only a very small effect on the WINDEX data.

Table 1. Characteristics of WINDEX Camera Channels*

Filter Identification	Principal Emission Feature&	Center, Maximum Wavelength, nm†	FWHM, FW$\frac{1}{10}$M, nm†	Maximum Transmission	Window Transmission¥	Photocathode, Sensitivity mA/W**	Relative Power Sensitivity
1	CN (CH)	418, 419	30, 40	0.54	0.91	15	1.0
2	NO Contin	554	20, 24	0.65	1.0	44	2.5
3	Contin (OI)	635	26, 33	0.60₅	1.0	51	3.6
4	Contin, HNO	735.5, 730	20.5, 27	0.63	0.92	39	2.1
5	HNO, Contin	756, 752	25.5, 38	0.65	0.84	38	2.3₅
6	Contin (CN?)	796, 791	30, 43	0.58	0.55	34	1.5

*Measured at normal incidence at the nominal center of each 1-inch diameter filter, before application of antireflection coating

† ±1 nm   ¥Relative to 450-600 nm, 0.84   **Manufacturer's spectrum   &Refer to Table 2

Table 2. Estimated WINDEX Channel Signal 100 cm Downstream

Channel/Feature	CN Violet	CH*	NO$_2$ Contin†	HNO¥	Other&
1	0.65	0.12	0.22		
2			0.9	<0.1	
3			0.7	0.3	
4†			0.5	0.5	
5			0.24	0.76	
6†			0.45	0.23	0.32&

*A → X, Δv = 0   †Applying laboratory spectrum as in Ref 62
&CN A → X? See text.   ¥Applying laboratory spectrum reproduced in Ref 34

11

A microchannel electron multiplier in proximity to the photocathode places the intensified images on a phosphor, whose emission pattern is conveyed by a 3:2 demagnifying fiber-optic bundle to a 8.8×6.6 mm, 764×488 element CCD array. Full angular field in the long image direction is thus 10.7 degrees, which converts to a 4.7 m horizontal field-of-view at the mean range of the diverging exhaust stream, or closely 0.6 cm per pixel along its long axis. As Figure 1 shows, the radiating volume is "centered" some 10 degrees below the horizontal, presumably due to the camera's (unrecorded) angular orientation.

Characteristics of the six WINDEX channels (Table 1) include transmission of what we interpret as the center area of their interference filters at normal incidence before anti-reflection coatings were applied, provided by the camera's manufacturer; nominal spectral response of its "Gen 2 Red" intensifier photocathode; and transmission of Orbiter's rear flight deck window. The final column lists the calculated end-to-end sensitivities, relative to shortest-wavelength channel 1. Pending actual measurements we assumed constant transmission of the camera lens, although fast 35-mm film format lenses are known to lose of the order of 15% at 400 nm and exhibit further small variations over the visible wavelength range; we also assume that this lens has uniform aperture ratio over its aforementioned narrow field-of-view, that is, negligible vignetting.

The window transmissions (sixth column of Table 1) were taken from WSAI's analysis in connection with spectrometry of off-surface spacecraft glow[60]; channel 1 is weighted for its expected domination by the CN violet $\Delta v = 1$ sequence (Table 2). The actual half- and tenth-response widths of the camera channels differ somewhat from those of their interference filters, as photocathode conversion efficiencies are not strictly constant within these filters' spectrum intervals. We have stated responses in power (rather than photon) units, on the expectation that the spectral intensities reported in Ref's 33-34 also refer to power.

The relative emission spectrum in Figure 2 refers to a column of exhaust gas oriented toward the camera located 100 ± 10 cm from the PRCS exit plane[34] and roughly 10 cm downward from its axis[61] (that is, toward Orbiter's $+z$ direction). Plotted for comparison are the calculated sensitivities and FWHM's of the channels from Table 1; a recent third body-stabilized laboratory recombination spectrum[62] from $\sim 300K$ NO_2 at gas densities $1.3 - 17 \times 10^{16}/cm^3$–it differs negligibly from earlier spectra,[56]–normalized to the field data at 550 nm (expressed in energy units); and WINDEX data that we identify below. The NO_2 pseudocontinuum would appear to mask beyond realistic hope of recovery the (unresolved) $630 - 636.4$ nm $^1D \rightarrow {}^3P$ doublet from

12

atomic oxygen within channel 3. (The strong CN 5,1 A $\rightarrow$ X band also lies within its wavelength interval.)

The normalized "fully quenched" NO_2 emission spectrum[55,56,62] applied with these nominally 4-nm resolution Auroral Photography Experiment data leads to the estimated contributions to the WINDEX channel signals listed in Table 2. This derivation makes the simplification that the sensitivity of each camera channel is constant over the half-transmission wavelengths (FWHM's) of its filter and zero outside them; neglects other, weaker emission features; applies the laboratory spectrum of recombinant HNO[34] (apparently unquenched) for characterizing channels 4 and 6; and–in particular–does not take into account any change in the spectral distribution of the NO_2 pseudocontinuum.

This spectrum alteration is believed due to collisions that induce potential curve crossings of $^2B_2$ state-recombinant NO_2 molecules to and from high vibrational states of $\tilde{X}^2A_1$, and depopulate these (mixed) levels.[54] The mean densities of the exhaust gas calculated from isentropic flow[34] are 3×10^{16}, 3×10^{15}, and 6×10^{14} cm^{-3} respectively at D = 50, 200, and 500 cm (the practical detection limit of WINDEX before extensive coadding of images). These densities would correspond to pressures of 860, 85, and 18 millitorr at room temperature. Over this density range, the ratios of pseudocontinuous spectral emission within channels 3 - 6 to NO_2-dominated channel 2 decrease by 15 - 25%. At the same time the apparent total two-body recombination rate coefficient is decreasing roughly logarithmically from 6 to 3×10^{-17} cm^3 s^{-1},[56] due to the lower density of associative reaction-stabilizing third bodies.

The effects of temperature on the fully-stabilized NO_2 recombination-emission rate (with the spectrum of Ref 62) is taken into account (as T^{-2}) in the chemical-kinetic model.[34] Considering further the weak effect of temperature[63,64] and even buffer gas type[54,56,62] on the spectral distribution, this dependence would apply best in the so-called high-pressure ($\gtrsim 1$ Torr at 300K) region of the PRCS exhaust flow. The laboratory-tank spectra[56] indicate that at downstream distances beyond 150 cm, and less outside the higher gas-density flowfield limbs, the NO_2 pseudocontinuum contributes fractionally less to the signal in each of the WINDEX channels, relative to its standardization value in channel 2. Straightforward model calculations would correct the spatial distributions of the several emission features for this variability; additionally, the decrease in effective NO_2 recombination rate coefficient with third-body density (separate from its increase with decreasing gas temperature) could readily be taken into account.

The theoretical prediction[34] that the ratios of emission per unit wavelength from NO_2 and HNO track one another over the flowfield would lead to the same relative

13

signal in channels 2 to 6 everywhere in these WINDEX images. Indeed, such constant behavior which, as we will see is not observed, would obviate the need to design the experiment to isolate the two recombinant features. Conversely, relative sensitivities in channel 1, which the provisional calibration shows as dominated by the CN violet $\Delta v = 1$ sequence, would vary both axially and transversely over the intrinsic core.

Data

Five firings of PRCS L1L only at nominal intervals of 45 deg from Orbiter's trajectory direction (in its x–z plane) were photographed while the spacecraft was at 297 km on 10 February 1995, as summarized in Table 3. (Images of a further firing series at lower WINDEX sensitivity are to become available.) The camera was operated by the STS-63 mission specialists, without synchronization with turnon/off of the thruster(s). Typically, <½-s "correction" firings of other attitude-control rocket motors that reoriented the spacecraft for the succeeding measurements appear to provide less useful data. Those firings of L1L simultaneous with nose-mounted thrusters F1L or F3L, whose self-luminous exhaust streams do not come into the WINDEX field-of-view, appear sensibly identical. (A precise listing of PRCS operation times and Orbiter orientation angles is to be supplied by NASA; the timing reported here comes from the video display, as in Figure 1.)

The photographs show no significant differences among these five L1L exhaust directions, as is illustrated by isophote-contour plots from channels 1 ("CN") and 5 ("HNO") midway through direct-ram PRCS firing A and direct-wake firing E (Figure 3). This invariance of the emission pattern near the exit plane is expected, as few collisions with the $\sim 10^9/cm^3$ density background air relative to those among the factor-10^{-6} more dense combustion gases themselves are taking place. The crew's unfortunate adjustment of the camera's pointing between firings hampers, but does not preclude, coadding of image sequences further to suppress noise and increase the useful downstream range of photocurrents. (These changes are identifiable from the position of the low-contrast Orbital Maneuvering System pod in the camera field between thruster firings, as well as in Figure 3). We, therefore, focus initially on ram firing A, Tail only, in Table 3.

Figures 1 and 3 are typical of the radiance distributions reached in two or three 1/30-s video-interframe times after (apparent) turnon of the thruster motor. They show a substantial transverse asymmetry, which is more quantitatively illustrated in the normalized photocurrent traces 105 to 150 cm downstream (Figure 4). (The distance scale, derived as described above, remains subject to an estimated $\pm 10\%$ uncertainty.)

14

Table 3. Operation of the WINDEX Camera and PRCS Thrusters on STS-63

Start WINDEX	11:02:00	10 February 1995
Filter 1 in place	11:02:07	
Filter wheel on	11:04:05	3.97 ms exposures

Firing Sequence	A	B	C	D	E
Angle to Ram (nominal)	180°	135°	90°	45°	0°
Start Nose and Tail	**11:04:24**	**11:10:24**	**11:16:24**	**11:22:24**	**11:28:24**
End	**4:27**	**10:27**	**16:27**	**22:27**	**28:27**
Correction (up, side	4:44-	10:44-	16:43-	22:44-	28:44-
Firings and both)	4:49	10:50	16:49	22:49	28:49
Camera Mount Adjustment	5:40		16:35		28:25
Start Tail Only*	**6:23.7**	**12:24**	**18:23**	**22:24**	**30:24**
End	**6:26.6**	**12:27**	**18:27**	**24:27**	**30:28**
Planet in Field of View				24:32 to 24:42	
Correction Firing†	(up) 6:45	12:44	18:44	24:46	30:44
Mount Adjustment	6:47	13:37		24:40	
Correction Firing†	9:52	(up) 14:31	20:05	26.19- 26.29	(aft) 33:24

_ _ _ _

*Thruster L1L   †Realignment for next sequence

15
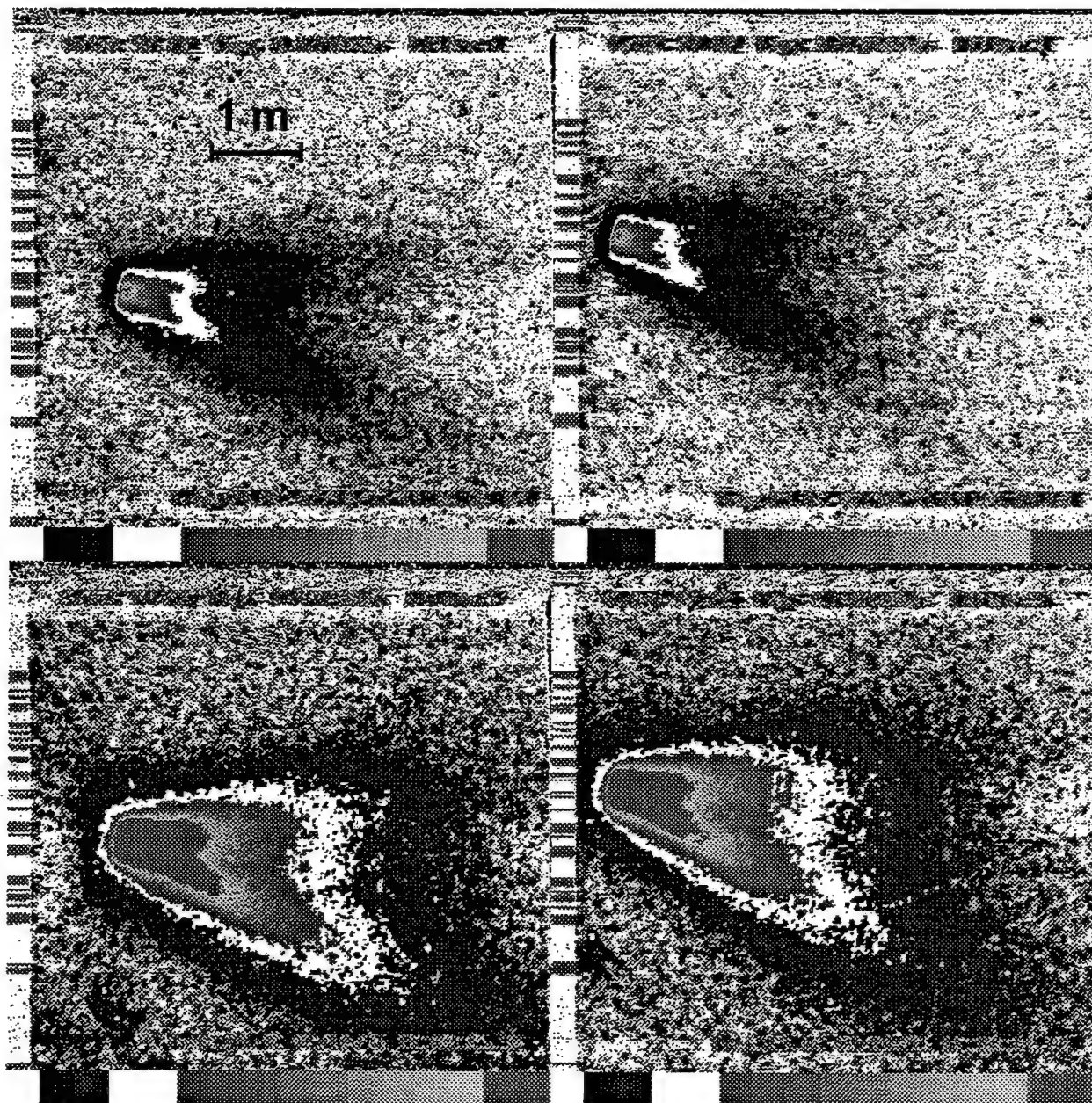
Figure 3. Isophote plots of ram (left) and wake thruster firings from channels 1 (top) and 5.

We, as usual, take the column emission rates to be proportional to these output currents over baseline leakage current; that is, we assume the camera's response to be linear until it saturates. (Essentially linear behavior was observed in initial WINDEX performance tests.[61])

16
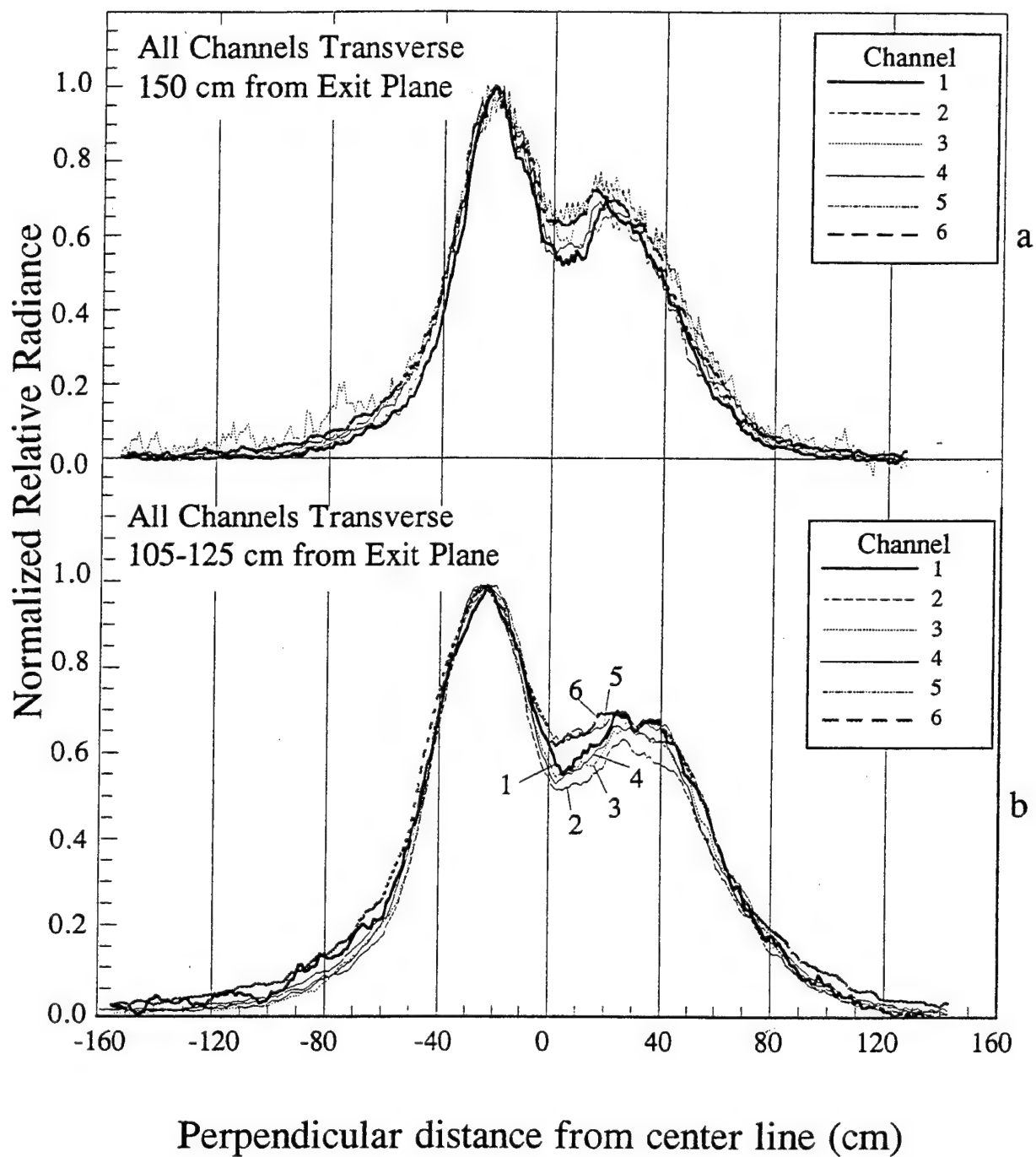
Figure 4. Photocurrent traces perpendicular to the exhaust centerline, normalized at their peak. a) Single line trace at D = 150 see Figure 1); b) average between 105 and 125 cm, showing the effect of summing on noise.

Ratios of the larger peak-to-trough (axial) radiance are somewhat more pronounced in both the low- and high-noise traces at the two shortest wavelengths, which also evidence slightly narrower emission profiles; channel 5 shows the lowest such brightness ratio, along with the broadest transverse profile. That is, those camera channels to whose signal HNO emission makes a large contribution show somewhat greater spatial "smearing" (perhaps because the lighter recombining hydrogen atoms are decoupling from the other reacting combustion species). The 3:2 brightness ratio of the two limb peaks is also observed in the images of the other L1L firings in Table 3; the asymmetry is presumably an artifact of performance of this particular PRCS motor. Figure 4 provides a measure of the signal/noise improvement achieved by coadding photocurrents from adjoining scan lines.

Near-axial radiance profiles measured by the six WINDEX channels are plotted in Figure 5. We selected the 21 pixels, across area indicated in Figure 1 for this presentation as a compromise between longitudinal resolution from the enhanced limb brightnesses and applicability of the existing model[34] of emission-feature radiances viewing perpendicular to the thrust symmetry axis. Only least-sensitive channel 1, with its weak recombination-species component, remains on-scale to within the 50 ± 10 cm from the exhaust exit plane allowed by the camera's projection. The rocket engine appears to ignite between channel 2 and 3 images, and its exhaust glow in effect stabilizes by channel 6, less than 4/30 s afterward (somewhat later at the wavelengths of channel 1).

The luminosity of the exhaust stream decreases more slowly after turnoff, which appears to be taking place on the sixteenth one-fifth-second filter wheel cycle after turnon between channels 5 and 6. The near-axial brightnesses decrease about exponentially with characteristic times 0.1 - 0.2 s; their peaks do not appear to move axially. Other wavelength intervals give evidence of somewhat more rapid radiance decreases than channel 1, especially immediately after turnoff. Figure 6 sums all the photocurrents in the camera's field, and Figure 7 sums within the rectangular area indicated in Figure 1, provide a qualitative comparison of these optical yield rates after the PRCS thruster is shut off.

To smooth further these near-axial radiances, we coadded them over the slightly less than 3 s of stable engine operation (Figure 8). The measured brightnesses vary about as $(D + D_o)^{-3}$, while as noted above the prediction is $(D + D_o)^{-2}$ (see also Figure 10).

The radiant intensities within the fields/sensitivity ranges of the WINDEX camera (Figure 6) do not include the substantial off-scale signal from $D < 100$ cm, along with its component screened by the Orbital Maneuvering System pod. Their fluctuations are more likely a measure of the precision of the photocurrents-above-baseline summed
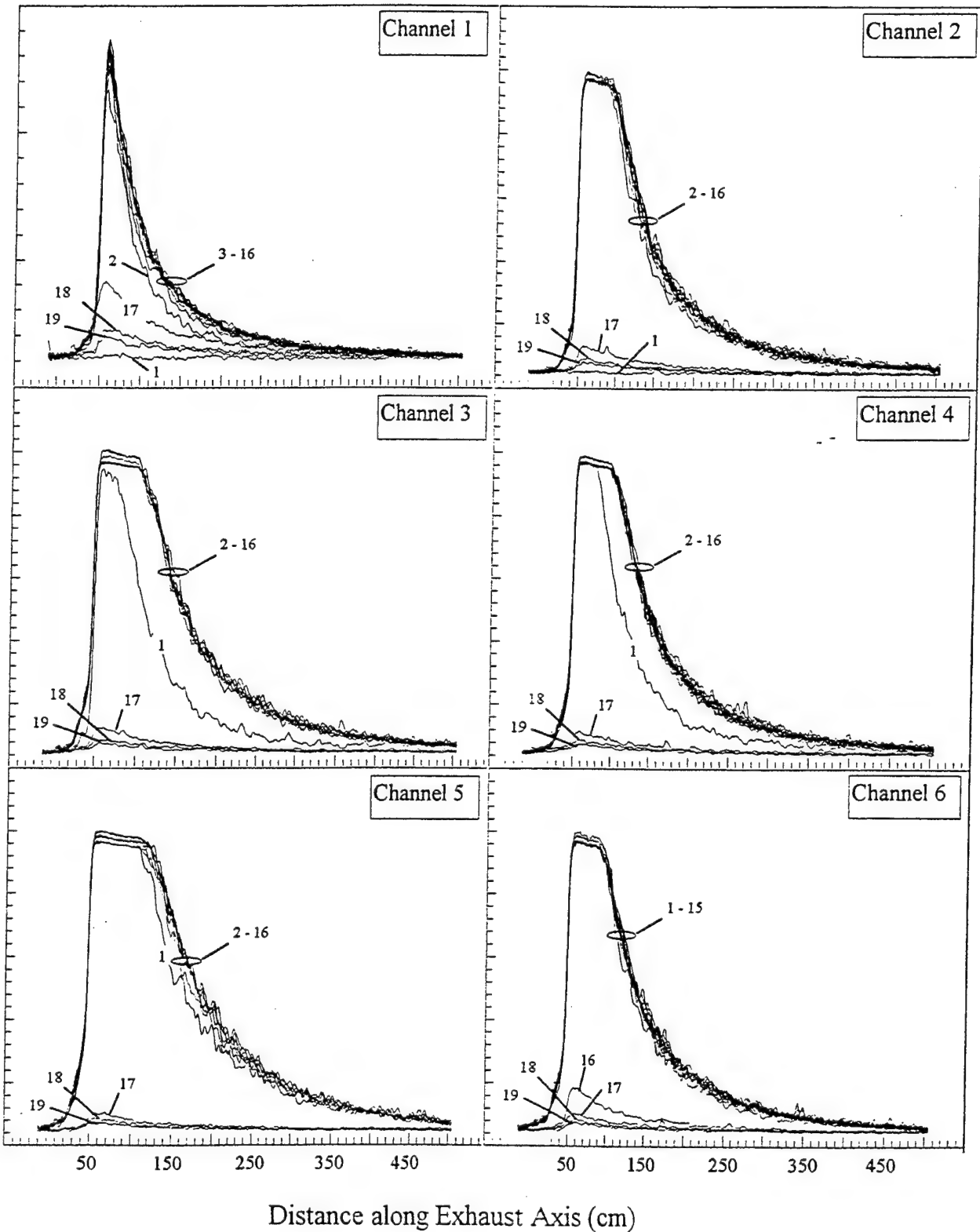
Figure 5. Relative radiances in the rectangular area indicated in Figure 1 (sums of 21 pixels). The numbers identify the WINDEX images after thruster turnon.
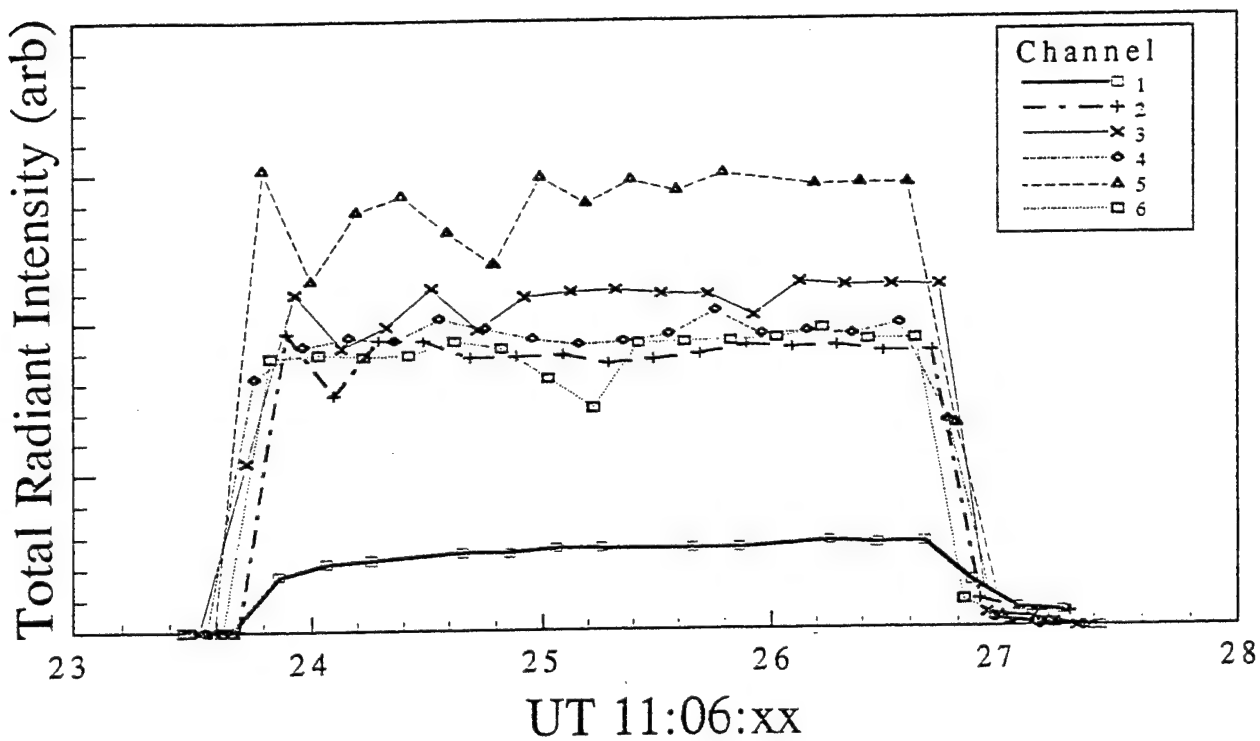
Figure 6. Total relative radiant intensities measured in the six WINDEX camera channels.
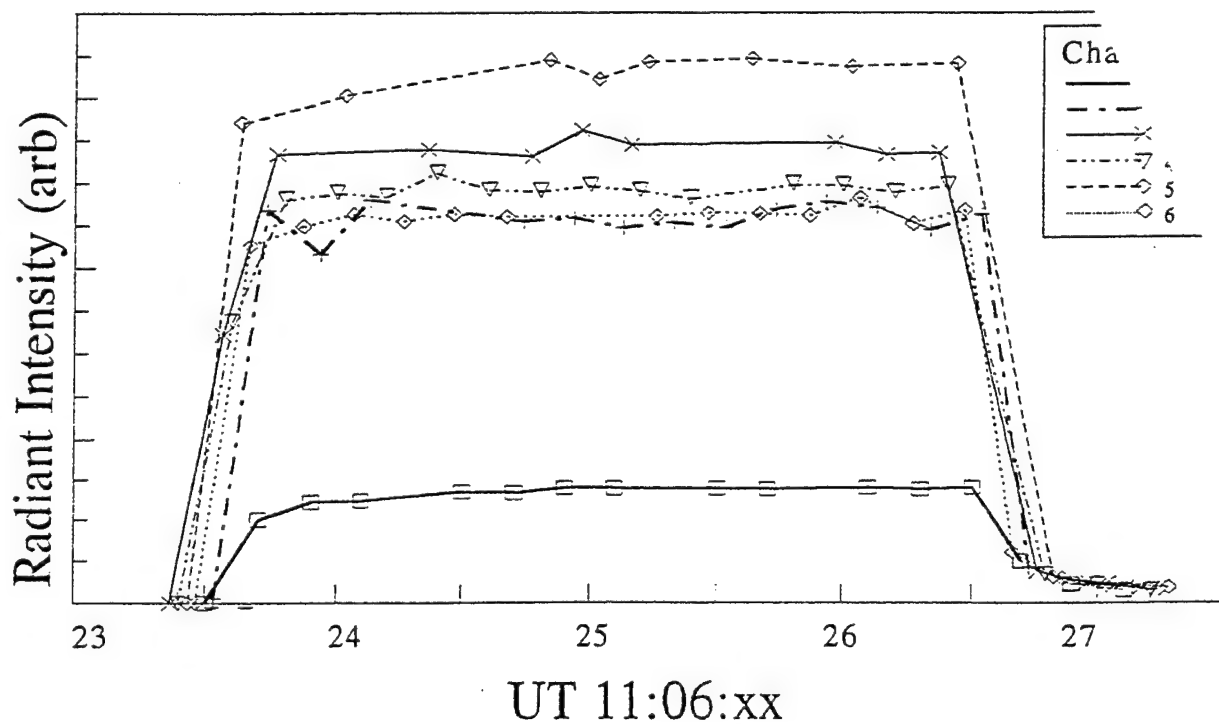
Figure 7. Sums of photocurrents within the longitudinal area shown in Figure 1.
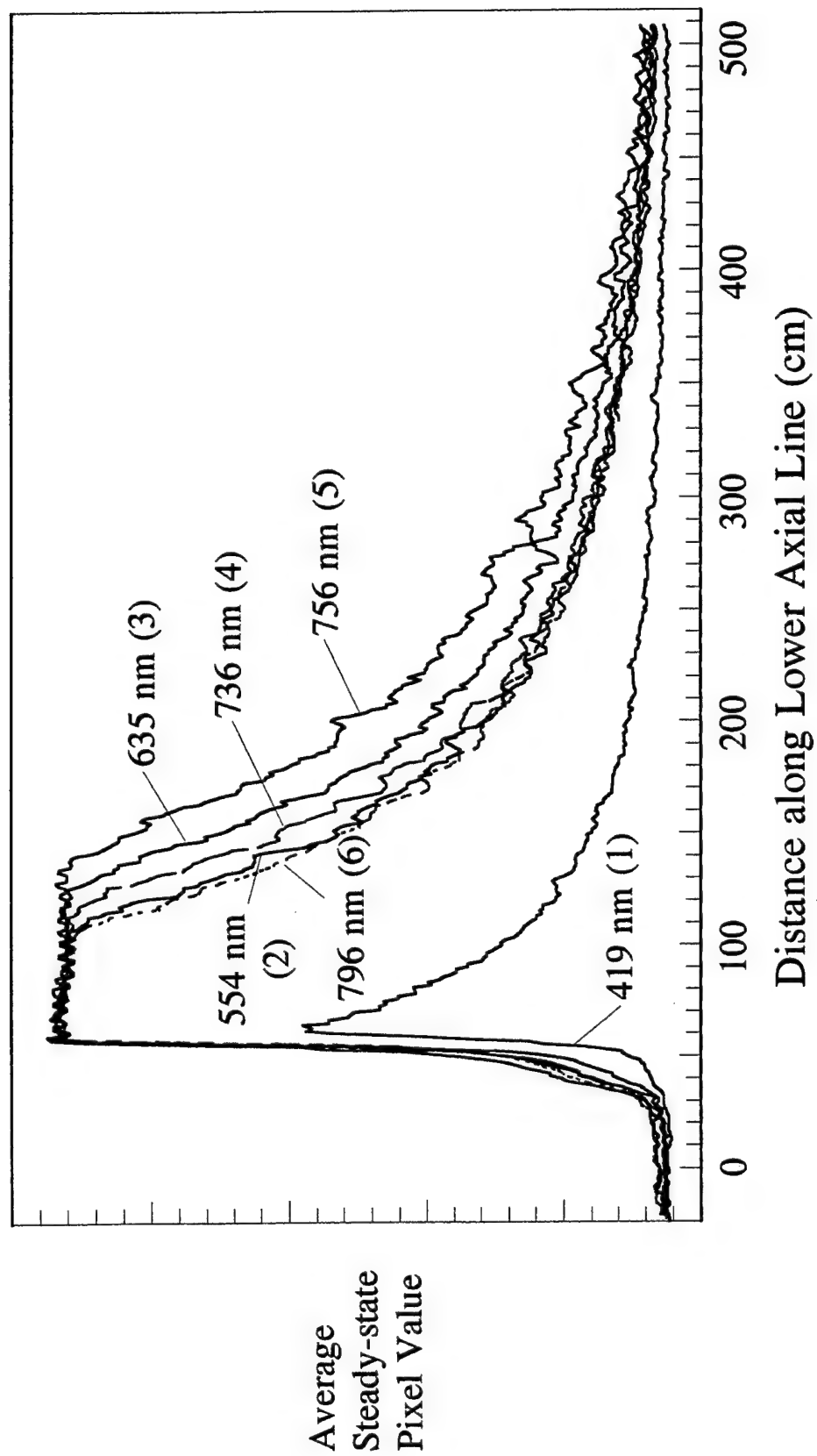
Figure 8. Averages over the duration of the thruster firing of the relative radiances along the limb.

over the full image field than a real effect of the bipropellant burn, as is further indicated by the smoother results in the limited exhaust-scene region of Figure 7. By contrast, the increase in CN- and CH-dominated, high photocurrent signal/noise channel 1 over 3 s of thruster operation, gives the impression of also being present at some of the other wavelengths, and can be considered a real physical phenomenon. (Persistence of these rocket fuel-originated molecular features after turnoff may arise from the protocol for shutting down liquid-bipropellant rocket engines.)

Figure 9 presents the ratios of signal summed within the 21 pixel-wide area in channels 1, 2, and 6 (from Figure 8) to HNO $000 \rightarrow 000$ band-dominated channel 5. (Coadding images of the further LIL firings would improve these noisy data.) This last ratio decreases significantly with increasing distance from the exit plane, for the reason we hypothesize in the following subsection. By contrast, the ratio of channel 2 to channel 5 evidences a distinct increase from D = 250 cm, where the exhaust density is $2\frac{1}{2} \times 10^{15}/cm^3$, to D = 500 cm - $2 \times 10^{14}/cm^3$, the distance at which it is no longer
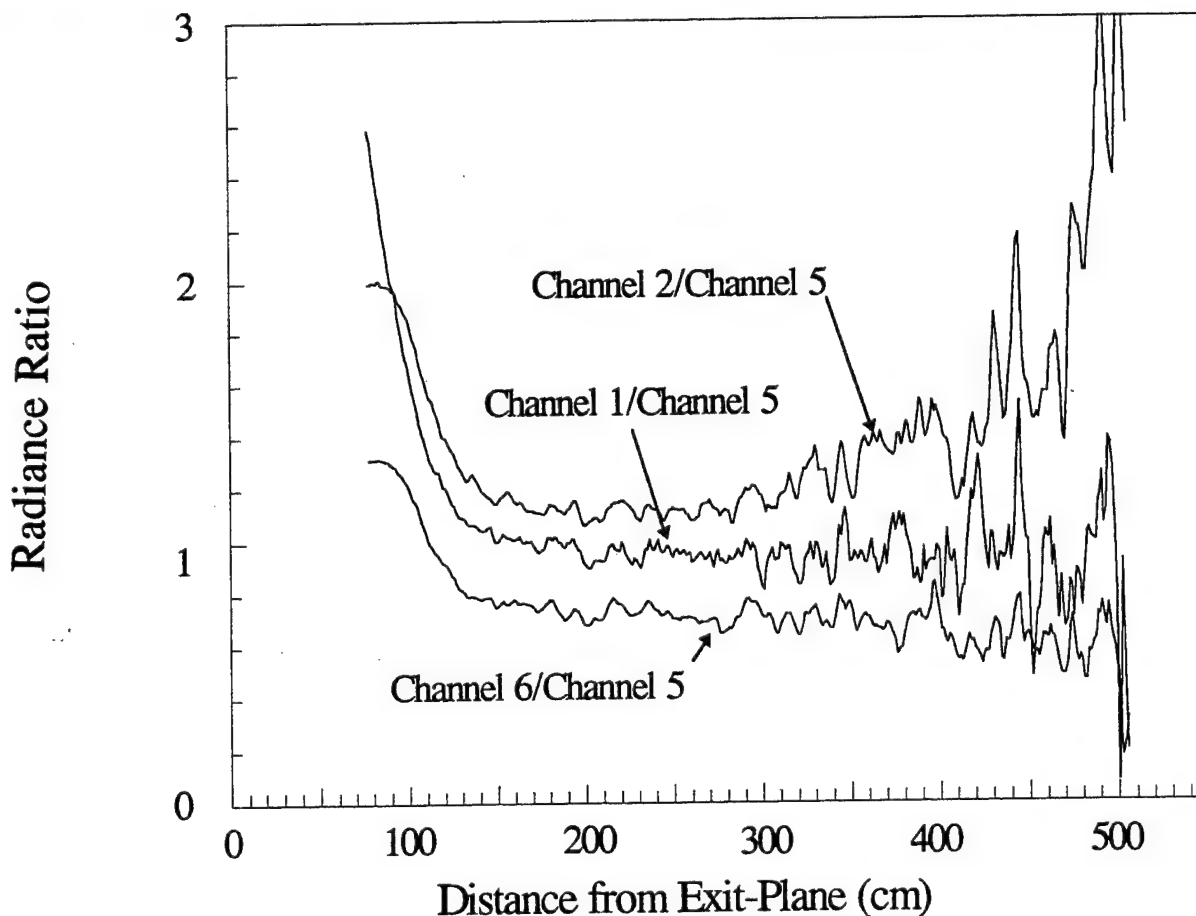
Figure 9. Ratios of time-averaged camera signals (from Figure 8).

detected by WINDEX, Thus, either the relative column and volume emission rate of HNO is decreasing or that of NO_2 is increasing downstream. The latter idea disagrees with our earlier argument that the effective rate coefficient for O + NO recombination becomes smaller as the gas density decreases away from the exit plane.

Furthermore, and more importantly, the near-axial signal in CN-dominated channel 1 closely tracks HNO-dominated channel 5. This finding is in contradiction with both the 1-D measurement and theoretical prediction in Ref's 33-34, as is further illustrated in Figure 10. Indeed, the fit of the model to the spatial distributions is rather poor.

Spectral radiances applying the sensitivities of each camera channel derived as described above (in Table 1) are included in Figure 2. These points represent ~10-cm longitudinal averages over the 3-s firing centered at 110 and 250 cm from the exit plane along the single-pixels scan line indicated in Figure 1, normalized to channel 3 at 250 cm. Similar data extracted from the higher signal/noise 21-pixel-averaged photocurrents are not substantially different from those plotted.

Discussion

These provisionally-calibrated, low-resolution WINDEX "spectra" agree with the higher-resolution Auroral Photography Experiment imaging spectra to the extent that they show a general increase of emission with wavelength. Major disagreements appear in channels 2 and 6, where the radiances appear anomalously large. The WINDEX observation that the fractional axial decrease in CN and CH bands-sensitive channel 1 is sensibly the same as in the channel that responds primarily to recombinant HNO* is contrary to the result reported from this previous experiment; the clear finding that the transverse profiles differ little from one another disagrees with the theoretical prediction that limb brightening takes place only in electronic bands of molecules requiring fuel derivatives for their formation; and the comparison among axial profiles (Figure 10) shows rather severe discrepancies not only between the previous image spectra and new spectral images, but also with the chemical-kinetic model.

These high readings in channel 2 may be due to error in identifying the actual filter installed for the experiment: spectral consistency would result if, for example, its FWHM were 30 instead of 20 nm, or if it had significant off-wavelength leakage or pinholes. (The filter transmissions provided are annotated with a claim of optical density-4 blocking outside the design wavelengths.) The enhanced signal in channel 6 may be from CN A $\rightarrow$ X radiation overlying the $NO_2^{*,\dagger}$ continuum, as this band system is predicted to be relatively strong by D = 120 cm.[34] This hypothesis is supported by the downstream decrease in ratio of channel 6 to channel 5 (Figure 9),
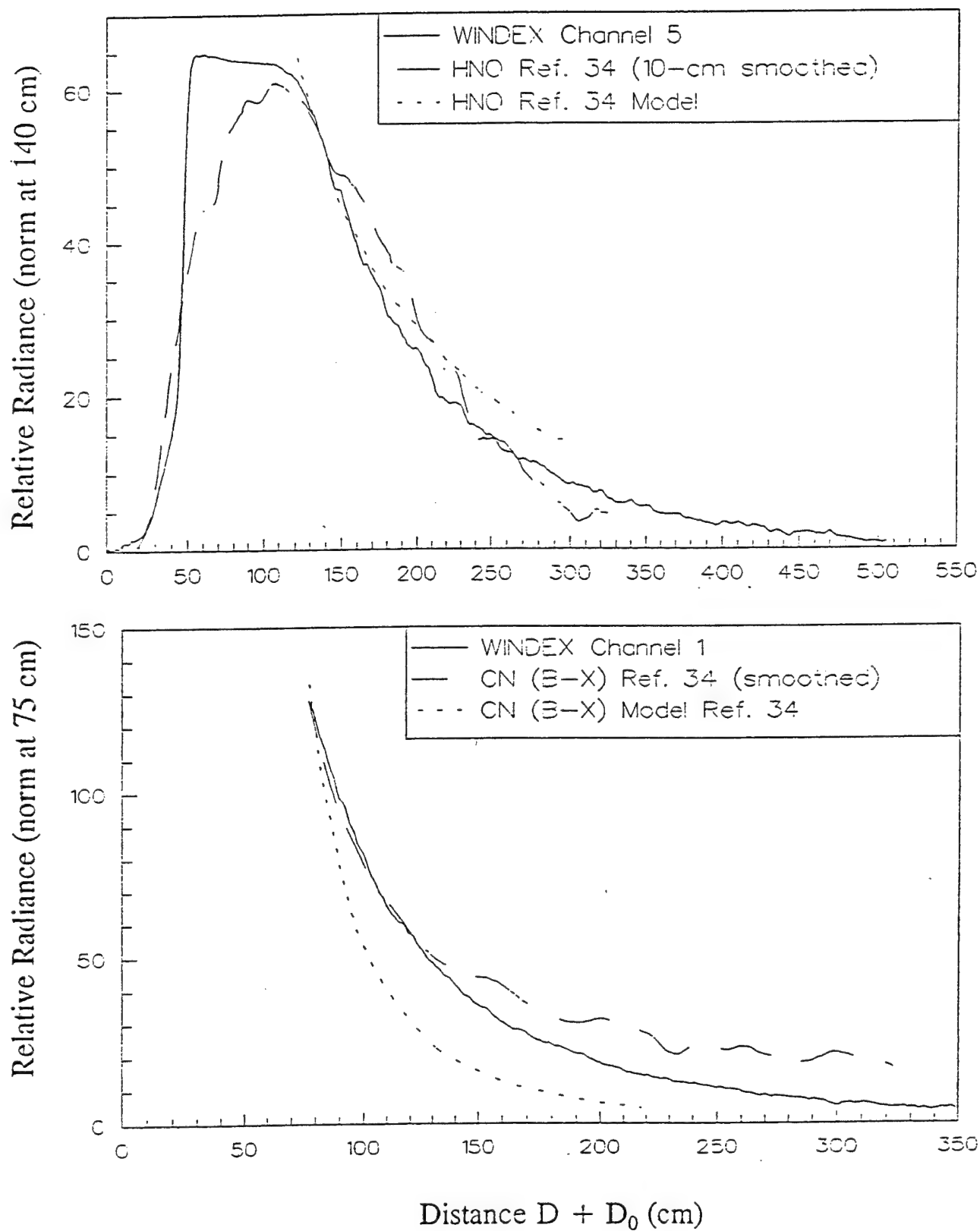
23

Figure 10.   Comparison of measured and predicted axial PRCS intrinsic core radiances, normalized at D = 75 and 140 cm.

insofar as the model also predicts that the highly temperature-sensitive CN-radical radiances fall off more rapidly axially than NO_2-HNO. Failure of these CN "red" bands to be resolved in the Auroral Photography Experiment may be an artifact of its sensor's end-to-end calibration, as such calibrations are notoriously subject to error toward the long-wavelength cutoff of red-sensitive photoemissive materials; further, aft cabin windows may differ among individual Shuttle Orbiters, and/or the aforementioned indirect measurement of this transmission near 800 nm could be in error.

The strongly increasing ratio of channel 2 to channel 5 signal downstream would disagree with the prediction that volume emission rates of NO_2 and HNO follow one another, unless the ratio of O to H concentration changes significantly due to chemical consumption of one of these recombinant atoms. Further, as we showed earlier, $NO_2^{*\cdot}\dagger$ emission weakens and spectrally shifts as the gas density decreases, which suggests that the effect of third bodies or temperature on excitative recombination of H with NO is different from that adopted for the chemical-kinetics model. (Indeed, a temperature dependence of the reaction rate coefficient could be extracted from these data.) Similarly, and more importantly (as we have stressed), the essentially constant axial ratios of column emission rates in channel 1 to channel 5 are in contradiction to the behavior expected. In addition, while the radiance distribution from channel 1 indeed shows limb brightening of the type predicted by the exhaust flowfield-chemistry model, this brightening is also pronounced in all of those WINDEX channels virtually void of signal from molecular bands whose excitation depends on the initial presence of fuel-fragment C_2H_2 precursor outside the oxidizer-rich near-axial combustion zone.

Also, unexplained and presumably of less importance is the $\sim 20\%$ increase in total yield of primarily CN-CH band radiation over the 3 s of PRCS operation. This enhancement could have its origin in increasing temperature of the combustion chamber walls, particularly since the rate of increase appears to be greatest just after ignition. (This channel 1 emission gives the impression that it would continue to grow if the motor continued to operate, an idea that lends itself to experimental test.) Persistence of these visible radiations is most likely an effect of the fuel-oxidizer shutoff procedure, with the somewhat longer duration signal in channel 1 due to a lag in stopping the flow of liquid fuel. Putatively CN bands containing channel 6 also evidences greater persistence than those camera channels sensitive primarily to HNO* and $NO_2^{*\cdot}\dagger$.

Recommendations

As noted initially, we have addressed these WINDEX images to the extent justified by the reliability of their current calibration. The angular field of the camera, "its plate scale" can be readily determined from photographs of a test target. Images of a NIST-traceable

uniform radiance source (available at PhotoMetrics, PL/Optical Physics Branch, and elsewhere) lead to 1) the relationship among the sensitivities of each filter channel (without the necessity of remeasuring wavelength responses); 2) the absolute dependence of output photocurrent on paraxial scene radiance; and 3) any variation of 2) on position in the image plane. Uncertainty in the camera's electronic gain does not affect the relative low-resolution spectral distribution derivable from its six channels, but would hamper verification of model predictions of the absolute radiances in molecular bands.

In this regard, the WINDEX photographs can be straightforwardly computer-rectified to projections normal to the axis of the exhaust chemiluminescence, that is, to a constant transverse distance scale in object space. Since this gas volume is in general optically thin to its spectrally-widespread electronic emissions, this correction leads to a visible spatial optical signature applicable to all projections of surveillance sensors. An accurate radiometric calibration would justify the effort to improve signal/noise ratios by various coadditions; for example, photocurrents from the ten L1L PRCS firings identified in Table 3 could be summed after the images from the sporadically re-pointed camera are registered, which would approximately double the downstream distance at which this signature is known (and in addition provide a better characterization of the grow-in/ decay of the visible emissions).

Our earlier approximate calculation of the kinetics of NO_2*·† suggests that additional analysis of the existing Auroral Photography Experiment spectra be performed to determine the dependence of this emission on local gas pressure and temperature. Even more important, the finding that the transverse (and also axial) radiance profiles of those features ascribed to fuel product-derived and other species differ insignificantly from one another bears strongly on the assumptions about PRCS engine phenomenology that are applied in the flowfield-kinetics model.

These initial results also lead to recommendations for future application of WINDEX to spectral imaging of thruster exhaust gases. We restrict the camera's view projection to that of this 1995 experiment, in part in the interest of cost-saving (much more effort would be needed to operate it in Orbiter's open payload bay) and also because blockage of the initial high-temperature ½ m of the exhaust stream reduces requirements for its dynamic range as well as for protecting its photocathode. (The model[34] CN B → X radiances viewing normal to the flow axis decrease by four orders of magnitude between D = 0 and 100 cm; these high brightnesses close-in inhibit viewing from distant "unshielded" positions, such as could be provided by the Remote Manipulator Arm or docked MIR spacecraft.) The camera projection should be accurately surveyed pre-flight, and held constant during the engine operation. Spectral images of the aforementioned calibration source through the aft flight deck window would determine its absolute transmission. While near-UV measurements unfortunately show

high attenuation by the routinely-used window at the ~ 385 nm of the first overtone of the CN B $\to$ X system, which offers the benefit of virtually no contamination from NO_2, a near UV-transmitting aft window is available.

Insofar as the radiance distributions of the intrinsic core remain essentially stable after engine turnon (channel 1 emissions perhaps being an exception), the time lost between acquisition of narrow-band images (in this WINDEX operation, about 7/8 of the thrust time) can be minimized by longer-duration sampling of the photocurrents from camera channels. A readily achieved factor six in total exposure length would lead to on-scale signal from NO_2 and HNO roughly twice as far downstream. (This change in operation of the camera would in turn would call for a corresponding increase in its field-of-view.) The high chemiluminescent radiances near the exit plane could be held on-scale by intermixing shorter exposures and/or CCD readouts; ~ 1-ms samplings would be effective. The STS-63 observation that PRCS exhaust radiation patterns do not depend on orientation of the thrust axis to Orbiter's trajectory quite obviously greatly simplifies requirements for future imaging: longer duration firings, without consideration of their angle to the flight path, would further extend the dynamic range of brightnesses.

The spectrum intervals in which the imaging system operates also lend themselves to improvement. For obvious reasons channel 1 could be narrowed, and even split in two to isolate CH emission, with present channel 3 eliminated. Channel 6 could be tailored to the CN A $\to$ X band structure longward of the HNO ^{1}A"$\to$ $\tilde{\text{X}}$ 000 $\to$ 000 band, to assess the signal in this largely-quenched feature.

These visible-range exhaust radiations are accompanied by ultraviolet electronic bands (OH, CO, and NH A $\to$ X, ...), whose emission rates and spatial distributions both bear on the kinetic processes and are themselves an element of the optical signature.[52] In consequence, complementing spectral imaging/imaging spectrography at UV wavelengths, such as by WSAI's GLO sensor operated from the payload bay (preferably, in a near-coaligned view projection) would be particularly effective in validating/improving models of electronic excitation in the intrinsic (or vacuum) core of PRCS thruster exhausts.

SURVEYS OF THE EARTH'S LIMB RADIATIONS
BY THE "GLO" IMAGING SPECTROGRAPH

Introduction

Radiations from the extreme ultraviolet to the long-wavelength infrared arise from resonant and fluorescent scattering of sunlight and earthshine, impact of photoelectrons, and excitative reactions in the mesosphere and thermosphere. Measurement of their brightness distributions, besides serving the obvious purpose of characterizing the scene backgrounds/foregrounds encountered in optical surveillance,[6,22,23] provides critical information about the composition, temperature, chemistry, and dynamics of the high-altitude atmosphere.[65-68]

Intensities of the various ultraviolet emissions in particular depend on the fluences of short-wavelength photons from the Sun, which alter the densities of optically active species, as well as on the fluxes of these photodissociating and resonant- or fluorescent-scattered photons. In consequence, UV limb profiles vary with phase of the solar cycle, latitude and season and time of day, and related geophysical factors. The multiple flights of space shuttle provide a unique opportunity for systematic surveys of the Earth's limb, in particular by sensors capable of scanning underground control or autonomously while its technical crew are resting or otherwise occupied. PL/WSAI's el-az platform-mounted "GLO" imaging spectrograph system[35] has this ability, and conducted such measurements[15-24] over part of the descending phase of recent solar cycle 22 as summarized in Table 4.

GLO was also pointed from Orbiter's payload bay to investigate the UV and visible radiations excited (and absorbed) by exhaust from its attitude-controlling thruster motors, due to the high-velocity spacecraft's interaction with the low-density atmosphere, and from astronomical sources ("UV-Star", on GLO-3). (The instrument also viewed thruster exhaust interactions through a long-focus telescope at the Air Force Maui Optical Site[10].) PhotoMetrics was involved with these other on-orbit experiments only through its contribution to operation of the sensor described below.

Applications of Limb Spectra

A comparison of the spectral ranges of dayglow and the several middle- and near-ultraviolet molecular bands that have been identified in thruster rocket exhaust appears in Figure 6 of Ref 6. (UV emissions also arise from interaction of high translational energy

28

Table 4. GLO Limb Airglow Measurements

GLO-	1	2	3	4
Shuttle Mission STS-	53	63	69	74
Orbital Inclination	57°	51°	28°	51°
Latitude at Local Noon	57°N	48°S	10°N	—
Dates on Orbit	2-9 Dec 92	3-11 Feb 95	7-18 Sept 95	12-20 Nov 95
PhotoMetrics Participation	—	3-11 Feb	30, 31 Aug; 7-18 Sept	9-20 Nov
Simulation Exercises	—	9-10 Jan; 13-15 Dec	5, 6, 24 July	—
Total hr Limb View (approximate)	30*	50	120†	50**
Sunlit hr (approximate)	25	30	70	40
Fractional moonlight illumination	0.56-0.99	0.17-0.86	0.97-0.31	0.73-0.04
A_p Index	2-12	2-30	3-39	3-10
10.7-cm solar flux (10^{-22} W/cm²Hz)	112-116	79-84	68-72	71-75
Tangent Heights (km)	80-330	80-400	80-400	80-400
Location on Spacecraft		Bay 12	Bay 11	Bay 5
Spectrograph Slit Orientation	Horizontal	Horizontal Night Vertical Day	Horizontal Night Vertical Day	Horizontal Night Vertical Day
Data Focus	Terminator	High Latitude	Equatorial	High Latitude

- - - -

* Best data 2-4 Dec, mission elapsed times 55:40 - 100:26 h

† Best data mission elapsed times 100 - 160 h

** Includes ~17 hr while Orbiter was docked with the "MIR" manned spacecraft

combustion products with the low-orbital atmosphere[10,51].) These features include NO gamma, CO Fourth Positive, and OH ultraviolet (A → X) bands, all of which are overlaid by natural radiations from the atmosphere's N_2 and NO. The strong atomic lines of airglow lie primarily at shorter wavelengths (≤ 1600Å), and while of considerable aeronomic interest, currently play no significant part in evaluating remote sensing concepts. By contrast, as visible wavelengths are now being considered for surveillance-tracking, the background scene radiances measured by GLO's >4000Å-sensitive spectrograph sections and filter cameras become of interest.

Applications of optical sensing to geophysics of the thermosphere have been recently reviewed in detail.[67] The altitude profiles of trace metal ions/atoms measured by GLO play a unique part in investigating dynamics of the ionosphere[6,15-21,24], in particular at near-equatorial latitudes where vertical transport of plasma is significant. Other issues of perceived DoD importance that would be addressed by this database include concentrations of (infrared-active) NO, which are readily extracted from the altitude profiles of its gamma bands (an initial estimate appears in Ref 6); total atmosphere density, from Rayleigh scattering of sunlight; geographic and time-of-day distributions of hydrogen atoms and ozone molecules, whose reaction produces OH airglow extending down to GLO's longer-wavelength sensitivity range, and of $N(^2D)$, the primary precursor of NO; and the temperature profiles that can be derived from atmospheric density scale heights and rotational distributions within electronic bands.

Sensor

The GLO system, an improved version of the University of Arizona Lunar and Planetary Laboratory's Imager/Spectrograph,[35] is composed of nine ~1000Å free spectral range 1-D imaging spectrograph units and twelve filter cameras covering ~1200Å - 11000Å, with their optic axes coaligned. As the airglow data from these electronic imagers appear to provide lower signal/noise, we have considered primarily GLO's spectra.

The spectrograph's field-of-view is 0.2° × closely 10° in its imaging direction. Photocurrents from elements of its final-stage photodetector array are routinely coadded to enhance signal at the expense of spatial and/or spectral resolution. Nominal best FWHM line spread is 4Å at the shortest wavelengths, increasing to 10Å near 10000Å. GLO was mounted toward the –y (port) side of Orbiter's payload bay on a dedicated elevation-azimuth scan platform driven by stepping motors, at the x (long) axis positions indicated in Table 4. The spacecraft's body was oriented to allow the sensor to scan in elevation over axial tangent intercepts from ~80 km to co-altitude (i.e., viewing horizontally) without obstruction of its

field of regard. Its viewing azimuth was always >30° from Orbiter's ram direction to minimize artifacts from spacecraft-induced glows, and also >30° from the Sun (and where practical Moon, whose illumination appears in Table 4) to avoid scattering within its optics.

At GLO-1 the spectrograph's exposure times were 30 s, with its horizontally-oriented field stepped vertically; in the later three missions they were typically 4 s in each 8 s. With the slit horizontal, its footprint on airglow near 100 km was typically 10 km vertically due to a combination of its finite natural projection and the unavoidable small misalignment and pitch-roll-yaw drifts of Orbiter's body.[6] With its long axis held vertical, daytime limb spectra were typically accessed over 100 - 250 km and 250 - 400 km intercept altitude ranges. To bring the weaker nightglow on-scale in individual spectrum samplings, the slit was oriented horizontally and photocurrents in the imaging direction were coadded.

GLO was operated autonomously, with a command uplink from NASA's relay stations communicating with its controller when Orbiter was within radio range (80 - 90% of the flight periods). Its data were relayed through a 110 kbyte/s and 55 kbyte/s communication channel, and its performance downlinked through two low-rate channels. A read/write magneto-optic disk recorder provided 500 Mbyte of storage between data transmissions (~30% less during the UV-Star experiment).

A PhotoMetrics staff member (J. Gardner) participated in round-the-clock operation of GLO 2, 3, and 4 from NASA-Goddard Space Flight Center and took part in the pre-flight simulation/training sessions as indicated in Table 4. He contributed to short- (one day ahead) and long-range (2 - 3 days) planning of the measurement sequences (in part on the basis of continuing analysis of the incoming spectra), and operated the sensor system in real time. A principal task was adjusting the angular limits of the el-az mount to achieve the desired ranges of atmospheric limb intercepts as the spacecraft's pitch-roll-yaw was changed to meet requirements of other onboard experiments.

A typical ultraviolet dayglow spectrum, reproduced from Ref 6 (Figure 11), shows the strong lines of upper-thermospheric (and extended solar-chromospheric) atoms shortward of OI 1356 and 1304Å; the NO γ bands reported in Ref's 6 and 22; the three comparably-intense N_2 electronic bands Vegard-Kaplan ($A^3\Sigma_u^+ \rightarrow X^1\Sigma_g^+$), Second Positive ($C^3\Pi_u \rightarrow B^3\Pi_g$), and Lyman-Birge-Hopfield ($a^1\Pi_g \rightarrow X$); resonant scattering of sunlight from F-region N_2^+ ions (which extends well into the visible); and one of the several metallic-atom and -ion lines (Mg^+ at 2872 Å). Several other UV features are identifiable in spectra obtained at other intercept altitudes-latitudes-solar elevations.
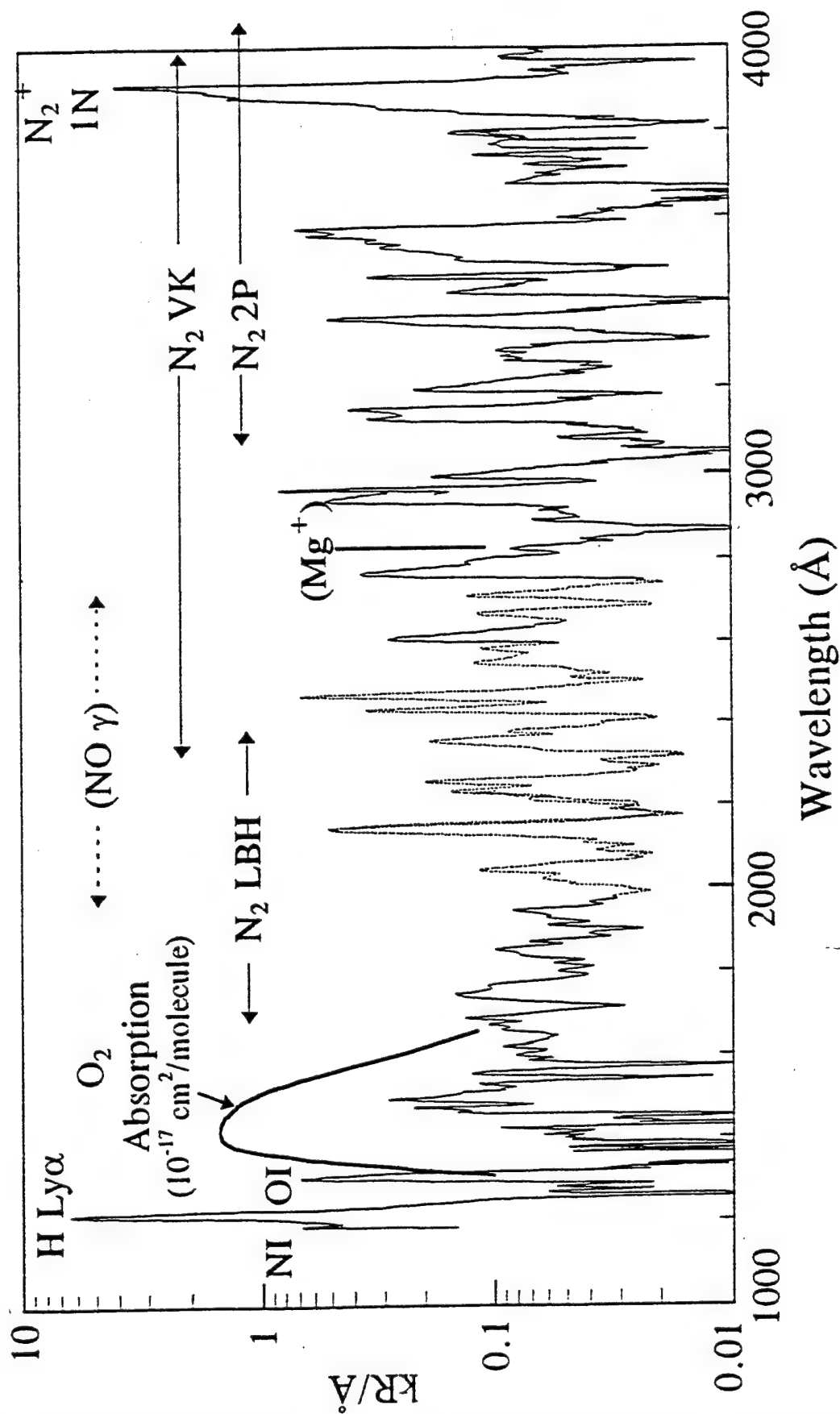
Figure 11. Typical ultraviolet daytime limb spectrum assembled from four adjacent GLO channels. The horizontal slit intercepted the equatorial atmosphere at 138-156 km, with the zenith angle of the retrograde-azimuth Sun 97° to 100° (at this intercept).

Absorption of short-wavelength L-B-H band radiations by O_2 in its Schumann-Runge continuum ($X^3\Sigma_g^+ \rightarrow B^3\Sigma_u^+$) represents an example of application of ultraviolet spectrometry to aeronomy, as it measures view-column concentrations and thus altitude profiles of oxygen molecules. A UV spectrum of the nightglow, and representative GLO limb spectra at longer wavelengths, are reproduced in Figures 12 and 13.

Diurnal Variation of NO and N_2 Backgrounds/Foregrounds

Figure 14 is a schematic comparison of the UV dayglow intensities from $10^{-5.4}$ relative concentration nitric oxide and 10^{-1} relative concentration molecular nitrogen, which represent a major interference with surveillance of ultraviolet-emitting thruster exhausts from orbital altitudes. (Viewing against the sunlit mesosphere and stratosphere, Rayleigh scattering also presents high backgrounds.) Since the absolute radiances vary with factors other than the elevation of the Sun, the ordinate scales are not intended to be the same. Column emission rates in the three aforementioned N_2 systems are comparable, as is indicated in Figure 11. Particulars of excitation-quenching-absorption of these radiations are in Sections 2 and 4 of Ref 6 respectively. (Ch in Figure 14 represents the Chapman grazing-incidence function[69].)

The N_2 electronic bands are excited by impact of photoelectrons (in some part through radiative and even collision-induced cascade), primarily those produced by the <305Å solar flux. As altitude profiles of nitrogen molecules, and also UV sunlight-absorbing oxygen atoms, vary little over the course of one day, the limb radiances vary regularly with the horizontal irradiances of these hard photons, that is to say, with the Sun's elevation. At night, these and the several visible and near-infrared N_2 bands essentially disappear.

By contrast, 1) the electronic bands of NO arise from its fluorescent and resonant scattering of middle-ultraviolet sunlight, to which the thermosphere is optically thin except in low-altitude, high-zenith angle propagation paths; 2) furthermore, 3) the concentrations of these molecules build up/decay significantly while the Sun is above the hard-earth horizon. (Vertical and latitudinal transport, in particular from the auroral region where nitric oxide is created by other than solar photon-initiated chemical reactions, also alter the NO concentration profiles.) Still further, the midday limb radiances peak at altitudes some 40 km below those of the N_2 bands (more near twilight), and some NO chemiluminescence in δ as well as γ bands accompanies recombination of the thermosphere's O and N atoms at night.

In consequence of observations 1) and 2), limb radiances in the γ ($A^2\Sigma^+ \rightarrow X^2\Pi$) and weaker ϵ ($D^2\Sigma^+ \rightarrow X$) and δ ($C^2\Pi^+ \rightarrow X$) bands of NO evidence the less
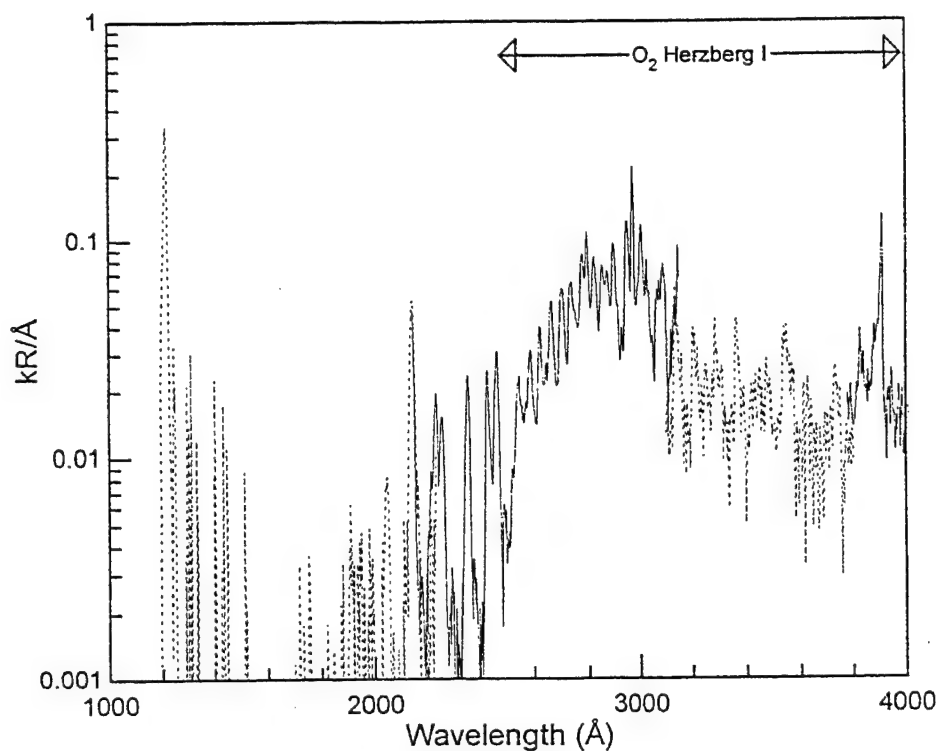
Figure 12a.   Typical GLO ultraviolet nightglow spectrum. Tangent height 100 km, solar zenith angle 106° at tangent intercept, 1.6°S latitude.
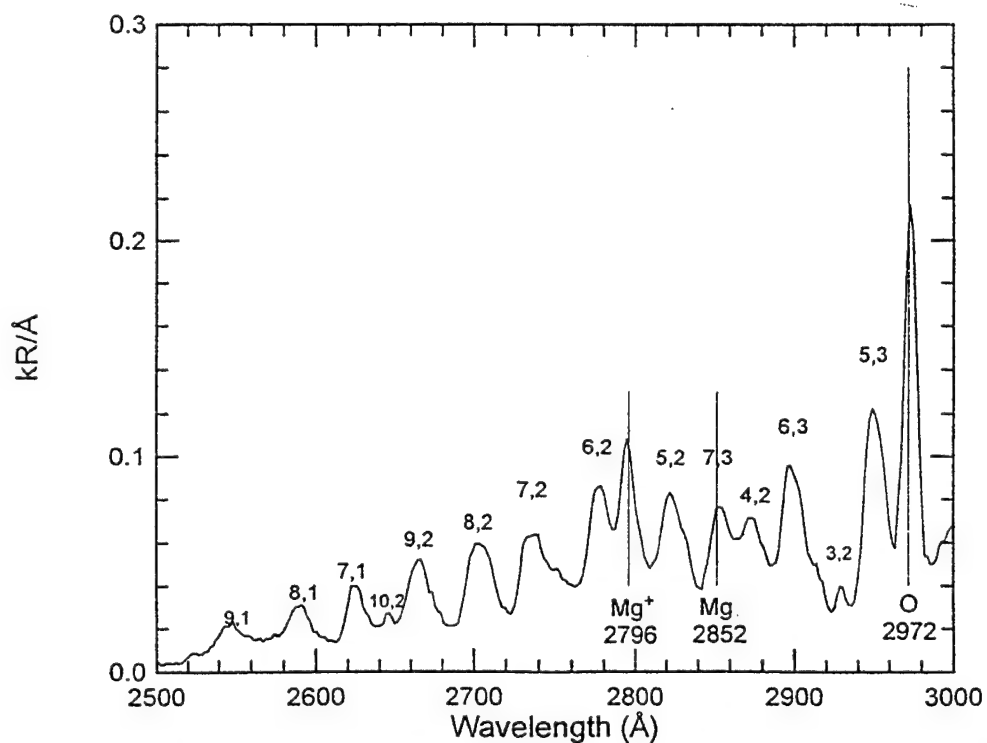
Figure 12b.   Enlarged UV nightglow spectrum, showing the O_2 Herzberg I ($A^3\Sigma^+_u \to X$) bands.
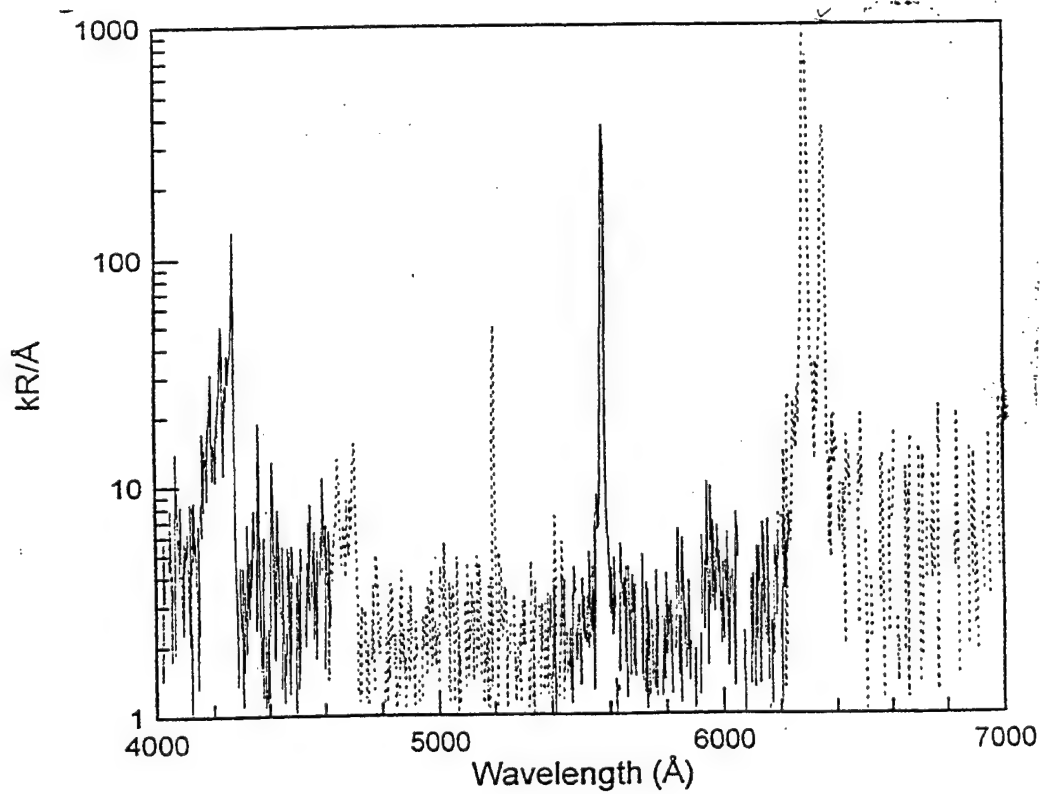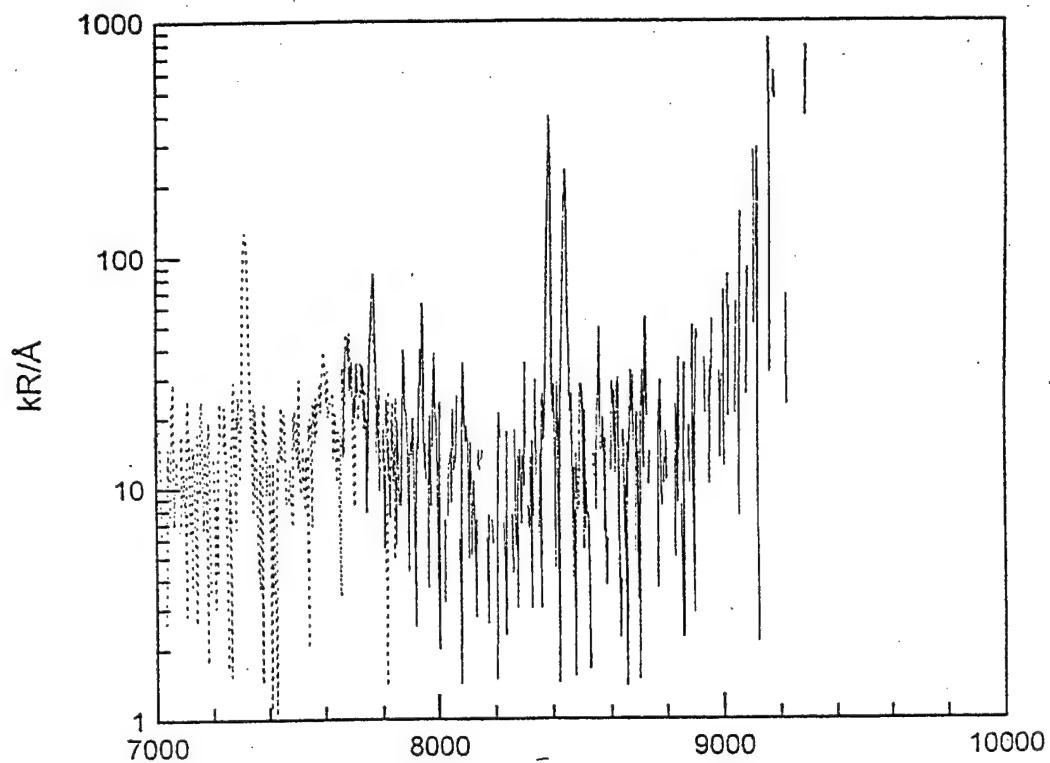
Figure 13a. Typical GLO-1 visible and near-IR dayglow spectra, from 192 km tangent intercept altitude, SZA 95°, 54°N latitude.
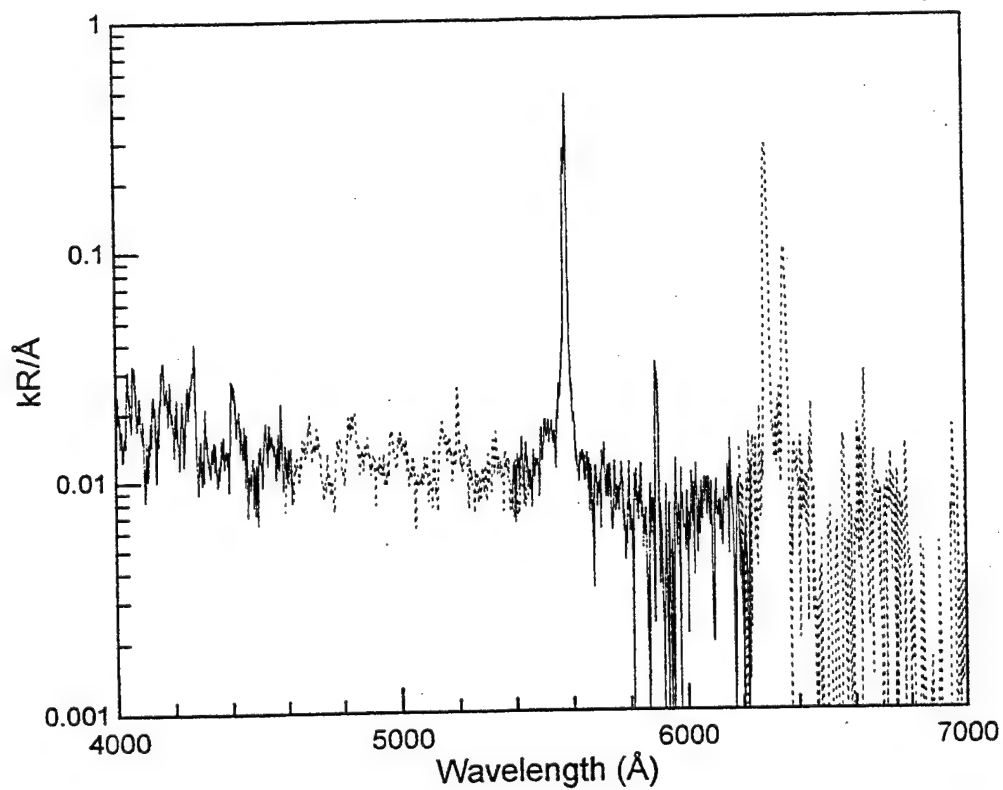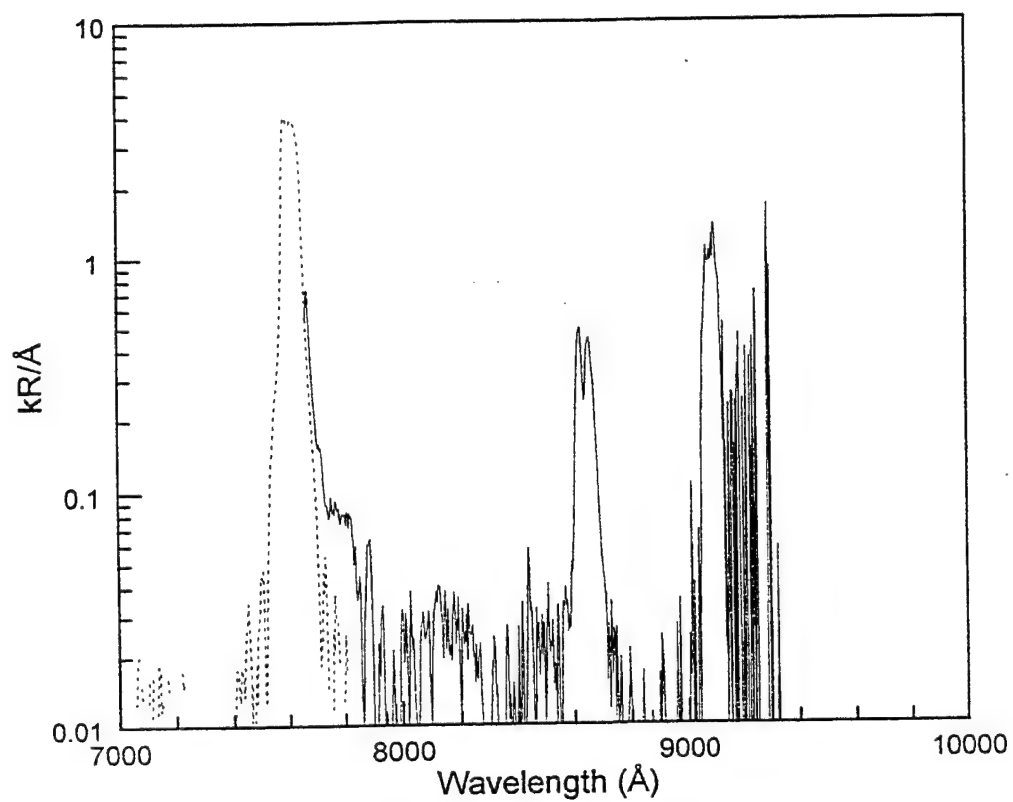
Figure 13b. Typical GLO-1 visible and near-IR nightglow spectra, from 100 km tangent intercept altitude, 1.6° S latitude.

36
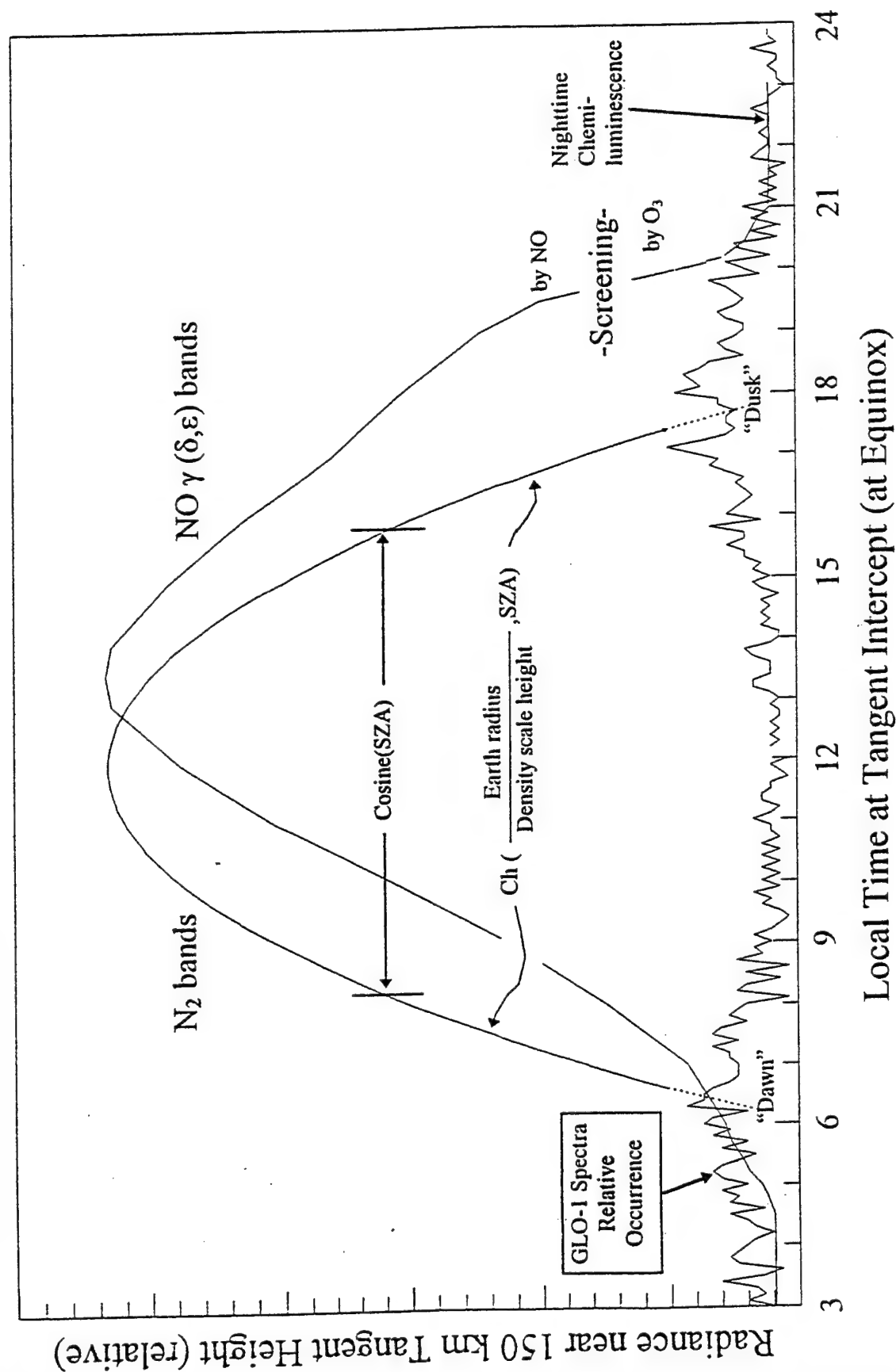
Figure 14. Schematic comparison of the diurnal variation of airglow from nitric oxide and nitrogen molecules. The radiance scales are intended to be relative. Ch refers to the Chapman grazing-incidence function[69], and SZA to solar zenith angle.

systematic and more complex diurnal variation indicated in Figure 14. As alluded to above, the exciting ultraviolet solar photons are outscattered by NO only along high-concentration sight paths, as are those photons scattered in the direction of spaceborne sensors. In addition, ozone screens ~2200 - 3100Å radiation in illumination and view paths traversing the stratosphere.

GLO Trajectories and Intercept Altitudes

The latitudes and solar zenith angles at which Earth-limb spectra were obtained are in part illustrated in Figures 15 for GLO-1 (reproduced from Ref 6) and 16 for GLO-2. (Similar housekeeping information from the two more recent shuttle missions have not yet become available.) Latitude-local time and latitude-longitude of single orbits of intercepts from GLO-1 and GLO-2 are shown in Figure 17; the spacecraft's low-orbital path is of course precessing in longitude. The trajectories of cycles of the first three flights in Figure 18 aid in identifying the latitude of local noon, as well as the region of limb data from those flights relative to the geomagnetic equator, where vertical plasma transport is significant. GLO-1 provided the unique near-solar terminator results on ultraviolet backgrounds from nitric oxide documented in Ref 6, along with the new findings about trace metals in the high ionosphere reported in Ref's 15 - 23. It also returned data on the less-than-systematically-varying altitude profiles of NO-band radiance at auroral latitudes, which were not considered in this initial analysis.

Figure 19 illustrates a measurement of sunlight scattering from Mg^+ at GLO-2, near 90° solar zenith angle and 60° N latitude at tangent intercepts 100-120 Km.

In GLO-3 ~60 h of continuous limb measurements were obtained with a single spacecraft orientation (tail to earth), which was selected to maximize the observation window while space shuttle's Wake Shield package was deployed as a free-flier. This geometry provides a unique data set, in that the 30°N-to-30°S thermosphere at all longitudes was viewed with <1 hr resolution at all times of day. That is, airglow profiles were accessed over the full range of near-equatorial solar elevations, providing in particular new information about transport and reactions of metal ions/atoms and the complexes considered to play a part in their formation/destruction.

38
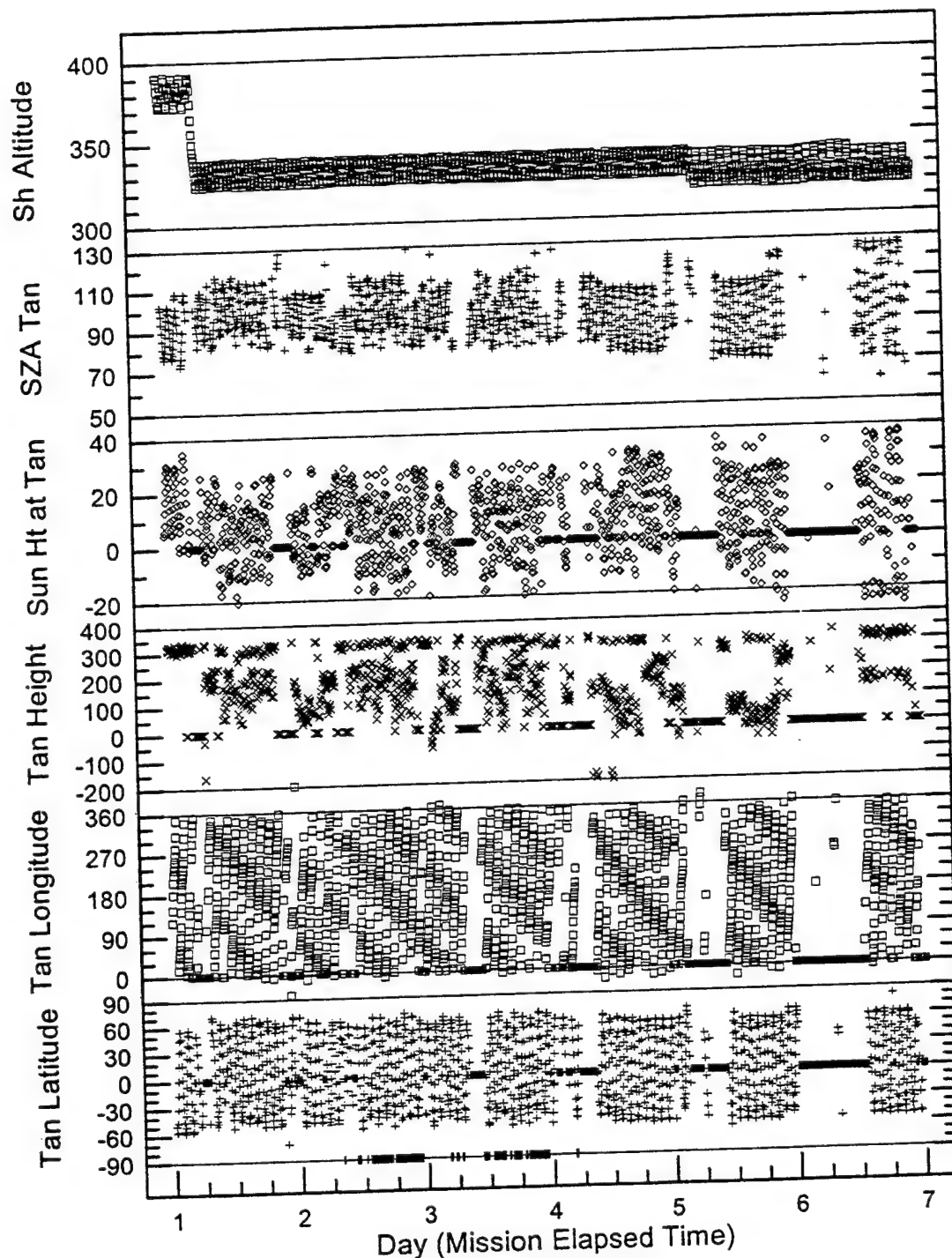
Figure 15. Geometry parameters of GLO-1, sampled at 5-min intervals. Reading downward: altitude of Shuttle Orbiter (km); zenith angle of the Sun at the latitude-longitude of the sensor field's tangent intercept (deg); elevation angle of the Sun at this tangent (90° – solar zenith angle); altitude (km), longitude and latitude (deg) of this tangent point. The thickened line at the bottom of the plot indicates the time periods of the dawn and dusk NO limb data analyzed in Ref 6.
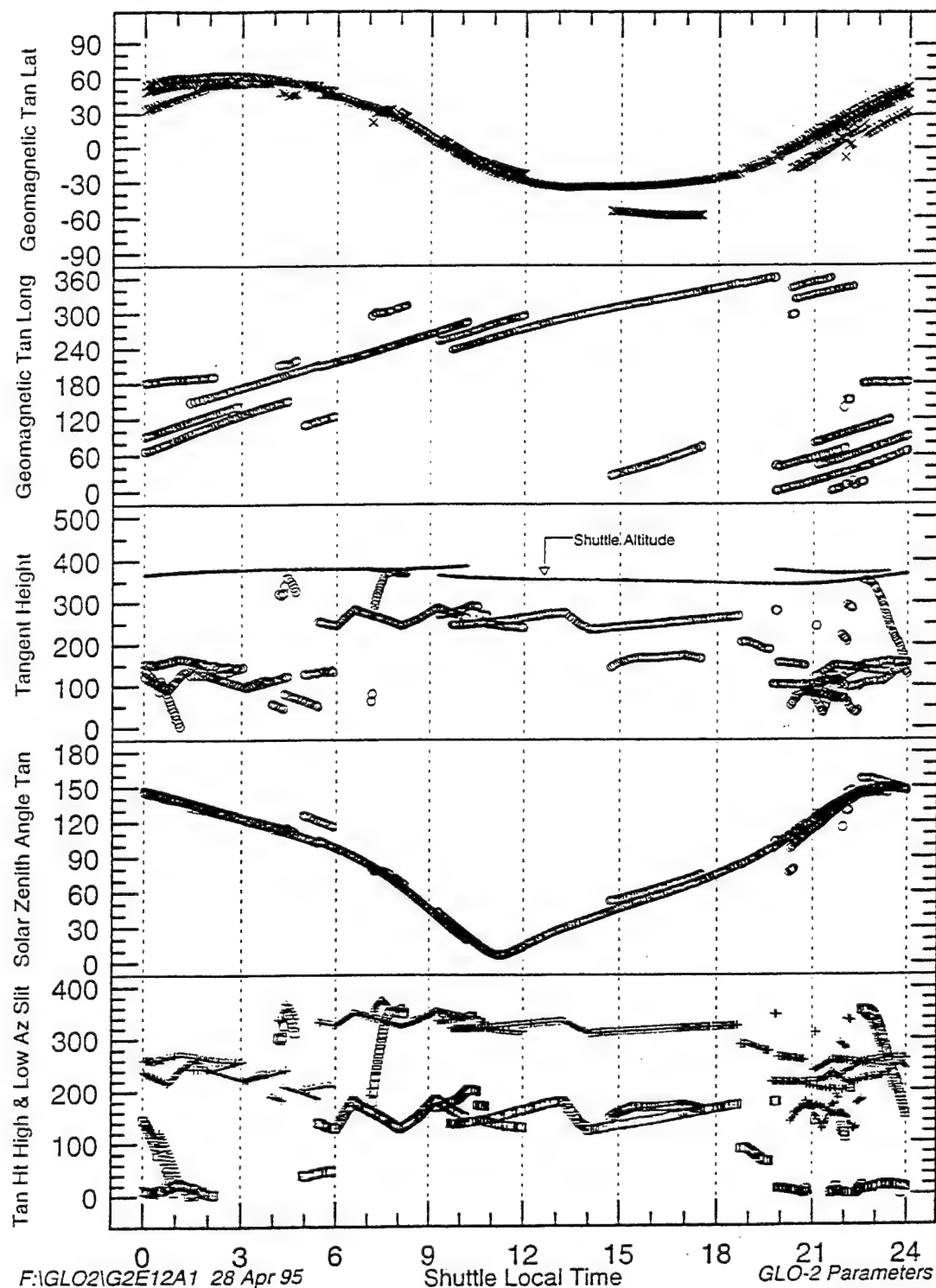
Figure. 16. Geometry parameters of GLO-2 on 4 - 5 Feb 1995. Reading downward: latitude and longitude of the tangent intercept of the geometric center of the spectrograph slit's projection (deg); tangent height of this intercept (km); maximum and minimum tangent heights of the projection (km); solar zenith angle of the central tangent intercept (deg).

40
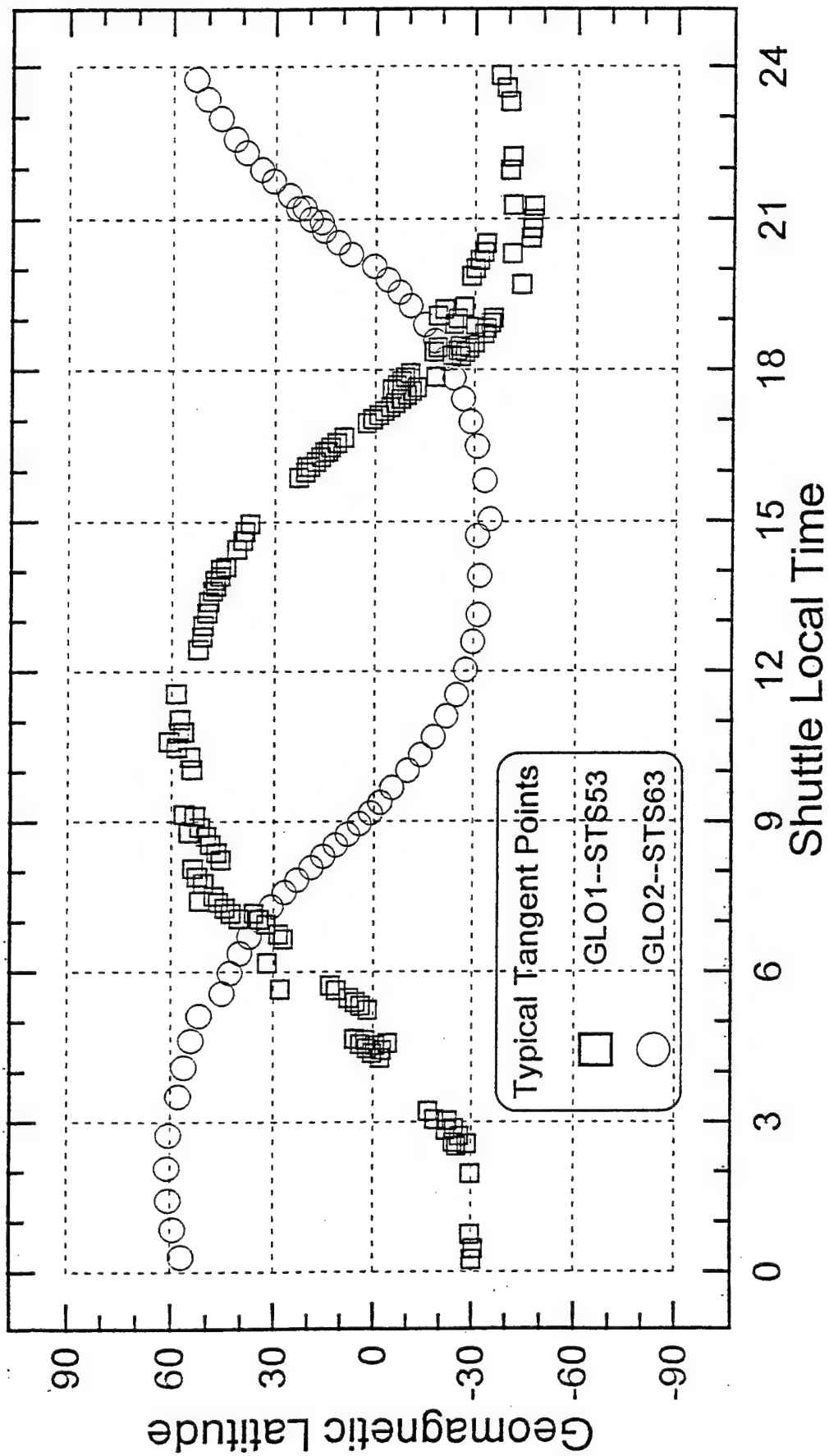
Figure. 17a. Typical tangent geomagnetic latitude (at the center of the spectrograph slit)-local time plots of the GLO-1 and GLO-2 series.
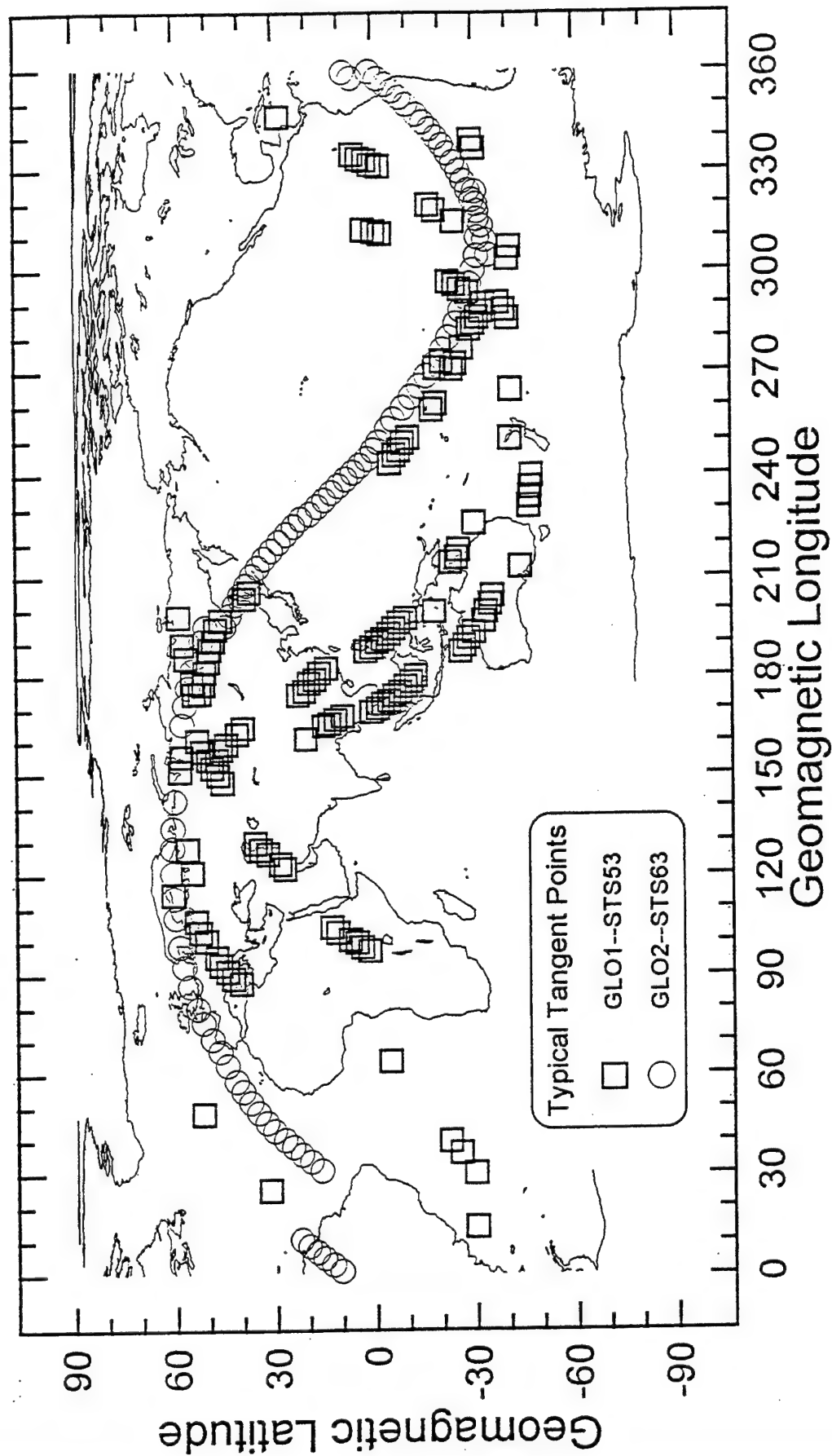
Figure 17b.   Typical latitude-longitude of the tangent intercepts of GLO-1 (2 orbits) and GLO-2.

42
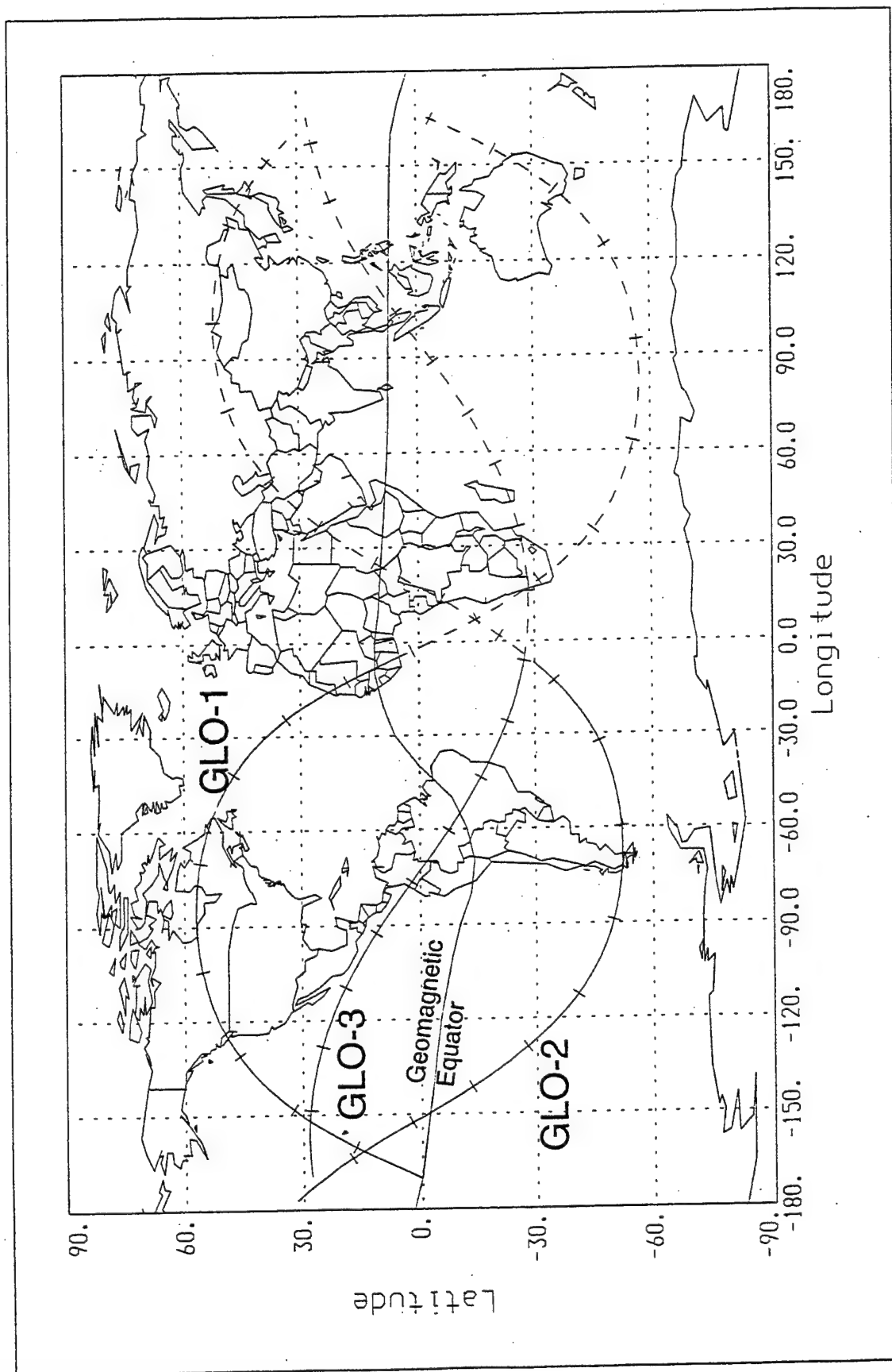
Figure 18. Typical trajectories of GLO-1, -2, and -3. Solid line segments represent sunlight illumination at the spacecraft's latitude-longitude, dashed signals nighttime.

43
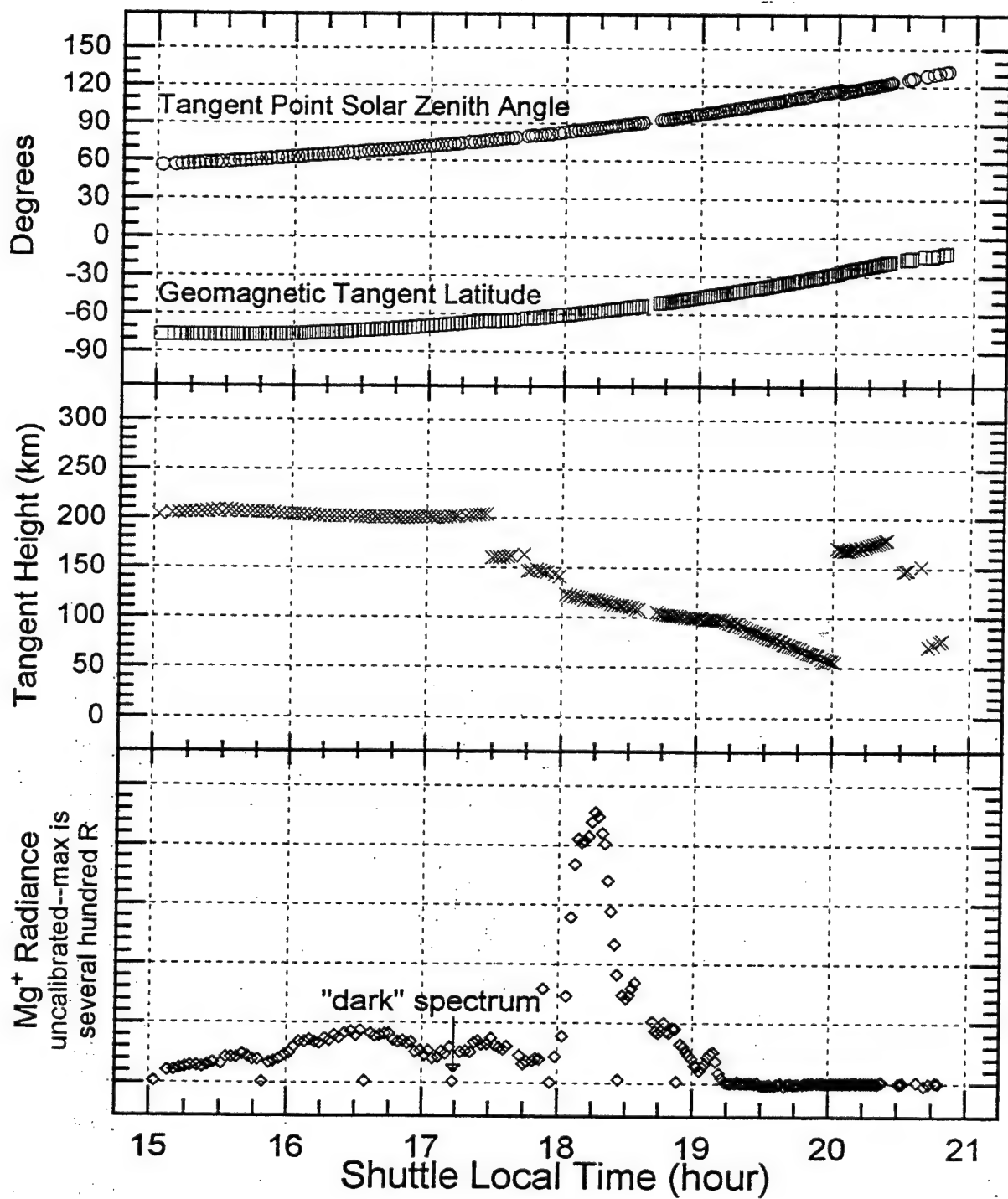
Figure 19.   Observation of Mg$^+$ 279.6 - 280.3 nm doublet on a GLO-2 terminator crossing.

SECTION 4

IDENTIFICATION OF THE SWIR-RADIATING SPECIES
IN THRUSTER EXHAUST-AIR INTERACTION VOLUMES

Technical Issue

Identification of the chemical species emitting between 2½ and 3½ μm following hypervelocity collisions of thruster rocket exhaust gases with the atmosphere's oxygen atoms is currently of considerable interest[5,14,70], in part because these wavelengths overlap thermal radiations from CO_2 and H_2O otherwise applied for optical surveillance. We show here that the excitation process(es) can be investigated using existing multi-filter cameras and spectrometers in groundbased tracking telescopes, and that supporting information can be derived from measurements from Shuttle Orbiter of the short wavelength infrared radiations that result from this spacecraft's routine releases of water vapor (a major component of thruster exhausts).

The two principal candidate SWIR radiations are the stretch bands (v_3, v_1) of H_2O arising from its non-adiabatic collisions on $O(^3P)$[47,71,72] and the vibrational fundamental sequence of OH from atom exchange reactions ($H_2O + O \rightarrow 2OH$) that leave one of the product radicals in an excited state[14,70]. The former emission would be accompanied by substantially weaker H_2O overtone and intercombination bands below 2 μm, which besides affording lower measurement signal/noise, call for modeling to identify and quantify the 001 and 100→000 (and nearby "hot band") transitions. (Bending-mode and pure rotational emission beyond ~5½ μm, while known to take place,[73] contributes little to understanding excitation of the water stretch modes.) By contrast, the $\Delta v = 1$ hydroxyl bands would be accompanied by $\Delta v = 2$ emissions centered near 1.5 μm, which would have comparable total intensity if the probability of populating OH vibrational levels about the third is significant. The ~2.8 – 3.5 μm OH fundamental sequence can be scaled from this first-overtone radiation, in particular when the instrumental resolution is sufficient to assess intensities of individual rovibrational features.

Equally important, the water bands lie at somewhat shorter wavelengths than the hydroxyl fundamental. Thus, contributions from the two mechanisms can be determined from the spectral distributions between 2½ and 3½ μm, as well as from the ratio of intensity in this wavelength interval to that between ~1¼ and 1¾ μm.

Filter Photography

This approach is to image from a ground station interactions of space shuttle's control thruster exhaust in restricted short-wave infrared intervals, whose specification to separate the two types of vibrational emission we initiate here. PL/WSAI's "IRIM" six-channel camera, or previously-used "Amber" camera,[14] would provide the spectral selectivity and radiance response required.

Past experiments have shown[5,11,14] that the posigrade volume from which SWIR emerges becomes essentially stable in Orbiter's moving reference frame by closely 1 s after ram-directed Precision Reaction Control System thruster firings start. We can therefore improve signal/noise ratios by increasing the camera framing (dwell) times to near the ~10-s exhaust-injection period allowable by NASA practice, and also enhance spatial resolution by adjusting the telescope's field-of-view to encompass and follow the high-brightness central area of these interaction glows. If the vibrational development of product hydroxyl that has been derived[70] from laboratory crossed-beam measurements[74] applies also to the on-orbit exhaust conditions, signal/noise in (for example) a 2.8 - 3.2 μm camera channel (somewhat longward of the water bands) would be as high as it was in the 2.3 - 3.6 μm Amber images of the windward PRCS firing from shuttle mission STS-56.[14] (In the unlikely event that the necessary narrowing of camera wavelength intervals turns out to result in subthreshold photocurrent from individual pixels, total radiant intensities could be extracted by coadding, i.e., converting the "spectral imager" into a simple filter radiometer.)

Relative spectral radiances transmitted to the Air Force Maui Optical Site at 45° depression from the spacecraft have been calculated from these laboratory data and related observations.[70] These best-estimates are reproduced in Figure 20, overlaid by the assumed/nominal 0.4-μm full-width bandpasses of the optical filters currently planned for IRIM. (Since the combination bands of H_2O shortward of 2 μm are expected to be an order of magnitude weaker than the familiar stretch bands they have been omitted.) The transmissions-at-normal-incidence shown, i.e., spectral "shapes", are taken from standard interference filter manufacturers' literature (Melles Griot, Barr Associates); filters with similarly steep cutoffs, flat tops, and maximum absolute transmission are available with FWHM's between about 2% and 50% of the center wavelength specified, in diameters large enough for imaging with fast camera lenses.

In Figure 21, we have placed three of these already-planned and by no means optimum filter characteristics on the calculated relative spectral intensities transmitted to the mountaintop station. This comparison illustrates the critical ideas that 1) OH

46
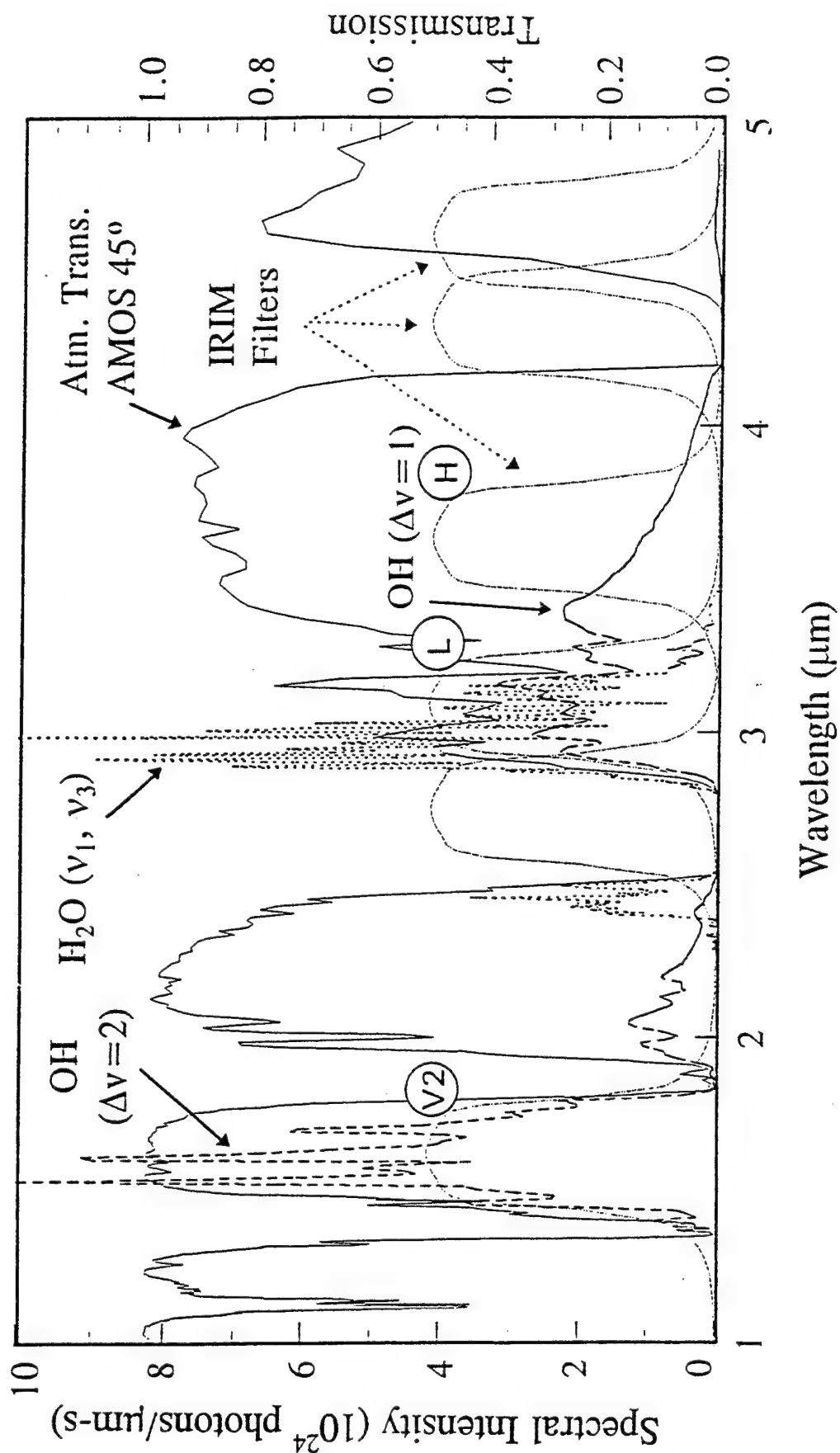
Figure 20. Derived endoatmospheric spectral radiant intensities of the candidate infrared species, atmosphere transmission, and nominal transmission of IRIM interference filters.
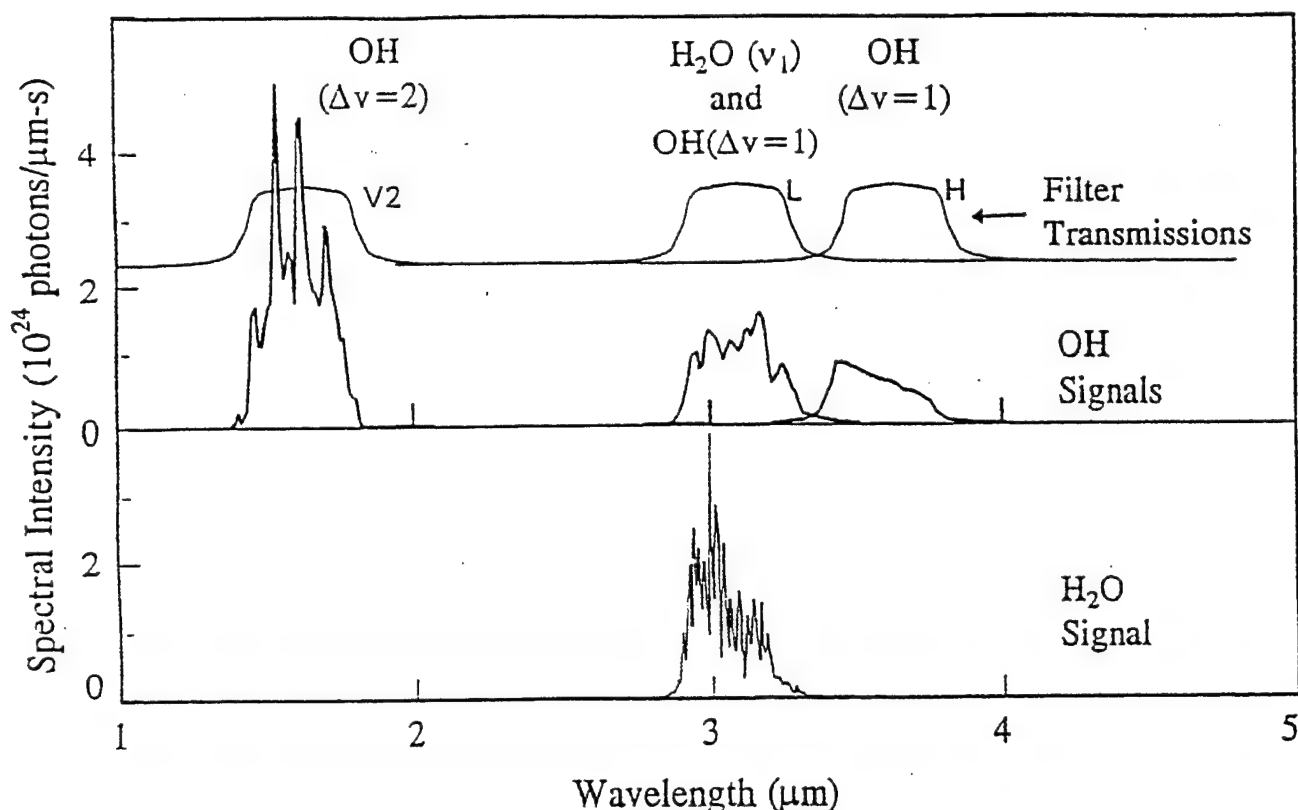
Figure 21.   Derived spectral intensities transmitted to the ground station.

vibrational fundamental radiation can indeed be isolated from the H_2O stretch bands with high reliability and 2) the OH $(\Delta v = 1)/(\Delta v = 2)$ ratio can be measured with sufficient signal/noise to further assess the part played by H_2O† (if any) and in addition extract OH vibrational "temperatures." In this regard, the hydroxyl overtone is almost completely transmitted by the intervening atmosphere and thus presents little interpretive difficulty. (Unfortunately, the lower atmosphere is much too bright at the ≥ 5-μm wavelengths of pure rotational bands of H_2O and OH to allow measurement of the rates of production of OH radicals from ground stations.)

Table 5 gives estimates of the sensitivity of this groundbased-imaging approach using the three interference-filter channels in Figure 20. These results are based on the best-fit vibrational and rotational temperatures derived previously,[14,70] the transmission of the LOWTRAN-model clear subtropical atmosphere in 45°-elevation paths to Shuttle Orbiter from the Air Force Maui Optical Site (the results are in fact insensitive to the water vapor profile adopted), a 100 kW SWIR output from "mature" PRCS ram interaction volumes as measured at STS-56,[11,14] spectrally-uniform quantum efficiency of IRIM's HgCdTe photodetector (or equivalent), and the peak transmissions of (readily-available) optical filters such as are shown in Figure 20.

48

Table 5.   Sensitivity Estimates

Filter Identification	V2	L	H	H/L
Center wavelength (μm)	1.3	3.1	3.6	
Spectral FWHM (μm)	0.4	0.4	0.4	
Signal OH† (10^{23} photons/s)	7.5	4.0	2.5	0.625
Signal H_2O† (10^{23} photons/s)	~0	5.1	0.06	10^{-2}

This simple imaging with three of the narrow-band filters already planned for IRIM can be seen to resolve effectively the issue of relative contribution to the SWIR signal from the reactive and non-reactive exit channels of hypervelocity H_2O-O collisions.   Further straightforward filter design (recall that the camera has six channels) would result in substantially better spectral isolation, even in the event that the radiation "temperatures" of these interaction-volume species differ from those currently favored.

Application of a Fourier-Transform Spectrometer

Infrared spectra of space shuttle's exhaust interaction volumes would be even more effective in determining the molecular source(s) of their SWIR emission.   We show in this subsection that sufficient signal/noise is available in measurements by an available Michelson interferometric spectrometer[75] (Bomem MR-2XX) operated in conjunction with a groundbased tracking telescope, such as the 3½-m-diameter unit at Starfire NM or the ~1 - 2-m units routinely used at the Air Force Maui Optical Site.   The aperture of this telescope does not affect the radiometric throughput of the spectrometer, but determines only its "footprint" on distant glowing volumes; any of these telescopes would isolate a physically-appropriate area of PRCS exhaust interactions.

From the specifications in the manufacturer's literature (further clarified by telecons with his staff), we calculated the expected noise equivalent spectral radiance (NESR) for three of the photodetector types available for this spectrometer (Table 6).   We take InGaAs, whose FWHM power response wavelengths are 1.0 and 1.7 μm, as representative for estimating signal-to-noise ratios in the hydroxyl overtone region.   As our first-principle sensitivity calculations based on performance of this focal plane detector did not agree with the manufacturer's (actually more pessimistic) figure, we proceeded to scale the response of the spectrometer to its recent measurements of rotational line intensities in the natural hydroxyl nightglow, for which InGaAs and germanium detectors had been used.

Table 6. Spectrometer Characteristics*

Focal-Plane Detector	-D11E	-D20E	-D60D	
	(HgCdTe)	(InSb)	(InGaAs)	
Detectivity of material	3×10^{10}	1×10^{11}	4×10^{12}	cm-Hz$^{\frac{1}{2}}$/W
NESR Calculated from detectivity	3.5×10^{-9}	1×10^{-9}	2×10^{-11}	W/cm^2-sr-cm^{-1}
NESR from mfr's literature	5×10^{-8}	5×10^{-9}		W/cm^2-sr-cm^{-1}

* Sensor etendue 4×10^{-3} cm^2-sr, transmission 0.15; signal integration time 2 s; spectral resolution 1 cm^{-1} (compare rotational separations in OH and H$_2$O, ~ 15 and 10 cm^{-1}).
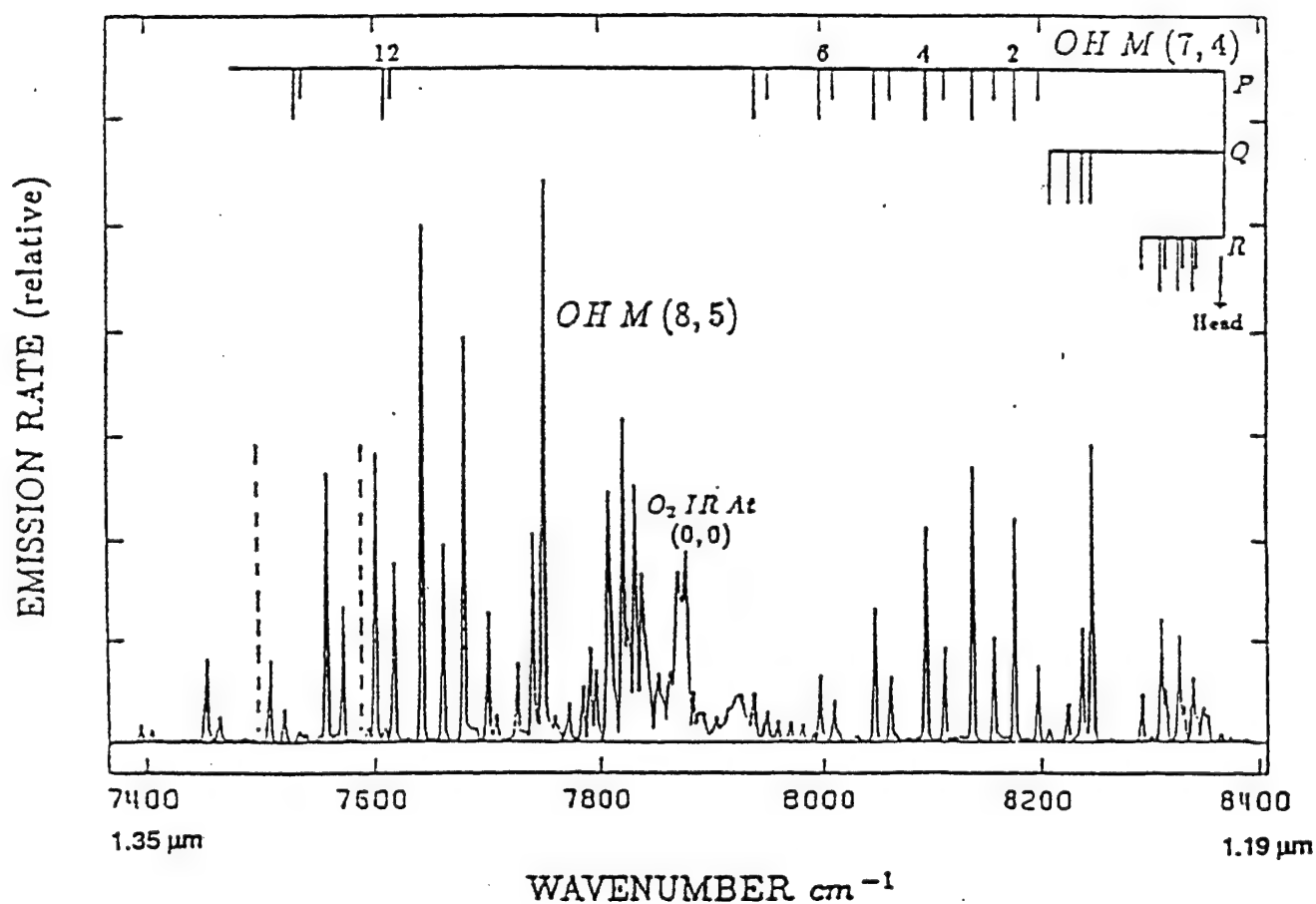
Figure 22.   Hydroxyl nightglow measured with the Fourier Transform Spectrometer. M refers to Meinel vibrational bands.

50

An integration time of about 1000 s resulted in good signal/noise (apparently ~20) in the OH $\Delta v = 3$ sequence[76], as shown in the ~3 cm^{-1} resolution spectrum reproduced in Figure 22. In the roughly 3 times more intense, longer-wavelength $\Delta v = 2$ sequence comparable signal/noise was later achieved with this instrument in 100 s[77]. The zenith radiance of OH 7,4 band nightglow is 15 kilorayleighs spread over some 200 cm^{-1}, equivalent to an "average" spectral radiance of $1\frac{1}{2} \times 10^{-12}$ W/cm^2-sr-cm^{-1}.

By comparison, images of the STS-56 ram interaction volume obtained by the AMOS Amber camera[14] showed its peak absolute 2.3 - 3.5 µm radiance to be 3×10^{-7} W/cm^2-sr at 1 s after PRCS ignition. (The maximum surface radiances had been factors 2 or 3 higher at earlier times.) Spread evenly over the closely 1000 cm^{-1} between these two sensor wavelengths, this measurement would lead to an "average" spectral radiance of 3×10^{-10} W/cm^2-sr-cm^{-1} in the $\Delta v = 1$ hydroxyl sequence. From this figure we estimate $1\frac{1}{2} \times 10^{-10}$ W/cm^2-sr-cm^{-1} in the $\Delta v = 2$ sequence, which can be seen to be roughly 100 times the spectral radiance of the 7,4 hydroxyl nightglow band in Figure 22; it also is about a factor 10 above the NESR calculated (in Table 6) for an InGaAs photodetector in the Fourier transform spectrometer.

In consequence, to achieve the same signal/noise as these hydroxyl-nightglow measurements, an integration time of $[(1/100)^2 \times 1000 \text{ s}] \approx 0.1$ s would suffice (assuming the transform Fourier-spectrum to be reduced with the same high resolution). The more recent OH $\Delta v = 2$ nightglow data[77] lead to roughly the same integration time for measuring the spectrally-similar radiation from ram interaction volumes.

Resolution in the above-mentioned airglow spectrometry is substantially better than required for determining the relative contributions of OH ($\Delta v = 1$) and H$_2$O (v_1, v_3) to the "SWIR" signal. Synthetic spectra indicate that 10 cm^{-1} FWHM spectral resolution would reliably isolate these emission features, and would furthermore identify the individual hydroxyl bands.

Accuracy of pointing and tracking on the emitting region is important in Fourier transform spectrometry, as changes in absolute scene radiance during scans result in sloped interferograms that can be corrected only at the cost of degraded wavenumber resolution and additional noise. Thus, the sensor pointing should be maintained near a constant-radiance area of the exhaust-interaction region during the data integration (i.e., spectrometer mirror-movement) period. As noted, WSAI's existing Amber-camera images of the infrared radiance distribution of ram interaction volumes provide a basis for tracking the groundbased telescope's field-of-view to minimize changes in scene brightness while spectra are being acquired.

Water Ventings

Spectral imaging and imaging spectrography from onboard Orbiter of the dense vapor from its flash evaporations[45] and releases of excess liquid water[4,7] are straightforward, cost-effective means of determining optical cross-sections of H_2O at collision energies about half those from ram-directed exhaust. These vapor clouds offer the further benefits of being free of other combustion products and uncontaminated by the strong close-in "intrinsic core" chemiluminescence of some of the exhaust gases discussed in Section 2.

Water vapor, in addition to being a major component of thruster motor combustion due to its outgassing and venting, is the principal effluent from low Earth-orbiting spacecraft. The closely 3-eV translational energy of this gas relative to the thermosphere's essentially static O atoms is high enough to allow excitation of several of its low-lying vibrational and higher rotational levels, as well as upper states of OH and also H_2O^{+72}. However, the cross-sections for populating the large number of accessible vibrational states, their rotational development, and the branching ratios from and further collision-induced interchange among them are not nearly well enough understood for reliable calculation of the resulting "near-field" infrared radiances, or for prediction of the relative contribution of H_2O† and OH† to broad-band radiometer signals.

Some information about this foreground infrared contamination has recently come from onboard filter radiometry[71] and high-resolution Fourier transform spectrometry[73] of Orbiter's collisionally-excited outgas. The signal-to-noise and far-field background ratios achieved by the spectrometer ("CIRRIS") are adequate to identify the most intense vibrational band of neutral water longward of 4 μm (its v_2 fundamental) and several of its longer-wavelength pure rotation lines. These spectra also provide inferences about the v_1-v_3 and multiquantum transitions that could be producing radiation between ~ 1.7 and 3.1 μm.

When surplus liquid water is ejected from Orbiter, about 12%, or under normal stationkeeping conditions 2 g/s, vaporizes within 5 m of its venting orifice[4]. (See Appendix B.) The resulting column densities of this H_2O gas are greater by factors from very roughly 300 (within a few m of the narrow cloud of ice/water particles into which liquid streams fragment) to 10 (in the rearward hemisphere) than those typically resulting from surface offgassing one day or more after launch. Furthermore, Orbiter's flash-evaporations are responsible for as much as an order of magnitude higher column densities of gaseous H_2O than these liquid releases.[45]

These large density enhancements result in comparably increased impact-excited infrared radiances, which offer the opportunity (extremely difficult to attain in the laboratory) to identify individual transitions and derive rotational temperatures. They also lead to relative,

and with the aid of numerical flowfield simulations absolute, optical cross-sections. In addition, the volume emission rates may turn out to be sufficiently high within a few m of the vapor source to allow measurement of visible radiances and spectra, from excited electronic states of $O(^1D$ and perhaps even $^1S)$ and from OH†. The fields-of-view and wavelength response of the IRIM and GLO spectral imagers could be configured to view this water vapor from onboard Shuttle Orbiter, or from nearby subsatellites (such as the SPAS) or MIR (Appendix C); GLO's imaging-spectrograph elements could also be applied to measure column intensities in these lines and bands.

REFERENCES

1. D. L. A. Rall and I. L. Kofsky, Analysis of IBSS Spectra of Space Shuttle Control Engine Exhaust, PL-TR-92-2174, 31 May 1992, ADA261749.

2. D. L. A. Rall, I. L. Kofsky, and J. A. Gardner II, Analysis of Images and Spectra of Spacecraft-induced Radiations, PL-TR-92-2178, 19 July 1992, ADA 257902.

3. D. L. A. Rall, I. L. Kofsky, D. J. Knecht, E. Murad, and C. P. Pike, Persisting Radiation from Interaction of Solid-Propellant Exhaust Gases with the Atmosphere, Paper B-8, *Proceedings of the 1993 Meeting of the IRIS Specialty Group on Targets, Backgrounds and Discrimination*, IRIA-IRIS, Vol. I, pp. 53-76, July 1993. (Appendix B)

4. J. A. Gardner II, D. L. A. Rall, C. A. Trowbridge, I. L. Kofsky, R. A. Viereck, E. Murad, C. P. Pike, A. T. Stair, Jr., and A. Setayesh, Optical Properties of Water Released in Low Earth Orbit, *Society of Photo-Optical Instrumentation Engineers Proceedings* 1754, Optical System Contamination: Effects, Measurements, Control III, ed. A. Peter Glassford, pp. 124-132, 1992. (Appendix A.)

6. D. L. A. Rall, J. A. Gardner, and I. L. Kofsky, Analysis of Ultraviolet Spectra of the Sunlit Atmosphere's Limb, PhotoMetrics, Inc, 18 July 1995.

Journal Publications and Conference Presentations
(Refer to identification of PhotoMetrics' contribution in the Foreword)

I. Phenomenology of Liquid Releases in Near-Space (also Ref 4) Effort suspended 1992.

7. I. L. Kofsky, D. L. A. Rall, M. A. Maris, N. H. Tran, E. Murad, C. P. Pike, D. J. Knecht, R. A. Viereck, A. T. Stair, Jr., and A. Setayesh, Phenomenology of a Water Venting in Low Earth Orbit, *Acta Astronautica* 26, 345-357, 1992.

8. J. A. Gardner II, D. L. A. Rall, I. L. Kofsky, A. Setayesh, and E. Murad, Liquid Dispersal Study: A Proposed Space Shuttle Liquid Release Experiment, Paper AIAA-92-0793, *30th Aerospace Sciences Meeting*, Reno NV, 6-9 Jan 1992.

9. J. A. Gardner, D. L. A. Rall, I. L. Kofsky, A. Setayesh, and E. Murad, Liquid Dispersal Study: A Proposed GAS Experiment, *NASA Small Shuttle Payloads Symposium,* Greenbelt MD, 21 October 1992.

II. Thruster Engine Exhaust and Interaction Radiations (also Ref 3)

10. A. L. Broadfoot, E. Anderson, P. Shepard, D. J. Knecht, R. A. Viereck, C. P. Pike, E. Murad, J. E. Elgin, L. S. Bernstein, I. L. Kofsky, D. L. A. Rall, J. Blaha, and F. L. Culbertson, Spectrographic Observation at Wavelengths near 630 nm of the Interaction between the Atmosphere and the Space Shuttle Exhaust, *Journal of Geophysical Research* 97, 19501-19508, 1992.

11. D. J. Knecht, E. Murad, C. P. Pike, D. L. A. Rall, I. L. Kofsky, T. Zehnpfenning, O. Shepherd, A. T. Stair, Jr., J. B. Elgin, and L. S. Bernstein, Simultaneous

Infrared and Visible Imaging of the Interaction of Space Shuttle Exhaust with the Atmosphere, *Proceedings of the 1994 IRIS Specialty Group on Targets, Backgrounds and Discrimination*, IRIA-IRIS, Vol. II, pp. 147-168, June 1994.

12. D. L. A. Rall, I. L. Kofsky, D. J. Knecht, C. P. Pike, and A. T. Stair, Jr., Infrared Observations of the Bow-Shock 2 Thruster Exhaust with the Atmosphere, *Proceedings of the 1994 IRIS Specialty Group on Targets, Backgrounds and Discrimination*, IRIA-IRIS, Vol. II, pp. 169-190, June 1994.

13. D. J. Knecht, D. L. A. Rall, I. L. Kofsky, C. P. Pike, and E. Murad, Interaction of Solid-Rocket Exhaust Gases with the Atmosphere at 110 Km, accepted for publication in *Journal of Spacecraft and Rockets* 33, 677-685, 1996.

14. D. L. A. Rall, I. L. Kofsky, D. J. Knecht, C. P. Pike, and T. P. Zehnpfenning, Optical Radiations from Interaction of Effluent Gas Interaction with the Low-Orbital Atmosphere, final acceptance for publication in *Journal of Spacecraft and Rockets* 33, 393-403, 1996.

III. Ultraviolet Airglow Radiances Measured by GLO

15. E. Murad, R. A. Viereck, D. J. Knecht, C. P. Pike, J. A. Gardner, A. L. Broadfoot, E. Anderson, and W. Sandel, Thermospheric Metals Observed from Space: Optical Measurements of Mg^+, Ca^+, and Na Viewed in the Limb, Paper SA31A9, *Spring Meeting of the American Geophysical Union*, May 1994.

16. J. A. Gardner, R. A. Viereck, S. T. Lai, D. J. Knecht, C. P. Pike, A. L. Broadfoot, E. R. Anderson, and W. J. O'Neil, Mg^+ and Other Metallic Emissions Observed in the Thermosphere, *Advances in Space Research* 18, 61-64, 1996; also *Society of Photo-Optical Instrumentation Engineers Proceedings* 2266, Optical Spectroscopic Techniques and Instrumentation for Atmospheric and Space Research, ed. Jinxue Wang and Paul B. Hays, pp. 242-252, 1994.

17. J. A. Gardner, R. A. Viereck, E. Murad, D. J. Knecht, C. P. Pike, A. L. Broadfoot, and E. R. Anderson, Simultaneous Observations of Neutral and Ionic Magnesium the Thermosphere, *Geophysical Research Letters* 22, 2119-2122, 1995.

18. J. A. Gardner, R. A. Viereck, E. Murad, D. J. Knecht, C. P. Pike, A. L. Broadfoot, and E. R. Anderson, Limb View Observations of Thermospheric Neutral Na and Mg, Paper SA 57A-02, *Fall Meeting of the American Geophysical Union*, Dec. 1994.

19. J. A. Gardner, R. A. Viereck, E. Murad, D. J. Knecht, C. P. Pike, and A. L. Broadfoot, New Limb View Observations of Thermospheric Emissions at a Terminator Crossing, Paper SA42A-6, *Spring Meeting of the American Geophysical Union*, May 1995.

20. J. A. Gardner, R. A. Viereck, E. Murad, D. J. Knecht, C. P. Pike, and A. L. Broadfoot, Recent Shuttle-Based Measurements of Airglow, Poster GAB11D-18, *XXI General Assembly of the International Union of Geophysics and Geodesy*, July 1995.

21. J. A. Gardner, R. A. Viereck, E. Murad, D. J. Knecht, C. P. Pike, and E. R. Anderson, Simultaneous Observations of Neutral and Ionic Magnesium in the Thermosphere, *Geophysical Research Letters*, 22, 2119-2122, 1995.

22. J. A. Gardner, D. L. A. Rall, I. L. Kofsky, R. A. Viereck, E. Murad, D. J. Knecht, C. P. Pike, A. L. Broadfoot, and E. R. Anderson, Dawn-Dusk Variability in Ultraviolet Atmosphere Limb Background Emissions, *Proceedings of the 1995 Meeting of the IRIS Specialty Group on Targets, Backgrounds and Discrimination*, IRIA-IRIS, in press.

23. D. L. A. Rall, J. A. Gardner, I. L. Kofsky, R. A. Viereck, D. J. Knecht, C. P. Pike, and A. L. Broadfoot, Systematic Measurement of Ultraviolet Dayglow Backgrounds from N_2, prepared for presentation at the January-February 1997 Meeting of the *IRIS Specialty Group on Targets, Backgrounds and Discrimination*.

24. R. A. Viereck, J. A. Gardner, W. J. McNeil, S. T. Lai, E. Murad, and A. L. Broadfoot, Neutral Metallic Species at 150 to 300 Km Altitude: Implications for Vertical Transport of Metallic Cluster Ions, submitted for publication in *Journal of Geophysical Research*, 1996.

IV. Laboratory Investigations (ion-neutral reactions)   Effort suspended 1994.

25. J. A. Gardner, R. A. Dressler, R. H. Salter, and E. Murad, Ion – H_2O Reactions Studied in a Double Mass Spectrometer Coupled with Luminescence Detection, *12th International Mass Spectrometry Conference*, Amsterdam, 26-30 Aug. 1991.

26. R. A. Dressler, J. A. Gardner, R. H. Salter and E. Murad, Luminescence Measurement of Ar^+ + H_2O and N_2^+ + H_2O Suprathermal Charge Transfer Collisions: Product State Distributions from H_2O^+ $\tilde{A}^2A_1$- $\tilde{X}^2B_1$ Analysis, *Journal of Chemical Physics* 96, 1062-1076, 1992.

27. J. A. Gardner, R. A. Dressler, R. H. Salter, and E. Murad, OH $A^2\Sigma^+ \rightarrow X^2\Pi$ Chemiluminescence Measurements of N_2^+, Ar^+ + H_2O Hydrogen Atom Transfer Reactions at Suprathermal Energies, *Journal of Chemical Physics* 97, 2473-2480, 1992.

28. J. A. Gardner, R. A. Dressler, R. H. Salter, and E. Murad, Reactions of N_2H_4 with O^+ and Other Ions at Suprathermal Energies, *Journal of Physical Chemistry* 96, 4210-4217, 1992.

29. J. A. Gardner, R. A. Dressler, and R. A. Salter, Methylhydrazine Reactions with O^+ and Other Ions at Hyperthermal Collision Energies, *Journal of Physical Chemistry* 98, 11630-11636, 1994.

30. Z. J. Jakubek, N. A. Harris, R. W. Field, J. A. Gardner, and E. Murad, Ionization Potentials of CaF and BaF, *Journal of Chemical Physics* 100, 622-627, 1994.

31. S. T. Arnold, R. A. Dressler, M. J. Bastian, J. A. Gardner, and E. Murad, Dynamics of Hyperthermal Kr^+ + H_2O charge-transfer collisions, *Journal of Physical Chemistry* 102, 6110-6120, 1995.

32. [Contribution from consultant S. T. Graul (Asst. Prof. Chemistry, Carnegie-Mellon University; see also Appendix D)]: R. A. Dressler, S. Williams, S. T. Graul, R. H. Salter, and E. Murad, Guided-Ion Beam Measurements of the Kr^+ + NO Charge-Transfer Reaction, *Chemical Physics Letters* 215, 656-661, 1993.

<u>Others</u>

33. R. A. Viereck, S. P. Mende, L. S. Bernstein, E. Murad, G. Swenson, and C. P. Pike, Visible Spectra of PRCS Thruster Plumes, *Proceedings of the 1992 Meeting of the IRIS Specialty Group on Targets, Backgrounds and Discrimination*, IRIA-IRIS, Vol. I, pp.79-90, March 1992.

34. R. A. Viereck, L. S. Bernstein, S. B. Mende, E. Murad, G. R. Swenson, and C. P. Pike, Visible Spectra of Thruster Plumes from the Space Shuttle Primary Reaction Control System, *Journal of Spacecraft and Rockets* 30, 724-730, 1993.

35. A. L. Broadfoot, W. R. Sandel, D. J. Knecht, R. A. Viereck, and E. Murad, Panchromatic Spectrograph with Supporting Monochromatic Imagers, *Applied Optics* 31, 3083-3096, 1992.

36. I. L. Kofsky, N. H. Tran, M. A. Maris, D. L. A. Rall and C. A. Trowbridge, Photometric-Photogrammetric Analysis of Video Images of a Venting of Water from Space Shuttle Discovery, GL-TR-90-0187, 15 June 1990, ADA 202429.

37. I. L. Kofsky, N. H. Tran, M. A. Maris and C. A. Trowbridge, Measurement of Optical Radiations in Spacecraft Environments, GL-TR-89-0168, 15 June 1989, ADA 213814.

38. I. L. Kofsky, J. L. Barrett, J. E. Brownrigg, P. J. McNicholl, N. H. Tran, and C. A. Trowbridge, Excitation and Diagnostics of Optical Contamination in the Spacecraft Environment, AFGL-TR-88-0293, 01 July 1988, ADA 202429.

39. L. Kofsky, D. L. A. Rall, and R. B. Sluder, Measurement and Interpretation of Contaminant Radiations in the Spacecraft Environment, PL-TR-91-2174, 28 June 1991, ADA 241756.

40. G. Lange, E. Weichs, U. Schmidt, and D. Sodeikat, Spectrometer/Radiometer for Measurement of Infrared Signatures from Space, Cryogenic Optical Systems and Instruments IV, *Society of Photo-Optical Instrumentation Engineers Proceedings* 1340, 203-216, 1990.

41. D. A. Levin, L. H. Caveny, D. M. Mann, F. J. Collins, C. Howlett, P. Espy, R.W. Erdman, and E. Zipf, Ultraviolet Emissions from In-flight Plume and Hardbody Flow Fields, *19th JANNAF Exhaust Plume Technology Conference*, May 1991.

42. P. W. Erdman, E. C. Zipf, P. Espy, C. Howlett, R. Loda, R. J. Collins, D. A. Levin, and G. V. Candler, Flight Measurements of Low Velocity Bow Shock Ultra-violet Radiation, Paper AIAA 91-1410, *26th AIAA Thermophysics Conference*, Honolulu, HI, June 1991.

43. J. L. Gole and C. E. Kolb, On the Upper Atmospheric Chemiluminescent Emission Observed upon Release of Aluminum Vapor and Its Compounds, *Journal of Geophysical Research* 86, 9125-9136, 1981.

44. R. R. O'Neil, F. Bien, D. Burt, J. A. Sandock, and A. T. Stair, Jr., Summarized Results of the Artificial Auroral Experiment Precede, *Journal of Geophysical Research* 83, 3773-3780, 1978.

45. J. E. Pickett, G. B. Murphy, W. S. Kurth, C. K. Goertz, and S. D. Shawhan, Effects of Chemical Release by the STS 3 Orbiter on the Ionosphere, *Journal of Geophysical Research* 90, 3487-3497, 1985.

46. B. D. Green, K. W. Holtzclaw, P. B. Joshi, and H. K. Burke, Analysis of Radiances from Orbital Gas Releases, *Journal of Geophysical Research* 97, 12161-12172, 1992.

47. J. B. Elgin, D. C. Cooke, M. F. Tautz, and E. Murad, Modeling of Atmospherically Induced Gas Phase Optical Contamination from Orbiting Spacecraft, *Journal of Geophysical Research* 95, 12197-12208, 1990.

48. R. E. Huffman, *Atmospheric Ultraviolet Remote Sensing*, Chapter 13, Academic Press, San Diego, 1992.

49. R. E. Huffman, the Atmospheric Ultraviolet Radiance Integrated Code (AURIC)–Validation of Version 1.0, *Proceedings of the 1993 Meeting of the IRIS Specialty Group on Targets, Backgrounds and Discrimination*, IRIA-IRIS, Vol. II, pp.123-135, July 1993.

50. R. A. Viereck, E. Murad, C. P. Pike, S. B. Mende, G. R. Swenson, J. B. Elgin, L. S. Bernstein, and S. Lucid, $O(^1S)$ 557.7 nm and $O(^1D)$ 630 nm Emissions in Shuttle Thruster Plumes, *Journal of Geophysical Research* 100, 5819-5825, 1995.

51. R. A. Viereck, E. Murad, D. J. Knecht, C. P. Pike, L. S. Bernstein, J. B. Elgin, and A. L. Broadfoot, The Interaction of the Atmosphere with the Space Shuttle Thruster Plume: The NH (A - X) 336 nm Emission, accepted by *Journal of Geophysical Research*, 101, 5371-5380, 1996.

52. L. S. Bernstein, D. R. Crow, G. N. Freeman, J. W. Cox, and J. B. Lurie, Modeling and Analysis of the Ultraviolet Emissions for the Marquardt R-40 Chamber Measurements, *Proceedings of the 1992 IRIS Specialty Group on Targets, Backgrounds and Discrimination*, IRIA-IRIS, Vol. I, pp. 21-47, March 1992.

53. D. L. Baulch, R. A. Cox, R. F. Hampson, J. A. Kerr, J. Troe, and R. T. Watson, CODATA Task Group on Chemical Kinetics, *Journal of Physical and Chemical Reference Data* 13, 1259-1380, 1984.

54. V. M. Donnelly, D. G. Keil, and F. Kaufman, Fluorescence Lifetime Studies of NO_2. III. Mechanism of Fluorescence Quenching, *Journal of Chemical Physics* 71, 659-673, 1979.

55. S. M. Adler-Golden, The $NO+O$ and $NO+O_3$ Reactions, *Journal of Physical Chemistry* 93, 691-697, 1989.

56. K. H. Becker, W. Groth, and D. Thran, The Mechanism of the Air-Afterglow $NO+O \rightarrow NO_2 + h\nu$, *Chemical Physics Letters* 15, 215-220, 1972.

58. D. E. Paulson, W. F. Sheridan, and R. E. Huffman, Thermal and Recombination Emission of N_2, *Journal of Chemical Physics* 53, 647-658, 1970.

57. J. L. Barrett and I. L. Kofsky, The $NO-NO_2$ System at Laboratory Surfaces, Second Workshop on Spacecraft Glow, *NASA Conference Publication* 2391, 165-168, May 1985.

59. M. E. Jacox, Energy Levels of Polyatomic Transient Molecules, *Journal of Physical Chemistry Reference Data* 19, 1387-1546, 1990.

60. R. A. Viereck, S. B. Mende, E. Murad, C. P. Pike, G. R. Swenson, F. L. Culbertson, and R. C. Springer, Spectral Characteristics of the Shuttle Glow, *Geophysical Research Letters* 17, 1219-1222, 1992.

61. R. A. Viereck, Personal Communication, 1995.

62. G. R. Bradburn and H. V. Lilenfeld, Absolute Emission Rate of the Reaction between Nitric Oxide and Atomic Oxygen, *Journal of Physical Chemistry* 92, 5266-5270, 1988.

63. D. G. Keil, V. M. Donnelly and F. Kaufman, Fluorescence Lifetime Studies of NO_2. IV. Temperature Dependence of Fluorescence Spectra and Collisional Quenching of Fluorescence, *Journal of Chemical Physics* 73, 1514-1520, 1980.

64. R. A. Hartunian, W. P. Thompson, and E. W. Hewitt, Glow Discharge Shock Tube for Studying Chemiluminescent, Surface-Catalytic, and Gas Phase Reaction Rates: Temperature Dependence of NO-O and CO-O Chemiluminescence, *Journal of Chemical Physics* 44, 1765-1769, 1966.

65. R. R. Meier, Ultraviolet Spectroscopy and Remote Sensing of the Upper Atmosphere, *Space Science Reviews* 58, 1-185, 1991.

66. R. R. Meier and D. E. Anderson, Jr., Determination of Atmospheric Composition and Temperature from the UV Dayglow, *Planetary and Space Science* 31, 967-981, 1983.

67. R. R. Meier and J. M. Picone, Retrieval of Absolute Thermospheric Concentrations from the Far UV Dayglow: An Application of Discrete Inverse Theory, *Journal of Geophysical Research* 95, 6307-6320, 1994.

68. S. A. Budzien, P. D. Feldman, and R. R. Conway, Observations of the Far Ultraviolet Airglow by the Ultraviolet Limb Imaging Experiment on STS-39, *Journal of Geophysical Research* 99, 23275-23287, 1994.

69. H. Rishbeth and O. K. Garriott, *Introduction to Ionosphere Physics*, Chapter III, Academic Press, New York, 1965.

70. L. S. Bernstein, J. B. Elgin, C. P. Pike, D. J. Knecht, E. Murad, T. Zehnpfennig, G. E. Galica, and A. T. Stair, Jr., Sources of the Infrared Radiation Generated by the Interaction of Fast $O(^3P)$ with H_2O in Space, *Journal of Geophysical Research* 101, 383-393, 1996.

71. D. G. Koch, G. B. Fazio, W. Hoffman, G. Melnick, G. Rieke, J. Simpson, F. Witteborn, and E. Young, Infrared Observations of Contaminants from Shuttle Flight 51-F, *Advances in Space Research* 7, 211-223, 1987.

72. R. E. Meyerott, G. R. Swenson, E. L. Schweitzer, and D. G. Koch, Excitation of Low Lying Vibrational Levels of H_2O by $O(^3P)$ as Measured on Spacelab 2, *Journal of Geophysical Research* 99, 17559-17575, 1994.

73. D. K. Zhou, W. R. Pendleton, Jr., G. E. Brigham, A. J. Steed, and D. A. Dean, Infrared Spectral Measurements (400-2500 cm^{-1}) of Shuttle-induced Optical Contamination, *Geophysical Research Letters* 21, 613-616, 1994.

74. B. L. Upschulte, D. B. Oakes, and G. E. Caledonia, Optical Excitation of Gases in Fast Oxygen Atom Collisions, *Proceedings of the 1993 Meeting of the IRIS Specialty Group on Targets, Backgrounds and Discrimination*, IRIA-IRIS, Vol. I, pp. 317-344, March 1991.

75. R. J. Niciejewski and J. H. Yee, Airglow Rotational Temperature Measurements During the ALOHA Campaign, *Geophysics Research Letters* 18, 1353-1356, 1991.

76. W. Pendleton, Jr., P. Espy, D. Baker, A. Steed, M. Fetrow, and K. Henricksen, Observation of OH Meinel (7,4) P N" = 13) Transitions in the Night Airglow, *Journal of Geophysical Research* 94, 505-510, 1989.

77. P. J. Espy, R. Huppi, and A. Manson, Large-scale, Persistent Latitude Structures in the Mesospheric Temperature during ANLC-93, *Geophysical Research Letters* 22, 2801-2804, 1995.

78. R. A. Dressler, R. H. Salter, and E. Murad, Guided Ion-beam Measurements of the $X^+ + H_2O$ $(D_2O)(X=Ar, N_2)$ Collision Systems, *Journal of Chemical Physics* 99, 1159-1171, 1993.

79. S. G. Lias, J. E. Bartmess, J. F. Liebman, J. L. Holmes, R. D. Levin, and W. G. Mallard, Gas-Phase Ion and Neutral Thermochemistry, *Journal of Physical and Chemical Reference Data* 17 (Suppl. 1), 1-872, 1988.

APPENDIX A

Optical properties of water released in low earth orbit

James A. Gardner II, David L. A. Rall, Christian A. Trowbridge, Irving L. Kofsky
PhotoMetrics, Inc., Woburn, Massachusetts 01801

Rodney A. Viereck, Edmond Murad, Charles P. Pike
USAF Phillips Laboratory, Hanscom AFB, Massachusetts 01731

A. T. Stair, Jr.
A. T. Stair Associates, Bedford, Massachusetts 01730

Alireza Setayesh
Radex, Inc., Bedford, Massachusetts 01730

ABSTRACT

Analysis of intensified video photographs of a twilight venting of excess water from space shuttle showed that the -1 mm diameter stream cavitationally fragments within about 1 m, forming two discrete-particle components and vapor. The images from nearby cameras are dominated by irregular, polydisperse water/ice droplets with sizes comparable with the venting orifice and outward velocity indistinguishable from that of the initially coherent liquid. In contrast the 2½ km-long quasiconical trail imaged from a distant ground station consists of accompanying submicron ice spherules that were produced by partial recondensation of the overexpanded vacuum-evaporated water gas, which are sublimating at rates that we calculated from the measured falloff of axial sunlight-scatter radiance and the energy balance of progressively roughening ice at 329 km altitude; at low latitudes they cool to 180K in <1 s, and their radii transition to the Rayleigh-scattering range in -1 min. The very much larger fragmentation particles come to a slightly higher equilibrium temperature within ~2 min, and persist for a few earth orbits. These three components of the vented water (and other high vapor pressure liquids) radiate and scatter earthshine and solar photons, and the orbital-velocity molecules are also excited by collisions with the residual atmospheric gas, overlaying wide-angle contaminating foregrounds on remote optical sensing from onboard. The particle sizes, densities, and temperatures derived from the visible data are applied in estimating ultraviolet and infrared radiances of the ice/vapor-containing volumes near Shuttle Orbiter.

1. INTRODUCTION

Scattering of visible sunlight from the clouds of droplets formed by liquid water vented from space shuttle *Discovery*[1-4] is a primary source of information about the foregrounds that result from releases of this and other high vapor pressure liquids into the orbital environment. The phenomenology data in intensified video photographs from onboard the spacecraft and the near-nadir Air Force Maui Optical Site (AMOS) provide a basis for quantifying both this optical contamination at other wavelengths and estimating the physical contamination produced by the "flash"-evaporated/sublimed water molecules. Vibrational and rotational emissions from this high-velocity vapor are excited by its collisions with the ambient atmosphere as well as by its thermal and photo-excitation. We calculate here the resulting infrared brightness distributions with the help of a recently developed gas-transport/excitation model[5].

Liquid water rapidly exposed to vacuum has long been known to be unstable against cavitationally bursting[6-10] due to the violent growth of bubbles of vapor ("steam") and dissolved gases within the then-superheated volume. About one-sixth of the injected mass evaporates[11] in cooling the initially 300K stream and its fragmentation droplets to an equilibrium temperature at sunlit orbital altitudes that we have derived as described here. The *Discovery* images also allowed us to bound the fraction of this evolved vapor from a routine operational venting that recondenses as it expands across the gas-solid equilibrium line of the phase diagram of water substance, and to determine the dependence on their distance from Orbiter of the diameters of both these Rayleigh-Mie size droplets and the "geometric"-scattering, polydisperse stream-rupture particles[1-4]. These particles show no evidence of returning to the spacecraft.

Sections 2 and 3 summarize this recent shuttle experiment to provide a background for predictions of the UV-visible-infrared foregrounds and the flow of gaseous water to spacecraft surfaces, which are presented in Sections 5 and 6.

2. EXPERIMENTAL

Largely pure and dissolved gas-free fuel cell product ("supply"[12]) water was forced under pressure directly into *Discovery's* wake on orbit 49 of shuttle mission STS-29 (16 Mar 89), at 19.4 g/s through an electrically-warmed, 0.14-cm opening truncated-conical nozzle. The experiment was planned by the Air Force Geophysics (now Phillips) Laboratory to take place when the flight altitudes were directly illuminated by the sun while the lower atmosphere above the ground station lay in the hard earth's shadow. The spacecraft was moving east-northeast in a 329-km circular orbit as it passed almost directly over AMOS (21°N - 204°E, 3.0 km altitude) about 1 hr before local dawn. Its zenith angle and range, the aspect angle to the retrograde trail (which determines the optical path length through it), and the solar-scatter angle (between vectors from the sun to *Discovery* and from *Discovery* to the groundbased tracking camera) are shown in Fig. 1.

This imaging telescope had an Intensified Silicon Intensifier Target (ISIT) photocathode with S-20R spectral sensitivity (its nominal FWHM photon response, taking into account the small prefiltering by the typically clear atmosphere above the mountaintop observatory, is 0.39-0.65 μm), a 55-cm diameter objective lens providing a 0.5°-diagonal field of view, and electronic gain under operator control. Onboard *Discovery*, SIT zoom cameras of space shuttle's closed-circuit video system viewed from near the tail in its open payload bay and, handheld by a mission specialist, through a crew cabin window about 5 m above and forward of the water-venting orifice (refer to the insert in Fig. 5). These cameras have similar spectral response, and automatic gain control. Figure 2 shows typical images of the cloud of sunlit particles from these close-lying and remotely-located stations.

The AMOS photographs represent a series of view projections and "scene lightings" of a time-stationary physical phenomenon, as both the venting and geophysical conditions remain sensibly constant over the segment of trajectory within the camera's field of regard. Since the optical signal from particles whose dimensions are at least comparable with the light wavelength improves at near-forward scattering angles and from elongated sight paths, we selected for detailed photometric-photogrammetric analysis a video image when *Discovery* was in the northeast quadrant at 60° zenith angle (Fig. 2a). Its high-albedo body is the strongly bloomed feature at the head of the smooth-surfaced, ~2½ km-long quasiconical trail. Figure 3 plots the relative radiant intensities per unit distance from the orifice (corrected for aspect angle), i.e., the brightnesses summed along lines perpendicular to the trail's symmetry axis or--in the parlance of rocket exhaust phenomenology--the "station radiance". (This transverse summation removes the effect of the optically-thin particle stream's divergence.) A linear dependence of output current-above-baseline on incident irradiance, which is characteristic of electron multiplier-based image intensifiers operated well below saturation, has been assumed.

The backlit images from the two onboard cameras in contrast showed primarily densely packed discrete particles, which both flickered as they moved coherently outward (indicating tumbling of irregular shapes) and produced variable image irradiances from fixed ranges (evidencing a spread of sizes). Both of these effects have been seen in laboratory tank simulations[10], which indicated that an outer ice "shell" quickly formed on the fragmentation droplets cracks and occasionally even breaks off under the increased pressure from their less-dense, still-unfrozen interior water. This beam of particles, whose dimensions are of the order of the venting nozzle diameter[4,6,8,10], diverges at sensibly the same angle as the trail seen from AMOS (~2/5 radian; see Fig. 2) and projects back to an apex roughly ½ m out from the orifice.

We determined their longitudinal velocities by following several readily-identifiable--and therefore presumably particularly large--water/ice droplets in successive video frames. The 23 m/s velocity with ±35% systematic uncertainty measured is experimentally indistinguishable from the velocity relative to the moving spacecraft of the still-intact (and in fact somewhat contracted[4,6]) liquid stream beyond the conical venting nozzle. The low mean transverse speed obvious from the small angular divergence, along with the narrow spread of the individually-measured longitudinal speeds, shows that breakup of the liquid imparts little momentum to the resulting discrete particles, and indeed the translational energy per unit mass delivered in this fragmentation is extremely small compared with their later changes in heat content.

The transverse-summed radiances in the AMOS frame analyzed are compared in Fig. 3 with predictions of a straightforward model of the submicron droplets' energy balance described in the next Section. The close fit, and also the weak dependence on scatter angle as *Discovery* moves toward the rising sun, shows that this signal at the distant optical station is due to these small ice spherules rather than to the much larger direct products of stream rupture. In the photographs from *Discovery* these unresolved smaller particles appear as a "haze" underlying the bloomed images of the fragmentation particles. Similar heat-balance calculations[1,4] showed that evaporation/sublimation from these very much

larger drops would result in only a $<-15\%$ decrease in their mean cross-sections for scattering visible photons in the ~2-min period during which they traverse the length of trail detectable in the AMOS photographs. In contrast the measured total decrease in radiant intensity per unit length (at distances from *Discovery* beyond where video blooming from its body contaminates the data) can be seen in Fig. 3 to be as much as a factor of 50.

3. INTERPRETATION

As mentioned above, the smaller ice particles are formed by "inverse sublimation" of some fraction of the evolved water vapor. (Rayleigh scattering of sunlight from this gaseous component of the flowfield is far below the radiance thresholds of all the video cameras.) Since the circumference of these recondensation droplets is of the order of twice the wavelength, their cross-sections for scattering visible light per unit mass of water substance are near the maximum physically attainable. Furthermore, their rate of scattering per unit solid angle changes more slowly with direction from the sun than that of the larger ice/water particles (which produce a much stronger forward peak), in agreement with the observed quite small variation of aspect- and downstream distance-normalized station radiance in the sequence of AMOS video images of which Fig. 2a is an example [for scattering at 48°]. The dependence of transverse-summed radiance on distance X from Orbiter is the basis for a calculation of the radius and temperature history of these small droplets. Additionally, the relative irradiances at the onboard image planes from this cloud of unresolved particles and from the distinguishable large particles lead to an estimate of the fraction of the vented-evaporated water that recondenses.

The energy balance of spherical ice (or liquid water not undergoing a phase change) with radius r and uniform temperature T is expressed as [4,8,13-15]

$$(4\pi/3)r^3\rho C\ dT/dt - 4\pi r^2 L dr/dt = \bar{\epsilon}_e\Omega_e r^2 \sigma T_e^4 + \bar{\epsilon}_s\Omega_s r^2 \sigma T_s^4 - \bar{\epsilon}_p 4\pi r^2 \sigma T^4,$$

where the subscripts e, s, and p refer to the thermally radiating earth-and-atmosphere, the sun, and the particle. The terms on the left side are rates of heat loss by cooling and sublimation (or evaporation), and those on the right represent heat gain by absorption of earthshine and sunlight photons and loss by thermal emission. (Heating of the particles by aerodynamic collisions can be readily shown to be negligible at *Discovery's* altitude, and the effect of the additional energy input from sunlight scattered off the atmosphere is very small.) $\bar{\epsilon}$'s are emissivities/absorptivities of the droplet weighted over the Planck emission spectra of the two assumed-blackbody sources of illumination, and of the gray body itself at T; Ω's are the solid angles subtended by the solar disk and curved earth-and-atmosphere (1.4π ster at 329 km); ρ, C, and L are the density, specific heat, and heat of vaporization of ice (or water); and σ is the Stefan-Boltzmann constant. A second relationship between the two unknowns follows from the sublimation (or evaporation) rate when the probability that departing gas molecules recondense is small, as appears to have been experimentally validated for the coherent column[9]:

$$-dr/dt = 0.27\ P(T)/T^{\frac{1}{2}} = 0.27\ T^{-\frac{1}{2}}\ (2.4\times 10^{10}\ \exp -6110/T),$$

where the numerical value of the multiplier refers to r in cm and vapor pressure P of solid or liquid water in torr. We converted X to time-after-droplet formation t by applying the measured (constant) longitudinal velocity of the distinguishable large droplets, which is justified by the similar angular spreads in the images of the two components of the cloud and the absence of mechanisms that would impart longitudinal momentum to the recombination droplets.

We initially solved these two simultaneous rate equations (numerically) with the assumption that the wavelength-averaged emissivities are proportional to r, a standard result of Mie theory applied to submicron spheres. This dependence ("volume scattering") led to r decreasing at much lower fractional rates than we derived from the AMOS radiances, a discrepancy that is not removed by changing the earthshine temperature--we adopted 280K, representing the average over the nadir hemisphere at low latitudes--, or assigning a different velocity to the recondensation droplets, or assuming polydisperse distributions of their initial radius r_0. The increasing downward curvature of the log-radiances in Fig. 3 is in the direction expected from progressive roughening of the surface of ice exposed to vacuum in the laboratory[13], which has the effect of increasing the imaginary component of its index of refraction and therewith slowing the decrease of its temperature and sublimation rate. An empirical fit to these AMOS data is achieved[3,4] by increasing the $\bar{\epsilon}$'s by a term proportional to the square root of $(r_0 - r)$, a dependence that may arise from the "statistical" nature of the irregular particle erosion (a linear dependence on the decrease in radius gave worse fits to the data). The derived radius and temperature of these small ice particles when they are above threshold in the AMOS images are in Fig. 4.

This dominance of the radiances projected to distant observers by these unresolved small particles and the magnitude and density of the distinguishable irradiance patches from individual large particles in the images from nearby lead to a rough joint constraint on the mean radius of the fragmentation drops and the fraction of vented water that recondenses. Table 1 summarizes the *Discovery* trail parameters estimated from this procedure[4], including an absolute visible brightness. Approximately 2% of the water released, or one-eighth of that which evaporates in the process of freezing and further cooling the remaining mass, forms into droplets whose initial radius r_0 is 0.3 μm. Laboratory-tank measurements with ~100 μs-pulsed narrow water streams indicated a roughly similar recondensation fraction with comparable radii of these ice particles[8], which furthermore were within experimental error monodisperse--as we have been assuming.

The constraint showed the mean radius of the fragmentation-product droplets to be 0.13 $\pm$ 0.02 cm, which considering their previously observed[10] irregular ("bowl" and "dish") shapes and broad overall-size distribution should be viewed as an ill-defined average figure. Application of the above energy balance equations led to the results that this radius decreases by <5% over a 2½ km initial flight path and that these discrete particles survive for several hr[4]. In the first ~1 s diffusion of heat from their interior controls the temperature at their immediate surface, an effect that we took into account both in Fig. 4 and in calculating the rates of water vapor evolution shown in Fig. 5. These radial temperature (and also phase) gradients and--in particular--their shape/size irregularities introduce uncertainty into calculations of the thermal emission from the large drops when they are < ~ 20 m from Orbiter, and their departure from sphericity remains a potential source of error in the infrared radiances after they become isothermal.

4. PHENOMENOLOGY, SCALING

The numerical values presented here refer to relatively pure ~30°C water released near 330 km altitude at low latitudes (or midlatitudes in summer) with the velocity and orifice diameter stated. (The equilibrium particle temperatures have a small dependence on the nadir angle-weighted earth-and-atmosphere radiation model adopted[16].) Since atmospheric drag is negligible over the time scales considered, these results would be independent of the direction in which the stream is released. Larger-diameter, higher-temperature, lower-velocity, more contaminated and gas-laden water columns burst nearer the venting nozzle[6,9], and impurities and lower initial temperatures lead to smaller fragmentation-cone angles (human waste water dumped from shuttle has been observed to form a narrower particle trail than supply water, by a camera held outboard on the spacecraft's Remote Manipulator Arm). Alteration of the equation of state and surface tension of the injected substance by dissolved materials can be expected to lead to quantitative differences in the number and initial size of the two droplet components, and high concentrations of "dye" dopants could increase the absorptivities/emissivities and so change the sublimation rates[7] (although the large water-ice drops are already optically thick across virtually all of the infrared). We note also that low vapor pressure liquids that contain little dissolved gas may not explosively rupture due to boiling, but remain subject to breakup into droplets initiated by fluid stream instabilities[6].

These comments are of necessity qualitative, and in view of the incomplete information about the response of nonreactive liquids to the near-vacuum and radiation field of low earth orbit we have suggested further space and laboratory experiments[7]. The liquid-solid-vapor phenomenology for a given initial temperature, diameter, and flow rate in general depends nonlinearly on the macroscopic parameters vapor pressure, specific heats and heats of fusion and evaporation, thermal conductivity, expansion coefficient, surface tension, and viscosity, as well as on the molecular weight and elastic collision cross-sections of the vaporized material. In consequence scaling of experiment data from one even chemically pure and dissolved gas-free liquid to another is likely to be highly unreliable. Even considering only water, further experience is needed to extrapolate reliably the numerical quantities from this experiment to other venting conditions; the optical sensing-contaminating radiances derived in Section 6 should be viewed in this context.

5. PHYSICAL CONTAMINATION OF ORBITER

The video images from onboard show no evidence of stream-fragmentation droplets drifting backward in the frame of reference of *Discovery* to recontact its body: all move away with sensibly the same speed, that of the radially-relaxed liquid column. (These cameras detected no slower-moving discrete particles, such as have been proposed as originating from fracturing of frost formed on the spacecraft wall near the venting nozzle.) Detailed orbital trajectory calculations[17] have shown that 1-mm ice particles would not collide with Shuttle Orbiter on its subsequent passes, at all angles relative to its flight path that the liquid stream may be injected. Since the much shorter-lived recondensation droplets have the same outward velocity, they also do not return to physically contaminate the spacecraft.

As mentioned, the intensified-video photographs do not detect the unrecondensed water, nor does scattering of sunlight from the droplets provide information--other than an estimated stream-breakup distance--about the rates at which this gas is evolved. (The "flash" vaporization that follows from the exponential dependence of equilibrium vapor pressure on surface temperature is a far more important source of contamination than the indirectly-observable much slower sublimation from recondensation particles, as will become apparent shortly.) Since the vapor comes off with much greater thermal speeds in the spacecraft's reference frame than the directed outward velocity of the stream (of order 600 m/s[9], and to a good approximation isotropic) some fraction of it recontacts exposed vehicle surfaces. Furthermore, these return fluxes are increased and their angular distributions broadened by scattering of water gas from the atmosphere[5,18,19].

An estimate of the vapor production rates from current theory[6] and laboratory vacuum tank measurements[9] on ~1 mm diameter, 300K water streams appears in Fig. 5. The calculation considers only conductive rather than convective internal heat transport (except as the somewhat supercooled liquid explodes at $X = \frac{1}{2}$ m, where the resulting droplets are taken as becoming isothermal at its radially-averaged temperature) and also neglects heating by redeposition of vapor, which appears to be justified by the experiment data. Despite the approximations in the existing theory for cylindrical[6] or spherical liquid geometry, and the uncertainty in the (assumed uniform) water temperature upon injection and breakup distance, the predicted gas-evolution rate summed along X is satisfactorily close to the aforementioned thermodynamic value of one-sixth. We are currently developing a Navier-Stokes equations-based numerical model[7] of the coupling between the two phases that will provide an improved spatial distribution of the vapor escape rates.

This vaporization/sublimation profile, with the further (good) approximation of isotropic free-molecular flow and consideration of the finite diameter of the diverging gas source, allows straightforward calculation of the direct fluxes to exposed surfaces of Orbiter and its instrumentation. For example onto its port-side wall 1 m from the orifice these fluxes are of order 10^{17} molecules/cm^{2}s, or 10^2 monolayers in each second of routine water venting. With its payload bay doors closed the spacecraft's body intercepts roughly half of all the vapor initially directed into its starboard hemisphere, producing an extended gas penumbra; and (as the elevation diagram in Fig. 5 shows) the open port-side door shields instrumentation inside the bay from direct exposure to the close-in stream region where most of the gas molecules originate. The evolution rates also serve as input to theoretical calculations[5,19,20] of the contamination by molecules backscattered from the ambient atmosphere and one another (and at least in principle, from control rocket exhaust and outgas species), and--in particular--of the resulting infrared radiance distributions. Direct simulation Monte Carlo calculations of the concentrations of and impact-excited radiances from water molecules exhausted from space shuttle's control engines (at ~½ its orbital speed) indicate that the molecule densities in its bay are strongly dependent on the angle between outflow axis and trajectory even at 600 km altitude[5]; another rarefied gas dynamics model[19] shows substantial buildup of density off ram surfaces at the spacecraft's lowest operating altitudes. A planned extension of Phillips Laboratory's "SOCRATES"[5] Monte Carlo approach to apply innermost computational-mesh spacings comparable with the dimensions of Orbiter will provide quantitative information about the flow of reflected water molecules to its payloads.

6. UV AND IR FOREGROUNDS

Table 2 is a brief qualitative overview of the optical radiations from the three components of the water trail at wavelengths outside the visible range of these *Discovery* video data. The thermal emissions and scattering of earthshine and solar photons from the particles are localized in the image regions shown in Fig. 2, while the collisionally-excited infrared emissions from the vapor originate from all directions around the spacecraft (as is illustrated in Fig. 7).

6.1. Particle stream

Calculation of brightness distributions from the array of discrete liquid/solid particles in effect reduces to exercises in applying standard electromagnetic wave-interaction and -generation theory to dielectric droplets with the radii, temperatures, and spatial densities derived above. The primary sources of error in the computed foregrounds would be the departure from sphericity of both types of particle and uncertainties in the optical constants of ice at their low temperatures[16,21]. Since the diverging trail is optically thin at all wavelengths (as can be readily shown), its radiances in general vary with (X sin [aspect angle])$^{-1}$, the product of sight path length through and mean density within it. Scans transverse to the longitudinal direction in the AMOS video images[4] indicated that the approximation of constant particle concentration at each downstream distance X within the 2/5-radian fragmentation quasicone should be applied in estimating infrared and ultraviolet brightnesses in sensor projections that intercept the trail away from its long axis.

In the ultraviolet, intensities of radiation from the fragmentation particles (which are "geometric" scatterers) fall off with decreasing wavelength due to the decrease in spectral irradiance of sunlight. In contrast radiation from the recondensation particles would show a complex dependence on wavelength and X--that is to say, r--for size parameters $(2\pi r)/(wavelength) > -2$, where Rayleigh and "Mie" scattering give way to essentially geometric cross-sections. Indeed, at some wavelength/X ratios and photon scattering angles the UV brightnesses of the trail can exceed its measured mean over the visible range (see Table 1). A sunlit water venting has recently been photographed in the vacuum ultraviolet, from the bay of space shuttle on mission STS-39[22]; the images appear similar to Fig's. 2b and 2c, as would be expected for r_o = 0.3 μm near the spacecraft.

In the infrared, the -mm particles are optically thick while these ≤ 0.3 μm ice particles are inefficient scatterers-radiators except near 2.7 μm[16]. The large-droplet component thus dominates the radiances even in projections to distant sensors, suppressing the severe spectral structure characteristic of the small droplets. That is, through virtually all of the IR thermal emission from the fragmentation particles exceeds solar and earthshine photon scattering by the recondensation particles, the opposite of the situation in the visible. Table 2 presents estimates of the radiances viewing normal to the trail centerline at large and small X in long- and short-wavelength infrared bands applicable in surveillance, made from the Planck radiation from the fractional area covered by the dilute array of blackbody spheres at the temperatures derived in Fig. 4 with a correction in the 3-5 μm interval for scattering of sunlight (which despite the very low droplet reflectivities would be comparable with their thermal emission at low T). In view of the uncertainties from the actual particle shapes, sizes, and densities within sight paths, and the potential error from assuming isothermality at X < -20 m (where the large droplets may be optically thin at some wavelengths over outer radial shells with significant temperature gradients), we have stated only the order of magnitude of these spectrally-continuous infrared brightnesses "looking in" perpendicular to the quasiconical particulate trail. Looking out from Orbiter into the relatively small solid angle that it occupies, the foregrounds would obviously be greater--very much so in some projections--because of the smaller view aspect angles.

As the temperatures of the droplets become less than the effective radiating temperature of the earth-and-atmosphere, the vented water volume--like most meteorological clouds--would exhibit "negative [infrared] contrast" in nadir-directed views. This effect is small since the emissivities in columns normal to its long axis are only $10^{-6} - 10^{-3}$ between X = 1 km and 1 m. Nonetheless even at 2 km from the venting orifice the radiances at the IR "window" wavelengths considered in Table 2 exceed those from the atmosphere's limb at orbital tangent altitudes[23] by at least an order of magnitude. At ~10 m intercept distances of fields of onboard sensors, these foregrounds from the more concentrated particles cloud would interfere with Shuttle Orbiter-based radiometry of the limb at tangent altitudes as low as 30-40 km.

6.2. Water vapor

The major fraction of the gas evolved expands near-isotropically into the atmosphere from a source whose dimensions are comparable with those of Shuttle Orbiter (the aforementioned back-side penumbra being partly filled in by scattering). A straightforward calculation shows that the column densities of water molecules become high enough to perturb the ambient airflow only within a few m of the venting orifice, which is much less than the size of the spatial cells typically used in numerically computing[5,18] volume rates of scattering and radiation near spacecraft. In consequence the body of thought on excitation of outgassed water[18,19,24-28], considered to come off after ~1 day in orbit at roughly one-hundredth the rate at which molecules evaporate/sublime from operational water dumps (as well as on the flowfield of the more energetic rocket-exhaust species[5]), can be brought to bear in predicting the contaminating scene brightnesses. As infrared radiations from this outgas have already been found to interfere with space shuttle-based astrophysical spectroradiometry[24,26], IR foregrounds from the gas evolved from vented water should be readily observable.

These emissions arise primarily from impact excitation of rotational and low-lying vibrational states of neutral and ionized (by charge exchange) H_2O molecules, and formation of OH (hydroxyl) radicals. Resonant and fluorescent scattering of earthshine and sunlight by the vapor, and its thermal excitation[25,28] as it leaves the about-260K condensed stream (Fig. 5), are further sources of optical foreground; see Fig. 6. At the 2½ – 3½ eV center-of-mass translational energies available in collisions with ambient air single-mode, multimode (for example 011 and 110), and multiquantum (020) vibrational levels of H_2O are accessible[26]--these are also populated by the radiation field--, and the fourth vibrational state of OH can be reached in excitative reactions of H_2O with the atmosphere's relatively abundant oxygen atoms. Thus combination-band and overtone photons as well as the familiar single-quantum radiations are expected, principally from within an elastic-collision mean free path from the spacecraft. The IR spectrum includes, in rough order of intensity

-- the commonly-encountered strong stretch- and bending-mode fundamental sequences of H_2O near 2.7 and 6.3 μm, rotationally broadened (to an extent that is not known, and would be best determined by on-orbit spectroscopy of evolved water vapor);

-- the fundamental vibrational cascade of OH extending above 2.8 μm, also similarly broadened (and whose excitation cross-sections at orbital impact velocity also lend themselves to measurement in space experiments);

--spectrally widespread rotational lines of neutral and singly-ionized water molecules, in which about equal radiances are expected in the 5-16, 17-22, and 23-28 μm wavelength regions[18];

-- stretch- and bending-mode fundamental bands of H_2O^+ near 3 and 7 μm, from the high cross-section[29,30] charge-exchange reactions with ionospheric O^+;

--the OH first-overtone sequence centered at 1.6 μm (the second and third overtone are much weaker);

-- intercombination and mode-transfer bands from the two water species, primarily near 1.9, 3.1, and 4.7 μm.

(The electronic bands in the ultraviolet and visible, and as mentioned Rayleigh scattering, are extremely weak.)

Each water molecule is photo-excited about once per 1000 s in the 6.3 μm transition (010-000, mostly by earthshine) and once per 4000 s in the 2.7 μm stretch modes[27] (001 and 100-000, by sunlight). In addition 1½ × 10^{-4} of the molecules evolve from the liquid stream and fragmentation droplets in the 1/20 s-lifetime 010 state, from which they radiate over a -30 m (exponential) path; and a much larger fraction comes off in much longer-lived rotational states, from which arise comparable total "look-out" radiances[28] in long-wavelength infrared photons. At the air densities where space shuttle normally operates excitation by collisions as noted proceeds more rapidly, resulting in predicted radiance distributions (in "look-in" projections, to emphasize the radial and angular dependences of the contaminating emissions) such as are illustrated in Fig's. 6 and 7. These were calculated by the aforementioned direct-simulation Monte Carlo method[5]. We adopted the cross-sections for elastic scattering and impact excitations previously applied[5,18], and neglected both cascade population of upper vibrational states of H_2O (which are thought to increase its emission rates by -60%[26]) and rotational lines from H_2O^+ (a smaller additional effect). In view of the well-known large uncertainty in the cross-sections for excitation--and even for elastic processes--, omission of thermal and photo-excitation, and the approximation of an isotropic vapor source (both shielding of the flow by Orbiter's body and the low-level continuing input of molecules sublimated from both size particles at X's beyond the innermost cell of the computational grid are inadequately considered), these predictions of the infrared brightnesses should be considered as less than fully reliable.

Figure 6 is a simple scaling-up to the unrecondensed vapor evolution rate (further reduced by one-quarter as a first-order simulation of the "loss" due to Orbiter's body) of previously calculated[18] dependences on distance from the spacecraft of impact-excited radiances in three wavelength regions. These had been compiled for 0.01 g/s of water outgassing uniformly in angle around the spacecraft. As they refer to incident air at 75% higher density and 15% lower relative velocity than for *Discovery's* venting conditions, the plots are intended to be only semiquantitative representations of views normal to the ram, wake, and perpendicular-to-trajectory directions. The corresponding foreground radiances presented to sensors looking out from onboard are to a reasonable approximation one-half these look-in values extrapolated to X = 0, with the following principal caveats. 1) Numerical errors are introduced by the finite resolution of the grid near the "point" source of water vapor, which lies in the same cell as the spacecraft and the sensors themselves; 2) the calculated radiances viewing antiparallel to the initial stream direction are upper limits, as the transport model does not take into account blocking of the initial retrograde-to-stream gas flow by Orbiter's body; and 3) the radiances when the vapor source is within or even near instrument fields of view--obviously, poor experiment practice--are likely to be substantially underestimated because the densities are higher there than implicitly adopted in scaling the outgas results.

The brightness profile shapes are broadly similar for emission features other than these summed rotational lines and the two overlying principal short wavelength infrared bands, which with the cross-sections applied have about equal excitation probabilities[5,18]. A further caveat 4) is that the brightnesses near 6.3 μm looking out into the hemisphere into which the water is vented are about twice those predicted from collisional impact at 329 km altitude due to emission within about -30 m from their evolution point by H_2O molecules that evaporate from the stream or droplets in the 010 state. As this last radiation tends to originate within the hyperfocal distance of optical sensors with very narrow fields of view, its degrading effect on their performance is somewhat ameliorated[25]. These adapted results and those in Fig. 7 indicate that the contaminating optical foreground from flash-evaporated water is reasonably isotropic (away from a region extending in both directions through the vented stream, which obviously presents computational difficulties), and lend themselves to comparison with the estimates in Table 2 of the spectrally-continuous radiances viewing into the limited solid angle occupied by the cloud of liquid/solidified water particles.

Figure 7 is a plot of look-in brightnesses in the (1,0) vibrational band of electronic ground-state hydroxyl, whose Q branch is at 2.80 μm and whose rotational width when produced by atom exchange is not known (¼ eV is a plausible estimate). The calculations refer to *Discovery's* venting and the other input parameters stated above, except that the populations of the first vibrational level of OH have been multiplied by two as a first approximation to taking into account cascading following the analogous population of higher levels. The essentially-spherical symmetry of the inner (higher) contours shows that this infrared foreground would be almost uniform in elevation and azimuth viewing from the spacecraft away from the above-noted zone in which the numerical method is unreliable, with a magnitude that we calculate to be 1×10^{-9} W/cm^2 sr. (This figure is in satisfactory agreement with the plot of SWIR radiances in Fig. 6, in which the H$_2$O stretch bands are also included but cascade of OH[†] is neglected.) The asymmetry of the more distant contours about the trajectory direction is an artifact of limited numerical precision of the calculation. Their distinct "drag" toward the wake shows that after water dumps end at this altitude the 7¾ km/s-velocity spacecraft outruns the gaseous radiation source within $\lesssim 1$ s; emission from the exhaust gases of Orbiter's thruster rocket engines shows a similar effect[30]. However water molecules that had adsorbed on surfaces could lead to longer-persisting optical foregrounds as they offgas at later times.

About equal collisionally-excited radiances are predicted in the sum of the two water bands near 2.7 μm and the 6.3 μm band, and also in the aforementioned arrays of pure-rotational lines[18]. An order of magnitude less total energy[26] would be emitted in each of the final three vibrational features listed above. In comparison under *Discovery*-like venting conditions optical sensors in the payload bay whose fields intercept the particulate trail proper at (typical) X = 20 m would encounter essentially spectrally-continuous contaminating daytime foregrounds of about 10^{-9} W/cm^2 sr between 2½ and 3½ μm--with which the almost completely surrounding, spectrally-structured radiance from the evolved vapor is comparable--, and 10^{-7} W/cm^2 sr between 8 and 13 μm--very much higher than in other pointing directions.

7. ACKNOWLEDGMENTS

8. REFERENCES

1. C. P. Pike, D. J. Knecht, R. A. Viereck, E. Murad, I. L. Kofsky, M. A. Maris, N. H. Tran, G. Ashley, L. Twist, M. E. Gersh, J. B. Elgin, A. Berk, A. T. Stair, Jr., J. P. Bagian, and J. F. Büchli, "Release of liquid water from the space shuttle," *Geophys. Res. Lett.*, Vol. 17, No. 2, pp. 139-142, Feb. 1990.

2. R. A. Viereck, E. Murad, C. P. Pike, I. L. Kofsky, C. A. Trowbridge, D. L. A. Rall, A. Setayesh, A. Berk, and J. B. Elgin, "Photometric analysis of a space shuttle water venting," in Proceedings of the 4th Annual Workshop on Spacecraft Operations, Applications, and Research (SOAR '90), Albuquerque NM, June 1990, *NASA Conf. Pub.* 3103, pp. 676-680, 1991.

3. I. L. Kofsky, D. L. A. Rall, R. C. Garner, C. A. Trowbridge, E. Murad, C. P. Pike, D. J. Knecht, R. A. Viereck, A. Berk, M. E. Gersh, J. B. Elgin, A. T. Stair Jr., and A. Setayesh, "Photometric analysis of the venting of water from space shuttle," Paper 3.2, Proceedings of the European Space Agency Workshop on Space Environment Analysis, ESA WPP-23, 9-12 Oct. 1990.

4. I. L. Kofsky, D. L. A. Rall, M. A. Maris, N. H. Tran, E. Murad, C. P. Pike, D. J. Knecht, R. A. Viereck, A. T. Stair, Jr., and A. Setayesh, "Phenomenology of a water venting in low earth orbit," *Acta Astronautica* 26, 345-357, 1992.

5. J. B. Elgin, D. C. Cooke, M. F. Tautz, and E. Murad, "Modeling of atmospherically induced gas phase optical contamination from orbiting spacecraft," *J. Geophys. Res.*, Vol. 95, No. A8, pp. 12197-12208, Aug. 1990.

6. E. P. Muntz and M. Orme, "Characteristics, control, and uses of liquid streams in space," *AIAA J.*, Vol. 25, No. 5, pp. 746-756, May 1987.

7. J. A. Gardner II, D. L. A. Rall, I. L. Kofsky, A. Setayesh, and E. Murad, "Liquid dispersal study: A proposed space shuttle liquid release experiment," Paper AIAA-92-0793, 30th Aerospace Sciences Meeting, Reno NV, 6-9 Jan. 1992.

8. B. P. Curry, R. J. Bryson, B. L. Seibner, and J. H. Jones, "[Selected] Results from an experiment [on] venting an H$_2$O jet into high vacuum," AEDC Technical Reports TR-84-28 and TR-85-3, Jan. and June 1985.

9. H. Fuchs and H. Legge, "Flow of a water jet into vacuum," *Acta Astronautica,* Vol. 6, No. 13, pp. 1213-1226, Dec. 1979.

10. T. T. Kassal, "Scattering properties of ice formed by release of H_2O in vacuum," *J. Spacecraft Rockets,* Vol. 11, No. 1, pp. 54-56, Jan. 1974.

11. P. A. Bernhardt, "A critical comparison of ionospheric depletion chemicals," *J. Geophys. Res.,* Vol. 92, No. A5, pp. 4617-4628, May 1987.

12. J. S. Pickett, N. D'Angelo, and W. S. Kurth, "Plasma density fluctuations observed during space shuttle Orbiter water releases," *J. Geophys. Res.,* Vol. 94, No. A9, pp. 12081-12086, Sep. 1989.

13. H. Patashnick and G. Rupprecht, "Sublimation of ice particles in space," Martin-Marietta Technical Report ED-2002-1654, Denver CO, Mar. 1973.

14. J. W. Duff and J. B. Elgin, "Fuel dumps as an optical obscurant," Proceedings of the 1986 Meeting of the IRIS Specialty Group on Targets, Backgrounds, and Discrimination, Vol. 1, pp. 137-146, July 1986.

15. R. D. Sharma and C. Buffalano, "Temperature and size histories of liquid H_2, O_2 and H_2O particles released in space," *J. Geophys. Res.,* Vol. 76, No. 1, pp. 232-237, Jan. 1973.

16. W. T. Rawlins and B. D. Green, "Spectral signatures of micron-sized particles in the shuttle optical environment," *Appl. Opt.,* Vol. 25, No. 15, pp. 3052-3060, Aug. 1987.

17. M. E. Fowler, L. J. Leger, M. E. Donahoo, and P. D. Maley, "Contamination of spacecraft by recontact of dumped liquids," Proceedings of the 3rd Annual Symposium on Space Operations, Automation, and Robotics (SOAR '89), *NASA Conf. Pub.* CL-3059, pp. 99-104, 1989.

18. M. M. Pervaiz, S. C. Richtsmeier, M. E. Gersh, and L. S. Bernstein, "Radiation estimates for collisionally excited outgassed molecules," in Proceedings of the Vehicle-Environment Interactions Conference (ed's. R. E. Erlandson and C. -I. Meng), Applied Physics Laboratory-Johns Hopkins University, 11-13 Mar. 1991.

19. M. R. Torr and D. G. Torr, "Gas phase collisional excitation of infrared emissions in the vicinity of the space shuttle," *Geophys. Res. Lett.,* Vol. 15, No. 1, pp. 95-98, Jan. 1988.

20. L. T. Melfi, J. E. Heuser, and F. J. Brock, "Direct simulation Monte Carlo technique for modeling of the environment in the vicinity of the space shuttle Orbiter," *SPIE* Proceedings, Vol. 287, Paper 10, 1981.

21. S. G. Warren, "Optical constants of ice from the ultraviolet to the microwave," *Appl. Opt.,* Vol. 23, No. 8, pp. 1206-1225, April 1984.

22. G. R. Carruthers and J. S. Morrill, "Far ultraviolet cameras observations of airglow, auroras, and stellar occultations: quick look results," Paper SA21B-1, Proceedings of the AGU Fall Meeting, 9-13 Dec. 1991.

23. T. C. Degges and H. J. P. Smith, "A high altitude infrared radiance model," AFGL TR-77-0271, 30 Nov. 1977, ADA059242.

24. D.E. Koch, G. G. Fazio, W. Hoffman, G. Melnick, G. Reike, J. Simpson, F. Witteborn, and E. Young, "Infrared observations of contaminants from shuttle flight 51-F," *Adv. Space Res.,* Vol. 7, No. 5, pp. 211-223, May 1987.

25. S. J. Young and R. R. Herm, "Model for radiation contamination by outgassing from space platforms," *J. Spacecraft Rockets,* Vol. 25, No. 6, pp. 413-420, Nov.-Dec. 1988.

26. R. E. Meyerott, G. R. Swenson, E. L. Schweitzer, and D. G. Koch, "Excitation of the low lying vibrational levels of H_2O by O ^3P as measured on Spacelab 2," in Proceedings of the Vehicle-Environment Interactions Conference (ed's. R. E. Erlandson and C. -I. Meng), Applied Physics Laboratory-Johns Hopkins University, 11-13 Mar. 1991.

27. J. Crovisier, "The water molecule in comets: fluorescence mechanisms and thermodynamics of the inner coma," *Astron. Astrophys.,* Vol. 130, pp. 361-372, 1974.

28. J. W. Duff, S. C. Richtsmeier, L. S. Bernstein, H. K. Burke, and M. Pietrzyk, "Analysis of HAVE SLED II flight test water outgassing," Proceedings of the 1992 Meeting of the IRIS Specialty Group on Targets, Backgrounds, and Discrimination, pp. 9-19, Mar. 1992.

29. M. Heninger, S. Fenistein, G. Mauclair, R. Marx, and E. Murad, "Review of the reaction of O^+ with H_2O and its bearing on composition measurements from the space shuttle," *Geophys. Res. Lett.,* Vol. 16, No. 2, pp. 139-141, Feb. 1989.

30. A. L. Broadfoot, E. Anderson, P. Sherard, D. J. Knecht, R. A. Viereck, C. P. Pike, E. Murad, J. E. Elgin, L. S. Bernstein, I. L. Kofsky, D. L. A. Rall, J. Blaha, and F. L. Culbertson, "Spectrographic observation at wavelengths near 630 nm of the interaction between the atmosphere and space shuttle exhaust," *J. Geophys. Res. 97, 19501-19508,* 1992.

Table 1. Summary of Numerical Results of the *Discovery* Water-Dumping Experiment*

Quantity	Magnitude	Comment
Fragmentation-particle radius	0.13 cm ±20% (mean), little decrease in 2½ km	"Average" figure derived from the constraint; about twice the radius of the venting orifice
Fragmentation-particle mass fraction, density	98% when formed (~88% in the AMOS views), 120 per meter	Follows from Fig. 5, and estimated from the onboard video photographs
Recondensation-particle radius	0.3 ±0.05 μm initially, decreases with X as in Fig. 4	Derived from the best-fit to radiances data; transitions to Rayleigh-scatter
Recondensation-particle mass fraction, density	0.022 ± 0.007 of the initially-vented water, 2½ × 10^{11} per m	Derived from constraint from irradiances at the image planes of cameras at long and short ranges
Longitudinal particle velocity	23 m/s +5, – 8 m/s (systematic error)	Measured from sequential video images; indistinguishable from the radially-relaxed stream
Transverse particle velocity	3–4 m/s nominal average	Little kinetic energy is imparted by fragmentation
Particle temperatures	Small 180K, in <1 s Large 182K, in ~100 s	At equilibrium; refer to Fig. 4
Recondensation-particle cloud brightness 0.4–0.65 μm, at 48° and 33° aspect angle	2 x 10^{-6} W/cm^2 sr in a projection intercepting the symmetry axis at 1 km from the spacecraft	Calculated from the fractional water mass in and radius of these small droplets; see Fig. 2a

* 19.4 g/s of largely gas-free ~300K fuel cell product water vented at 329 km altitude in the daytime at low latitude through a 0.14-cm diameter 60°-conical nozzle.

Table 2. Optical Radiations from the Water Trail at Other than Visible Wavelengths

Water Component	Initial Fraction	Spatial Distribution	UV Radiance	SWIR Radiance	LWIR Radiance
Fragmentation Water/Ice Particles	0.84	As Fig. 2; X^{-2} uniformly in cone	Geometric sunlight scattering	Emissivity ≈ 1; weak scatter, weak thermal*	Negligible scatter, some thermal*
Recondensation Ice Particles	0.02	As Fig's. 1 and 2; X^{-2} in cone	Substantial near-Rayleigh scattering	Weak scatter, very weak thermal*	Very weak earth-shine scatter and thermal
Unrecondensed Vapor	0.14	See Fig's. 6 and 7	Negligible molecular scattering	Impact excitation and weak solar scatter ν_3-ν_1, plus OH vibrational	Impact excitation of ν_2 and rotational lines, weak earthshine

*Viewing perpendicular to the trail axis
at 1 m, 10^{-8} } 3-5 μm 10^{-6} } 8-13 μm Watts/cm^{2}sr(band)
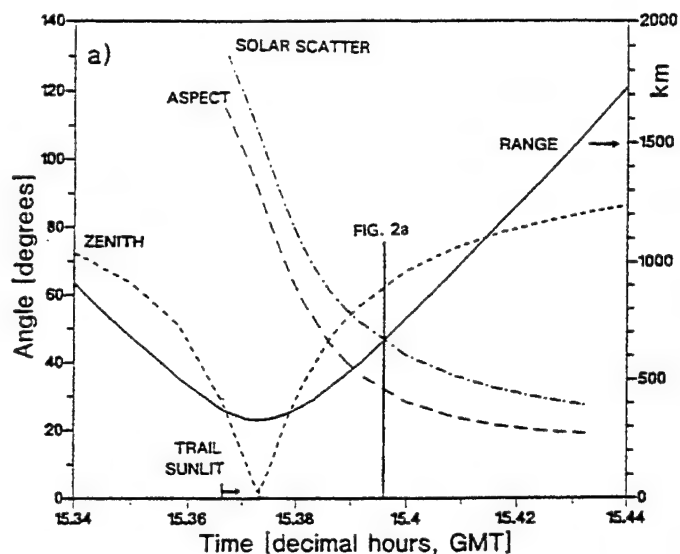at 1000 m, 10^{-12} 10^{-12} Watts/cm^{2}sr(band)

Fig. 1. AMOS viewing conditions for the *Discovery* water-venting experiment (16 Mar 1989).
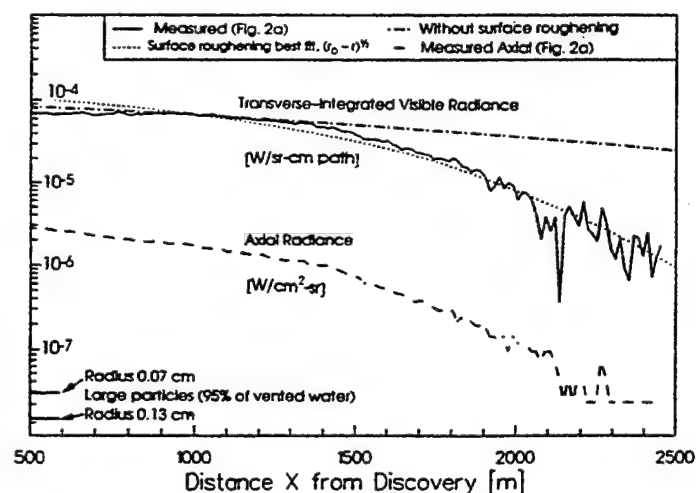

Fig. 3. Transverse and axial radiances extending downstream from spacecraft *Discovery* in Fig. 2a, with the normalized best fit to the time dependence of submicron particle radius as calculated in the text. (The slowly-sublimating large water-ice particles contribute little to the radiance signal at AMOS.)
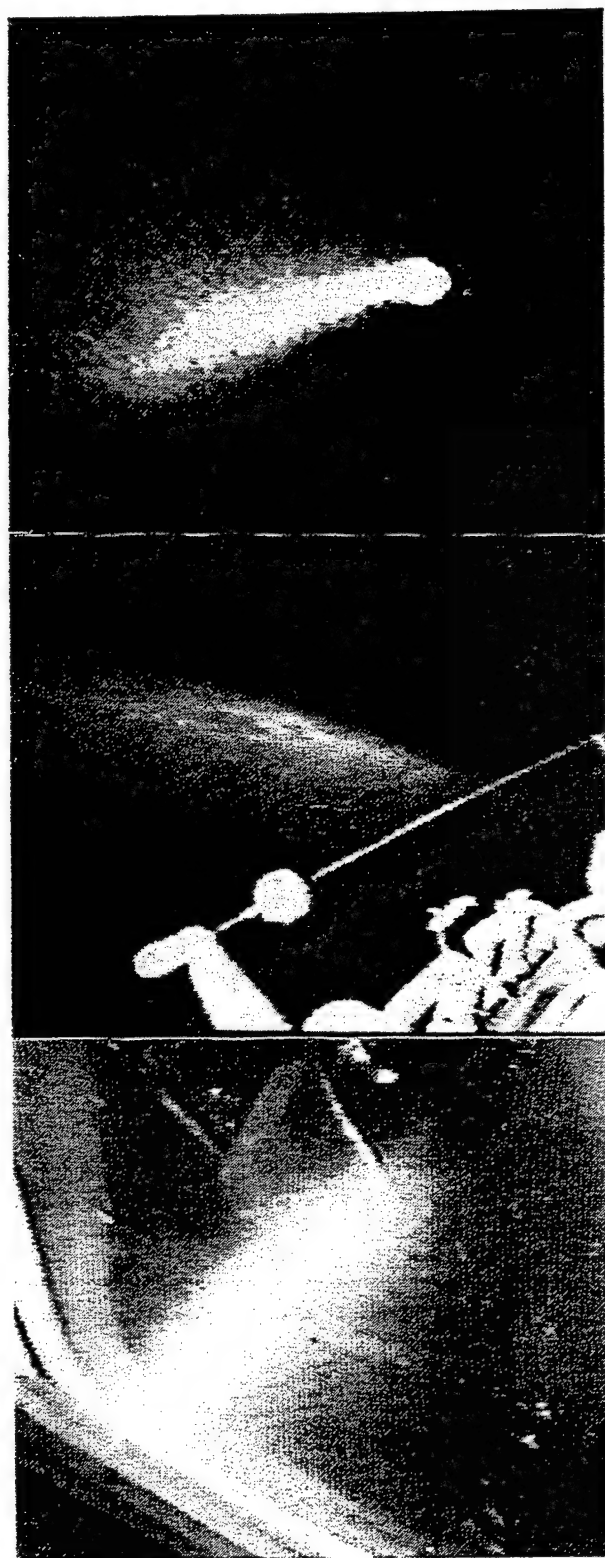

Fig. 2. Views of the sunlit water trail from AMOS (0.3° horizontal angular field) and two video camera stations onboard *Discovery* (-34° field).
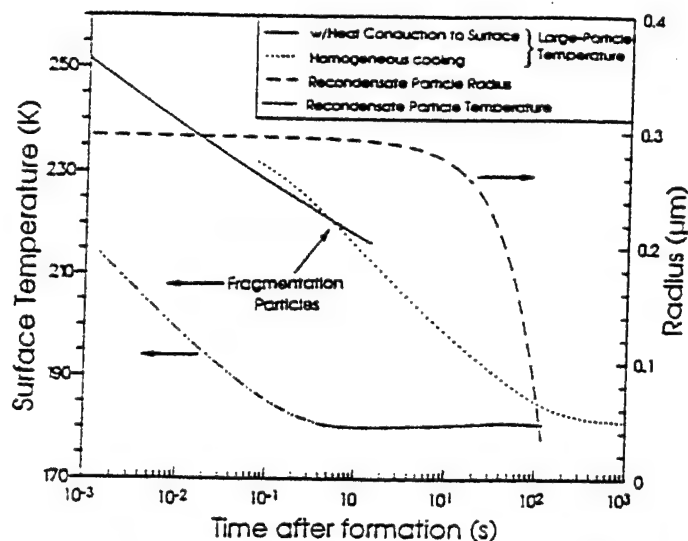
71

Fig. 4. Temperature and radius of the recondensation ice droplets derived from the AMOS video data and calculated temperature of the fragmentation particles.
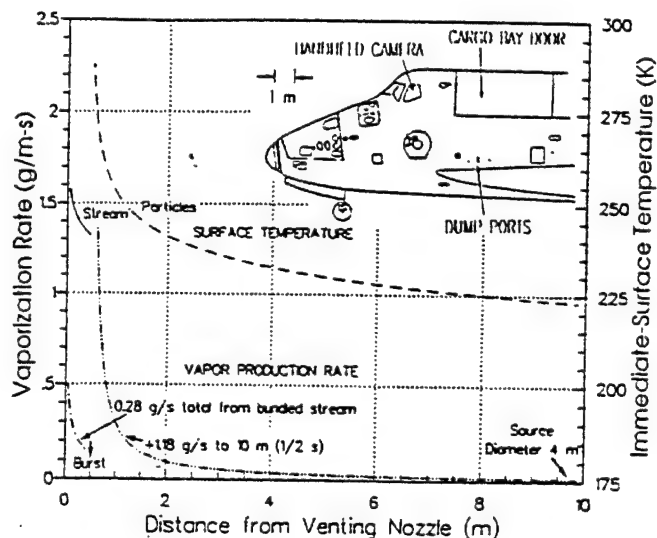

Fig. 5. Rate of evolution of water gas by evaporation/ sublimation the coherent water stream and its fragmentation droplets. The insert shows the location of the venting orifice on Shuttle Orbiter's port side.
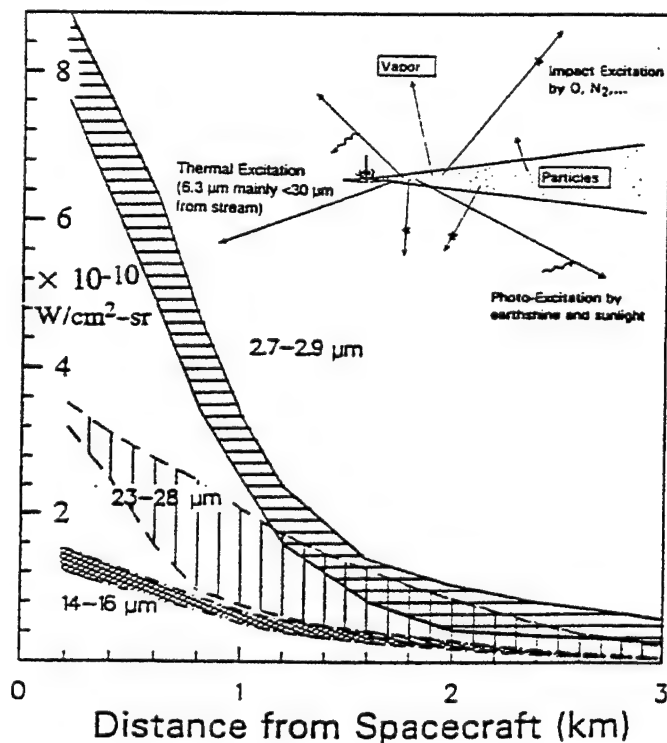
Fig. 6. "Look-in" radiances from the vapor collisionally excited in three infrared wavelength bands, scaled from direct simulation Monte Carlo calculations[18] for 6.6 km/s water outgassing at 300 km. The hatched areas indicate the variability among directly retrograde, posigrade, and perpendicular-to-orbital track view directions. The insert illustrates the three processes that lead to infrared emission from the evolved gas.

Fig. 7. "Look-in" radiances predicted by SOCRATES in the (1,0) vibrational band of OH for the venting conditions of *Discovery*. The corresponding foreground radiances looking out from the spacecraft (away from the stream direction) are nearly spherically uniform at 1×10^{-9} W/cm^2 sr. Total radiant intensity from the vapor reactions is 18 W/sr.

APPENDIX B

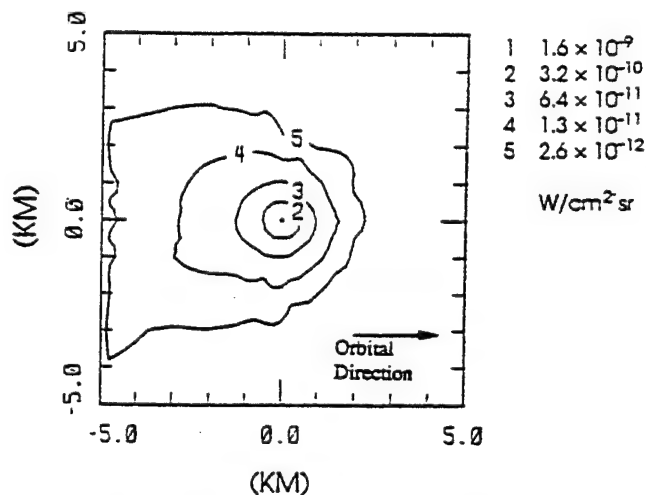## Persisting Radiation From Interaction of Solid-Propellant Exhaust Gases with the Atmosphere

January 1993

D. L. A. Rall and I. L. Kofsky
PhotoMetrics, Inc., 4 Arrow Drive, Woburn, MA 01801

D. J. Knecht, E. Murad, and C. P. Pike
USAF Phillips Laboratory, Spacecraft Interactions Branch (WSSI),
Hanscom AFB, MA 01731

ABSTRACT

Photometrically-calibrated visible light images of the exhaust trails from Antares IIa and Star 27 solid fuel rocket engines were obtained with a tracking, long-focus video camera at the Air Force Maui Optical Site. The observations were made at night during the SDIO Bow Shock 2 experiment, for which the firings took place at altitudes between 105 and 119 km. The luminous volumes associated with engine operation show the following principal properties: (a) they expand within <0.2 s to ~1 km transverse to the vehicle trajectory; (b) they have little further lateral motion (other than drift in the atmospheric wind); and (c) they exhibit pronounced limb brightening. Their spatial distribution and several-seconds persistence, which we quantified from both individual and sequential video images of the glows resulting from burn and smolder, show that the visible light cannot be thermal emission from the hot condensed Al_2O_3 exhaust or due to reactions catalyzed on the surfaces of these particles. With the assumption that the radiation is chemiluminescence from the reactions of a gaseous combustion-product species with ambient atomic oxygen, the photographic data lead to a depletion rate coefficient of the order of 10^{-12} molecules cm^3/s and an initial relative concentration of reactant ~5×10^{-4}. This phenomenological rate coefficient is close to those for the reaction of Al-containing small molecules with O atoms determined in laboratory and atmospheric chemical release experiments, in which similarly-persisting emission has been attributed to the formation of the intermediate AlO_2 ($^1B_2$). Consequently, the wake trails would have near-infrared radiances comparable with the 10^{-8} W/cm^2sr measured in the visible, as well as somewhat smaller radiances near 11 μm from cascade in the $AlO_2(\tilde{X})$ vibrational

1.0   INTRODUCTION

The second and third propulsion stages of the 18 February 1991 SDIO Bow Shock 2 (or "UV Diagnostic") Experiment[1,2] were solid-composite rocket engines that operated and smoldered at altitudes between 105 and 119 km. A visible trail persisted for several seconds along the trajectory of the Strypi-XI vehicle, which PL/WSSI photographed with a long focal length video camera at the ~350 km-distant US Air Force Maui Optical Site[3,4,5]. Representative images are in Figure 1. (Short-wavelength infrared glows associated with the bow shock of the thruster exhaust gases, and both SWIR and visible emission from the condensed Al_2O_3 exhaust particles were also imaged, and are to be analyzed separately.)

We determined the efficiency with which energy of these rocket motors is converted to $0.4 - 0.7$ μm photons by photometrically calibrating the electronically intensified camera against known stars in its field. The measured brightness distributions and dimensions of the wake glow are consistent with the interpretation that it is chemiluminescence from reactions of minor Al atom-containing species in the combustion-product gas with the abundant O atoms of the lower thermosphere; the liquid/solid Al_2O_3, which is well known to dominate the infrared signature of the exhaust of aluminized thrusters[6,7], plays no part. Similar selfluminous rocket trails have been previously reported[8], and indeed this persisting radiation may be a general feature of heterogeneous composite propellants based on aluminum granule fuel traversing the oxygen atom-rich altitudes of the atmosphere.

2.0   EXPERIMENT

2.1   VEHICLE TRAJECTORY AND ORIENTATION

Figure 2 shows schematically the flight path of the Strypi-XI relative to the mountaintop camera station (AMOS: 20.71°N, 156.26°W, 3050 m altitude), and Table 1 lists its altitude and velocity, elevation-azimuth and slant range, and angle between trajectory vector and line of sight. The ranges in Table 1 indicate that the image scale in Figure 1 is monotonically decreasing (by 14%) during the 35.4 s-duration second-stage operation; in addition changes in right ascension on the camera's astronomical mount have the effect of shifting the apparent direction of the trajectory.

The Bow Shock 2 experiment vehicle was launched at an azimuth of 202° from the USAF's Kauai (Hawaii) Test Facility (22.07°N, 159.75°W) at 14:18:35.0 UT/03:18:35 local standard time, with the moon below the horizon. After its first-(Castor) stage booster burned out near 40 km altitude, the Strypi-XI was reoriented so that its Antares IIa (Hercules X259A6) second propulsion stage, which ignited at 105.2 km–155.1 s after launch, produced a trajectory azimuth near 143°. (We henceforth measure times starting at this second-stage ignition.) This flight path resulted in 35°-40° nose-on view aspect angles from Maui during

burn of this engine, which increased to about 60° while it was smoldering. The spin rate about the long axis of the vehicle was 0.7 revolutions/s; its angle of attack rapidly decreased from 66° when the Antares ignited to 25° 10 s later, then to 12° in another 10 s, then decreased slowly to 8° at burnout, and during smolder varied between 8° and 15°.

After another 48.5 s, a third-stage Star 27 (Morton-Thiokol TE-M-616) solid-composite rocket motor propelled the vehicle generally downward from 119 km. Its spin rate remained 0.7/s, and its angle of attack oscillated with a 4-s period between 5° and 10°. The broadly similar formulation of this smaller thruster (see Table 2) also resulted in a persisting visible glow tangential to the Strypi-XI trajectory, less bright and with sensibly uniform diameter even near where it ignited. The velocity across the camera field of the rocket, on which the camera was then tracked for ~15 s, has then become too high for reliable determination of decay times; nonetheless radiance distributions transverse to the trajectory (such as those shown in Figure 13) could be readily measured. The Star 27 thruster, whose power output is intermediate between the operating and nominally burned-out Antares, thus represents a third sample in the exhaust-trail data set.

2.2   EXHAUST PROPERTIES

Table 2 lists the properties of the two solid-propellant engines pertinent to the luminous wake. The small (~20%), slow characteristic variation in thrust over their operation periods would not qualitatively alter the properties of the glow. Experience with other aluminized-solid formulations has shown that in addition to the major gaseous components listed measurable amounts of Al and Al_2O, AlCl and $AlCl_3$, and OH vapor, as well as trace amounts of other gases, may be exhausted[9]; furthermore, some of these low-concentration molecules can be expected to be hydrated or weakly chemically bonded to other exhaust species.

Figure 3 is a plot of the kinetic temperature and densities of atomic oxygen and all atmospheric species over the measurement altitude range, derived from a MSIS calculation[10] for the geophysical conditions. The ambient mean free paths for elastic collisions are of order 1 m, much less than the characteristic dimensions of the radiating wake volume.

2.3   CAMERA

A non-standard tracking method was devised by the AMOS operating staff to enable the Acquisition Telescope System (AATS) finder for the main "MOTIF" 1.6 m telescope to operate at the high zenith angles of the Strypi-XI flight path. This f/5, 15-cm clear aperture video camera has a 40 mm-diameter Intensified Silicon Intensifier Target photodetector with S-20R spectral sensitivity (FWHM photon response is 3800-6700Å). Its 3.0°-diagonal field was fixed on the initial segment of the visible wake until 16 s after the Antares ignited, and afterward was tracked on the overexposed image volume near the rocket.

3

2.4 RELATED OPTICAL DATA

Persisting radiation from the Antares burn was also photographed in ~15 km-long segments from the "LACE" low-earth-orbiting satellite[11], by an intensified charge-coupled device ("tracker") camera whose spectral response is relatively flat between 3000 and 4400Å and extends to 2500 and 4500Å (and thus overlaps that of the AMOS system; see Figure 14). Other ("plume") LACE cameras sensitive in narrower wavelength spans below 3400Å failed to detect the persisting glow. In addition the optical signal from Antares smolder appears to be below the thresholds of all the satellite cameras, and the Star 27 radiation is not reported. The LACE data released so far are consistent with the information that we have extracted from the multiple higher spatial resolution groundbased visible-light images.

Narrow-field photometers and a spectrometer viewing into the wake hemisphere from onboard the Strypi-XI measured ultraviolet radiations from the condensed exhaust and hot gases[6], which we judge to be unrelated to the persisting far-field emission seen from AMOS.

3.0 DATA

3.1 OVERVIEW

The instrumentally-bloomed area at the head of the wake trail is the thermally-radiating microns-scale Al_2O_3 particles of the rocket exhaust (the nozzle cone opening to the bright engine combustion volume itself is directed away from the camera). This feature has weakened and appears to break away from the then-broader trailing glow area in the video frame at 35-11/30 s after the Antares ignited. It goes out of the camera field of view 27/30 s later, and is undetectable when the Strypi-XI comes back into the field after another 3-28/30 s.

The persisting Antares trail itself can be seen in Figure 1 to consist of *1)* a highly irregular area that develops within 1 s after ignition, followed by *2)* a smooth bifurcated region that shows strong limb brightening up to at least 14 s. After about 25 s, when the camera has re-acquired the rocket, this latter volume takes on *3)* a somewhat "billowed" longitudinal structure with sensibly constant 1.2-km width along its ~25-km length within the image field. The surface radiance of the initially-produced rough volume varies over a range of almost a factor three, with no characteristic cell size (in this view projection). It shows some evidence of initially rotating about the trajectory direction—most probably due to the vehicle's rotation--, and its maximum width perpendicular to the flight path increases by only a factor about two between 2 and 16 s. *4)* A lower-edge "finger" also about 1¼ km across extends with a mean velocity of 300 ± 50 m/s to at least 5 km down the retrograde trajectory direction from this initial radiating region. This protuberance is also brightened along its outer borders, and furthermore gives the impression of breaking into two overlying quasicylinders.

Although the initial radial expansion rate of the luminous column cannot be accurately measured because of video blooming from the hot exhaust particles, a rough estimate of 4 km/s can be made from the less-exposed frames near burnout. No early oscillation of this hard-edged volume can be detected at the spatial and temporal resolution of the images, and as shown below its later apparent width changes very little. This rapid initial outward expansion is strong evidence that the persisting luminosity is due to gases rather than related to the condensed Al_2O_3 exhaust droplets, which besides thermally radiating at visible wavelengths could in principle be serving as recombination surfaces for the gaseous exhaust species. These particles would not undergo so large a lateral scattering in < 1 s, or pile into an irregular volume part of which moves backward along the exhaust direction at near the local sound velocity; furthermore they would not move coherently horizontally at a typical E-region wind speed, as the glow is seen to do between -25 and 37 s. Indeed, both simple aerodynamic drag arguments and a computational fluid dynamical model of the two components of the exhaust flow[6] show that the particles travel largely unimpeded from the $\pm 15°$ engine exhaust cone.

The initial optical yield rates per unit flight path during the > 40 s-long after-burn period (final two frames in Figure 1) are between one and two orders of magnitude lower than those from engine firings. In contrast to the latter glows, this smaller-radius (and higher-altitude) volume becomes noticeably broader within a few s after the rocket has passed. A more or less regular-appearing longitudinal variation of its initial width during this period is most probably due to the azimuthal asymmetry of smolder-exhaust flow as the rocket vehicle rotates about its long axis; however this spatial structure is not sufficiently distinct to allow a reliable period to be extracted. Similarly, as mentioned just above, the longitudinal radiances in the original video images between -25 and 35 s after Antares ignition show a weak modulation near the Strypi-XI, with the 1 - 2 km characteristic length that would be associated with its rotation. These low-contrast, poorly-defined cells give the appearance of remaining stationary (an estimated upper limit to their retrograde velocity is 300 m/s).

3.2   DATA REDUCTION

To compensate for discrete manual adjustments made to the camera gain, we calibrated separately sets of frames against the photocurrents produced by stars of known magnitude and spectral class. The irradiances within the camera's FWHM response from individual stars that we identified from standard charts and the SkyMap listing[12] were corrected for the small attenuation by the atmosphere above AMOS using LOWTRAN (as in[4]). We digitized the photocurrents from the analog videotape to eight bits, and then summed these currents above the dark-noise baseline in the instrument-spread "images" of these calibrating point sources. The effective halfwidths of these blur spots serve to convert the irradiance distribution at the focal plane from each star to its equivalent peak "radiance" in object space, to which the output currents in the images of the spatially-continuous trail are referenced. The absolute radiances outside the atmosphere (in Figures 9 and 11) refer to the 3800-6700Å photon FWHM of the camera. Their estimated overall accuracy, taking into account the difference in

77

spectral distributions from the typically-6000K blackbody calibration sources and the glow (whose emission spectrum, while not measured, is most probably the continuum in Figure 14), nonlinearity of the AMOS camera's response, and uncertainties from attenuation by aerosols along the low elevation angle sight path above the mountaintop station, is ± a factor 2½.

We determined the dependence of optical yield rates on time after passage of the Antares by measuring both their decrease in successive video frames at a fixed position (to the extent allowed by the data) and in single frames at a series of retrograde positions. This second measurement averages over altitude. In the static frame of reference of the atmosphere the mass of combustion gases exhausted per unit length remains independent of Strypi-XI velocity within the error of the video data, for Antares at an average of 8 g/m. Furthermore, the transport of this material does not change substantially with air density, as evidenced by the nearly constant cross-track extent of the wake and the aforementioned slow (if any) downstream motion of its low-contrast internal structure. Thus the space rate of deposition of reactant(s) is an almost stationary factor in the radiation process.

3.3   NUMERICAL RESULTS — ANTARES BURN PERIOD

Figure 4 is a set of transverse profiles of the gain-standardized photocurrents (averaged over six adjoining longitudinal pixels to improve signal/noise) at 3.0 s after passage of the Antares engine, at altitudes between 105.8 and 110.9 km. (Uncertainty in the individual radiometric calibrations precludes quantitative intercomparison of the photon yield rates per unit length along the trajectory.) Figure 5 is a series of summed photocurrents from transverse profiles at a fixed gain--i.e., area integrals of traces such as those of Figure 4 at the same ratio of radiance to photocurrent--, over a 3.4 s time span after the engine had burned out. The emission rates can be seen to decrease with time at each retrograde position, which is to say, at all altitudes along this segment of trail. In Figure 6 the crosswise-integrated photocurrents at 2 s after burnout have been corrected for the monotonically increasing velocity of the rocket-- i.e., placed on a time-since-deposition scale--, and this output signal has been normalized to the undisturbed concentration of atomic oxygen. This last step is an application of the hypothesis that [O] is the rate-limiting factor in chemiluminescence of the exhaust gases; we return to this critical point below. The thus-interpreted decrease in output current is exponential within the resolution of the measurements, with an e-folding time between 11 and 15 s. (These low signal/noise data can of course be fit by other functional forms.)

This derived time represents the mean characteristic decay period of the total visible-light output rate per unit length over the 108 to 111-km altitude range, in the first ~14 s after passage of the thruster. Since physical transport of the reactants plays an important part in the luminescence process (as we will show), this figure is not a chemical-reaction or exhaust molecule-depletion, or peak surface brightness-decay time; for example it would be expected to decrease as the exhaust and ambient atmospheric gas become more mixed. A similar reduction-analysis of the summed radiances from traces across the trail at 35 s, at five previous

deposition times up to 13.3 s (those in Figure 7), gave a best-fit exponential time constant of 13 s, consistent with the result in the previous paragraph from the frame 2 s later. Figure 8 shows the volume emission rates derived from these crosswise profiles.

We also determined this initial decay time averaged over a narrow span of altitudes, by staring at the series of images recorded between 35 and 38 s. Figure 9 presents the resulting sums of photocurrents above instrument baseline in the rectangular area indicated in Figure 1, which bounds 108.2 ± 0.2 km. The least-squares best fit exponential slope of these photon yield rates is 13 s. This agreement with the result for the wider range of altitudes (in Figure 6) gives credence to our normalization of the emission to the local concentration of oxygen atoms, and thus to the idea that O--or another atmospheric species with a similar scale height-- is participating in the reaction(s) responsible for the visible luminosity.

At 8 s after the rocket has passed the power radiated as visible light near 108.2 km altitude is 6 kilowatts per km. With the rather gross approximation that the fractional decrease rate remains exponential at $1/13$ s^{-1} this figure leads to a total energy output of 140 kilojoules/km. This optical yield may be compared with the total energy provided by the thruster, 10,000 megajoules expended over 50 km of flight path $\approx$ 200,000 kilojoules/km. Thus the efficiency with which chemical energy of the Antares propellant is converted to S-20R photons at this altitude--albeit through what we are interpreting to be a reaction of its combustion product(s) with a labile species in the atmosphere--is 0.07%.

The series of image scale-corrected photocurrent traces across a single image in Figure 7 at times between 5.2 and 13.3 s after rocket engine passage shows little difference in the projected widths of the radiating volume. (These times of course also represent a range of atmospheric altitudes.) Figure 10 plots the similar transverse radiances at the fixed altitude 108.2 km over a 3½-s period; again the video data fail to resolve any significant change in width of the visible afterglow. To assess the transverse growth in the absence of chemical consumption of the reactants, we applied a simple transport-only model in which the laterally-expanded exhaust gas interdiffuses with ambient air that it has initially compressed and heated[13] (as is further described below). Adoption of an effective diffusion coefficient 2 – 3 times that for the undisturbed atmosphere at 108 km, which is 2×10^6 cm^2/s[14], leads to the prediction that the widths would increase by about 250 m in 8 s or 170 m in 3½ s. The fact that the volume from which glow arises is expanding at a substantially slower rate--if at all--is evidence that the concentration of exhaust reactant(s) is being eroded at a fractional rate much greater than $1/13$ s^{-1} where it contacts the swept-out, overdense local air.

The coherent movement of the luminous region relative to stars observed in the video images (not discernible in Figure 1) corresponds to a horizontal velocity of 70 m/s in the direction perpendicular to the camera line of sight (along azimuth 285°), which is within the normal range of atmospheric wind speeds at the Strypi-XI altitude. This transport further emphasizes that the radiation is coming from a gas rather than -microns-diameter particles,

which would not follow the wind field. Since a star clearly shows through the glow volume (see Figure 11), it must be optically thin over at least part of the S-20R wavelength range.

The relatively flat tops of the transverse traces in Figures 7 and 10 show that the emission is arising principally from near the outer edges of the image-producing wake region, which we interpret as being essentially cylindrical on the basis of the single camera projection and simple growth-symmetry arguments. This limb enhancement is quantitatively evidenced by the emission rates per unit volume in Figure 8, which are Abel inversions of the set of radiances at 35 s. The unfold procedure applies the physically reasonable assumption that these rates depend only on radial distance from a symmetry axis in half-cylinders on either side of the plane defined by the lines of sight from the camera through this axis (and that the volume is optically thin to its own radiation). The depths of the troughs and widths of the edge regions in Figure 8 are subject to error from Abel-inversion differencing of the already-noisy photocurrents. Figure 11 is an isophote contour plot that includes one of the 1-D scans that were unfolded, with an absolute radiometric calibration.

Limb brightening is also obvious in both the irregular and relatively-smooth radiating regions that develop before 16 s; refer again to Figure 1. As the exhaust trail ages, its surface brightnesses (in Figures 7 and 10) exhibit less spatial modulation, and in addition its high volume emission rate outer "annular" regions (in Figure 8) broaden and flatten. This damping/smoothing is expected from the diffusion lengths estimated just above, which would be about same within the exhaust gas as where it is mixing with air that it has displaced.

3.4 NUMERICAL RESULTS — ANTARES AFTER-BURN

A similar analysis of the luminosity associated with smolder of the Antares engine is summarized in Figure 12. Using a bright star on each side of the trail as position references (refer to the frame at 49 s in Figure 1), we were able to stare for 3 s at a fixed 0.5 km-long segment of this glow centered at 114.5 km altitude. The radiating region appears Gaussian-shaped even at the earliest times after the rocket passed, and has a characteristic width that increases with $(time)^{1/2}$. Applying the theory of a reacting (or inert) species diffusing into a uniform, isothermal, undepleted atmosphere[15], we find that the slope of the plot in Figure 12b leads to a diffusion coefficient of $9 \pm 2 \times 10^6$ cm^2/s. This is roughly three times the small-molecule diffusion coefficient in the undisturbed atmosphere, an excess most likely due to the initially high mean temperatures[6,13] of the exhaust gas and air it contacts. An extrapolation to zero time (following the procedure developed for analyzing the growth of chemical-release clouds at thermospheric altitudes[15]) gives an initial Gaussian full width of 0.18 km.

The exponential decay period of the total emission rate per unit length of smolder trail is 3.5 ± 1 s (Figure 12c). This is about one-quarter of the characteristic time we derived for the afterglow of the Antares burn, despite the concentration of the putative rate-controlling species atomic oxygen now being almost a factor two lower. This difference comes about

because the less dense smolder exhaust gas does not coherently displace the local oxygen atoms, but merely intermixes with them, as we explain in Section 4.2.

A comparison of transverse traces in Figure 7 just before and after the propellant was nominally consumed shows that the exponential decay-corrected rate of emission of visible light per unit path early in the smolder is a factor 20 smaller than during burn. (The Antares engine is known to have finite residual thrust, but it cannot be quantified from the radar tracking or other housekeeping data.) As in Figure 12, which refers to a 3.4-km higher altitude and 12-s later time after burnout, the radiance pattern has an essentially Gaussian shape rather than the hard ("shock"-like) edge that results from full thruster operation.

3.5   NUMERICAL RESULTS — STAR 27

Figure 13 shows three transverse traces from the similar selfluminous trail left by the third-stage rocket motor, extending over 0.8 s near 118½ km altitude where the trajectory is nearly horizontal. The increased tangential velocity of the Strypi-XI and its tracking position at the center of the video frames make the period over which identifiable emitting segments remain in the camera field too short for quantifying the decay times by staring at fixed radiating downstream volumes. Nonetheless, these times appear to be substantially longer than the 3½ s of the lower-altitude (and higher oxygen atom density) glow from the Antares after-burn, and comparable with those from the Antares burn. As with the Antares operation, no lateral growth of the luminous trail left by the Star 27 is detectable; indeed, its "width" may be decreasing, or even oscillating. Abel inversions of these noisy traces show a relatively flat volume emission rate, with some evidence of limb brightening.

4.0   INTERPRETATION

4.1   EXCITATION MECHANISM

Thermal emission from the condensed Al_2O_3 can not be responsible for the wake glow, not only for the "geometry" reasons stated above but also because these microns-scale droplets cool radiatively in much less than 1 km to temperatures at which their output of visible photons becomes negligible. Furthermore, their angular divergence[6] precludes the interpretation that particle surfaces are catalyzing excitative reactions of the combustion products with atmospheric gases, or among exhaust (or for that matter ambient) species.

The radiation would also not be due to homogeneous reactions among combustion-product molecules cooled by expansion, not only because no chemiluminous reaction among them is known to proceed at a significant rate at the relatively low temperatures they reach after a few s[13], but also because the volume emission rates increase outward while the densities of these gases increase steeply toward where they are formed[6,13,16,17]. (This latter

observation also rules against radiation from metastable exhaust species.) In consequence we pursue the hypothesis that the luminosity is due to a reaction of a lower-thermospheric component such as the highly labile, abundant $O(^3P)$ atoms with either one of the major combustion products or exhaust constituents present at lower concentrations.

Excitative reaction of atomic oxygen with an aluminum compound outgassing from smoldering solid-composite propellant has in fact been advanced[8] to explain the geometrically and temporally similar visible radiation produced by the Nike-Hydac booster engine (Lockheed Propulsion 9.4-KS-10200) of the "Precede" experiment when it reached 88 km altitude, about 1 min after it had burned out. A preliminary analysis of the incompletely-documented data set suggests that the persistence of the Precede glow depends on the total air density as well as [O], that is, that the excited species is subject to collisional quenching.

Comparisons of the visible-radiance distributions measured at AMOS furthermore implicitly assume that the spectral distributions are about the same while both thrusters were operating and during the Antares after-burn, that is, that the excitation process remains the same. This assumption is justified if 1) the two solid propellants exhaust the same relative amount(s) of chemiluminescent-reaction species, and 2) the products of smolder are evolved primarily from continuing combustion of pieces of the previously continuous solid composite (the inner propellant-container lining of fiberglass and buna rubber also slowly "burns").

4.2   EXHAUST TRANSPORT AND SCALING

To address this chemiluminescence issue information about the spatial distribution of the combustion gases is needed. Guidance is available from standard explosion theory as well as from numerical calculations of the transport of rocket exhaust gases; a recent analysis[6] for Bow Shock 2, for example, specifically treats the early hydrodynamics of the Antares and Star 27 exhaust but does not lend itself to heuristic scaling of the flows to later times. We apply the so-called similarity solutions for chemical explosions at high altitudes[13,18], which agree with both the photographic observations of for example aluminized grenades[19] and results of numerical models of releases of gas from orbiting (i.e., high-velocity) spacecraft[17].

Above a critical ratio of [explosion energy released per unit ambient pressure]$^{1/3}$ to [collision mean free path], a Rankine-Hugoniot shock forms; the energetic, self-colliding explosion-product gas, whose density and temperature decrease outward, sweeps out (and in so doing heats) virtually all the air in a volume proportional to [energy/pressure]. The later transport of the explosion and background gases is essentially diffusive. In spherically-symmetric blasts[13,20,21] the radius of this initial-scale or pressures-equalization volume, after a few moderate-amplitude oscillations, reaches $0.21 \cdot$ [energy/pressure]$^{1/3}$. As the input energy decreases and the altitude--i.e., mean free path--increases the shock becomes thicker, increasing the fractional volume of the explosion gas in contact with the atmosphere, and eventually this boundary becomes undefined.

This relatively standard similarity modeling--all flow quantities having the same dependence on distance from the source--has been found to give reasonably accurate predictions of the hydrodynamic growth of chemical (and even nuclear) explosions in the atmosphere. (For example, when in experiment "Firefly Jeannie"[13] 18 kg of cyclotrimethylenetrinitramine ("RDX")-$CsNO_3$-Al was exploded at 109.7 km this pressures-equalization radius was in close accord with the prediction.) Similarity theory can be extended to the rocket-combustion products by considering the propellant burn as a "line" explosion with cylindrical symmetry[20,22]. Since the average outward speed at which the initial-scale radius is established exceeds the vehicle velocity during the Antares operation and smolder (and also during much of the Star 27 burn), this approach can be expected to be only approximate; that is, the line does not detonate simultaneously everywhere, but the also has attributes of a temporal sequence of point (spherically-symmetric) explosions.

With this straightforward approach the initial equilibration radius becomes proportional to [energy released per unit length/ambient pressure]$^{1/2}$ [21,22]. Applying this dependence to the Antares exhaust between 108.2 and 110.9 km altitude (taking into account the small decrease in engine thrust over this 25- to 30-s burn period, which was measured in flight), we find that this radius would increase by only about 15%. Such a small change is within the error of definition of the "edges" of the transverse photocurrent traces across the aged trail in Figure 7, which are being altered by diffusion with simultaneous chemical consumption--and, perhaps more importantly, represent line-of-sight column sums of products of concentrations of the two reactive gases (weighted by a perhaps temperature-dependent rate coefficient) rather than solely of concentrations of combustion molecules. Similarly the profiles of the 3 s-old volumes over the broader range of deposition altitudes (in Figure 4) agree within their accuracy with this simple scaling rule. (The bifurcated glowing region up to 25 s after Antares ignition, since it stems from the initial azimuthal nonuniformity of the solid-propellant burn--as we hypothesize later--, would not be expected to show the same scaled lateral dimensions.)

More significantly, this scaling applied to the transverse extent of visible glow from the lower-power, higher-altitude Star 27 gives agreement with this average from the late Antares burn. If we interpret the pressure-equilibration radii as the intercepts of lines tangent to the straight segments of the radiance profiles on the video dark-current baseline (a plausible definition of the "contact surface" separating the two gases), the observed mean proportionality factors for the Antares averaged over 108.2 - 110.8 km and for the Star 27 at 118.5 km are 0.21_5 and 0.19 respectively. In view of the potential error from this definition of the radius at which the two gases contact and in measuring these positions from the noisy video images, as well as from the model atmosphere and the energy output rates along the trajectory (which we took from post-flight rocket thrust profiles), the match can be considered satisfactory. The fact that this experimentally-determined proportionality factor is close to the 0.21 observed from spherically-symmetric blasts[13] (even when the small correction for the difference in radius increment that produces the same change in gas volume is applied) reinforces the above-mentioned idea that combustion of the propellant exhibits characteristics of a sequence of point

shock-producing explosions. This numerical factor should of course be interpreted only as a heuristic, lumped-parameter figure for scaling the emitting volume to the energy released

Extension of this principle to the Antares smolder is hampered by both this energy output rate being only approximately known and the fact that the outward distance over which the exhaust gas diffuses very quickly becomes comparable with the observed small initial glow radius (so that this equilibration radius is not well defined experimentally). An estimate of the longitudinal deposition rate, which applies assumption 2) above--that the ratio of engine power output to mass of radiation-producing reactant exhausted per unit time is the same after and before burnout--, can be made from the measured visible-light emission rates (which as mentioned are in the ratio 1:20) and decay lifetimes. If we take the radiation time scales to be dominated by chemical consumption in the smolder volume and by fluid-flow from engine burns, and assume the residual Antares thrust to remain the same at 114.5 km as near 111 km, the energy deposited per unit length at 114.5 km would be closely $(1/20) \cdot (3.5/13)$ times the average between 108.2 and 110.8 km. Following the procedure for chemical trail releases in the upper atmosphere[15], we adopt the intercept on the ordinate in Figure 12b to define the transverse distance at which the gas pressures equilibrate. The ratio of this radius to [smolder energy deposition rate/air pressure at 114.5 km]$^{1/2}$ is then 0.17.

The luminous volume resulting from the much weaker and somewhat higher-altitude "explosion" of smolder almost immediately exhibits a rounded profile because the contact surface with the ambient atmosphere is many ~3-m collision mean free paths thick[16,20]; in contrast with the rocket-propellant burns, the reservoir of dense exhaust gas near the trajectory almost immediately encounters reactive oxygen atoms. Hence the depletion rate of the chemiluminescence-producing combustion species is greater than when an atmosphere-sweeping-out front develops, in which case chemical consumption must await diffusive intermixing of the two species. This observation is further supported by the measurement by the satellite-borne ultraviolet camera of a several 10's-second (exponential) decay of peak radiance in the large region where Antares exhaust initially deposits[11], which is in the direction expected from the low ratio of surface to volume of this region.

We ascribe this early-developing irregular luminosity and succeeding few seconds of transversely separated but otherwise relatively smooth glow (refer to Figure 1) to nonuniform combustion of the Antares propellant. Indeed, the number of discrete-appearing "cells" in the prominent and persisting rough-surfaced region is comparable with the number of points in the cross-section of its propellant grain. (No change in velocity that would lead to a transition from turbulent to laminar flow into the stationary atmosphere is taking place during this initial burn period.) The edges of this region move outward at much less than molecular-diffusion speeds because, like those of the smoother glow region, they are being chemically eroded. A rudimentary such initial bright patch appears in the video photographs of the Star 27 burn, nonuniform in radiance but with about the same diameter as the later-developing exhaust column; presumably, this smaller thruster engine had relatively weaker startup transients.

We interpret the rounded finger that extends from this irregular Antares region as a retrograde extension of the early-developing quasicylinder(s) that results from axial expansion of the high-pressure exhaust into undisturbed air, at or near the local sound speed. This gas is confined radially by the background air that it has compressed.

Not only would solid-composite motors having other chemical compositions and grain configurations exhibit both different residual thrusts and relative outputs of reactive molecules, but also individual Antares and Star 27 units would be expected to burn somewhat differently. The hydrodynamic scaling indicated here would apply to the pre- and post-diffusion period radius of the wake glow from a given spatial rate of energy output, and only indirectly addresses the issue of yields of visible (and other) photons.

4.3 CHEMILUMINOUS REACTION

We look, then, for reaction processes of one or more exhaust species that lead to the following measurements.

1) Lifetime against chemical consumption 3½ s at 114½ km altitude, where the exhaust gases can be considered uniformly mixed with the local atmosphere. With the ambient reactant taken to be O, whose concentration is $2 \times 10^{11}/cm^3$, this figure would indicate a bimolecular rate coefficient for disappearance of the exhaust reactant of $([2 \times 10^{11}/cm^3] \cdot [3.5 \text{ s}])^{-1} \approx 1\frac{1}{2} \times 10^{-12} \text{ cm}^3/\text{s}$.

2) Column visible-light emission rates from the Antares burn of order $10^{-8} \text{ W/cm}^2 \text{ sr} \approx 2 \times 10^{11}$ photons/cm²-column s (see Figure 11). This figure indicates volume emission rates near 5×10^6 photons/cm³ s in the outer regions of the glow.

3) [from the satellite radiometry[11]] Blue and near-ultraviolet column emission rates of order $10^{-9} \text{ W/cm}^2 \text{ sr}$.

A further useful input to the interpretation is the concentration of all exhaust molecules in the essentially stable, 1.2 km-diameter Antares quasicylinder (see Table 2). This concentration initially decreases rapidly with radial distance from the flight path[13] and has a mean of $(2 \times 10^{21}/\text{cm of trajectory})/(\pi [1.2/2]^2 \text{ km}^2) \approx 8 \times 10^{11}/\text{cm}^3$.

A review of the chemiluminous reactions of the more abundant combustion products of solid composite motors with oxygen (and nitrogen) failed to identify any that proceed sufficiently rapidly at the low temperatures reached in the expanded exhaust to agree with these observations. While "blue flame" radiation from CO_2 ($^1B_2 \rightarrow \bar{X} \ ^1\Sigma$) is produced when CO combines with O, the rate coefficient for even the non-luminous three-body reaction[23] falls several orders of magnitude short of providing the volume emission rates measured by both the

AMOS and LACE cameras. Similarly the well-known yellow-green glow from recombination to NO_2^* can be ruled out because it would require unrealistically large amounts of NO in the engine exhaust (and would be inconsistent with the LACE observation).

In contrast, some small molecules that contain Al atoms are known to react exothermically with oxygen in both the atmosphere[19,24] and laboratory[25,26] to produce closely-packed electronic bands (they resemble a continuum) that extend from the near-infrared to a cutoff just below 3400Å (3.7 eV). This short-wavelength limit corresponds to the association energy of AlO with ground-state O to form AlO_2. As Figure 14 shows, the spectral distribution resulting from this process is consistent with the above-mentioned observation that more photons are emitted from the wake trail at the S-20R wavelengths to which the AMOS camera responds than in the blue and near-UV where the LACE satellite's "tracker" camera is sensitive; furthermore the cutoff is to the red of the response wavelengths of the LACE "plume" cameras, which as mentioned failed to detect wake trails.

Radiation with sensibly the same spectrum and persistence (~2 – 100 s) was observed when Al was released between ~90 and 200 km at night 1) bound in trimethyl aluminum (TMA-Al(CH$_3$)$_3$), 2) as a component of CsNO$_3$ aluminum-powder burners (which are in effect miniaturized solid composite rocket motors), and 3) contained in explosives[19,24]. (Control TNT/RDX grenades without Al granules produced no such luminosity.) In addition, as best as can be determined from the uncalibrated "Precede" images[8] the exponential lifetime of the aforementioned chemiluminescent wake of the burned-out Nike-Hydac motor was ½ s at 102 km and 1 s at 108 km; these times are consistent with the 3½ s "chemical" lifetime that we measured at about a scale height above the latter reaction altitude.

The current conclusion[26] from these in-atmosphere experiments and supporting laboratory measurements is that the upper state(s) of the transition is excited in a substitution reaction $XAlO + O \rightarrow AlO_2(^1B_2) + X$. The weakly-coupled adduct X is thought to derive from reaction-generated or rocket-contaminant H_2O[25] (insofar as the visible glow is prominent in the presence of water vapor). Other candidate reaction-stabilizing species that may be bound to AlO are OH, Cl compounds, H, or even another AlO molecule.

4.4 SPECIES CONCENTRATIONS AND RADIATION AT OTHER WAVELENGTHS

A lower limit to the effective rate coefficient for producing visible radiation from this reaction is 10^{-13} cm^3/s[26]. This figure is as expected less than the $1½ \times 10^{-12}$ cm^3/s that we derived in the previous subsection, which refers to the consumption reactions of the trace exhaust species: only some fraction of these would be expected to result in population of excited electronic state(s) of the product molecule. An extrapolation from the visible emission spectrum of AlO_2 formed by recombination-substitution[26] (and experience with other triatomic oxides) leads to the prediction that an about equal number of photons is emitted at near-infrared wavelengths; refer to Figure 14. (In addition, the AMOS camera also responds only

weakly to the ~5% (of the total) ultraviolet photons.) Thus the ratio of inferred rate coefficient for consumption of XAlO to the rate coefficient for producing photons in the visible range has an upper limit of somewhat under 10. Combining these figures with those stated above, we find that an upper limit to the radially-averaged initial concentration of XAlO in the exhaust gas is $(2.1) \cdot (10) \cdot (5 \times 10^6$ photons/cm^3 s$) \cdot (3.5$ s$) \approx 4 \times 10^8$/cm^3. This approximate figure represents 5×10^{-4} of all the molecules exhausted from the engine, which is in the range expected for "trace" combustion species.

Such very low absolute concentrations relative to ambient O (see Figure 3) show that the luminescence-producing reactant being depleted is XAlO (or its precursor). Furthermore the measured radiances are so high as to rule against a significant contribution from reactions involving minor atmospheric species, such as O_3. We note also that the resulting concentrations of ground-state AlO_2 are orders of magnitude to low to make the exhaust volumes optically thick to the multiple overlapping band radiations; the obvious limb brightenings are further evidence that the wake glow is optically thin (as initially assumed).

A comparable number of ~11-μm asymmetric-stretch (ν_3) cascade photons would also be emitted, since a large fraction of the transitions to the ground electronic state of AlO_2 would terminate on vibrationally excited levels. Thus this LWIR radiance component is of order 2×10^{-10} W/cm^2 sr even when direct chemical production of high vibrational states of $AlO_2(\tilde{X})$ is neglected. However as the rate of pumping of $AlO_2^\dagger$ by earthshine and solar radiation is low due to the small oscillator strengths of its vibrational fundamentals (for 001-000, ~10^{-7}), persisting infrared background from this species would be weak.

5.0   CONCLUDING COMMENTS

Chemiluminescent reactions of an incompletely identified polyatomic minor species present in their exhaust gas is the source of the ~10-s persisting visible wake trails from the Strypi-XI's solid thrusters as they traverse the oxygen atom-rich lower thermosphere. A similar glow along the trajectory of (at least) one further broadly similar rocket engine has also been photographed, and may be common to aluminum-granule fuel propellants. The photon yields would of course depend on the output of these reactant(s) from the high-temperature combustion (or from later reactions among the somewhat-cooled exhaust gases). For Antares the fractional concentration of this chemiluminous species is about 5×10^{-4} and the time-integrated energy yield (including that from the near-IR and -UV transitions in the quasicontinuum from AlO_2^*) is 0.15%, with estimated accuracy $\pm$ a factor 2½.

The lateral dimensions of such glows scale to the power output and pressure altitude of the rocket motor roughly as predicted from "similarity" hydrodynamics of static explosions in the high atmosphere. Surface brightnesses of the wake trail are controlled by reactive flow of the combustion gas and the ambient O(^{3}P) atoms, which are pushed out by the exhaust of full

87   15

engine burn but are almost immediately intermixed with exhaust from engine smolder [at the altitudes of the two rockets' operation]. The Antares developed a broad, irregular luminous region surrounding the ~2 km of its flight path just after ignition (most probably stemming from engine startup transients), and later showed a relatively smooth and stable column along its trajectory (and also extending several km in the retrograde direction). Quite obvious limb enhancements and longer than "chemical" decay times of the surface radiances are due to sweepout of the atmospheric reactant by the denser, directed combustion-product gas.

The absolute visible radiances that we measured from the ground station, with the lower blue-near ultraviolet radiances from the spaceborne camera, are consistent with the interpretation that AlO_2 ($^1B_2$) molecules are responsible for the luminosity. The absolute brightnesses and the rates of emission per unit axial length indicated in Figure 11 quantify the far-field scene presented by the Antares operation to surveillance/tracking sensors between 0.38 and 0.67 μm, and form a basis for estimating the accompanying radiant intensities from AlO_2 at infrared wavelengths. Since the optical yield rates depend on the altitude profile of [O], they would vary with geophysical conditions; furthermore they show some evidence of a kinetically complex dependence on air density, probably due to quenching of AlO_2^*. Their scale times would later decrease, by somewhat less than an order of magnitude, as the emission process becomes dominated by chemical reactions rather than physical transport, as is the case at very early times in the less dense wake from the Antares after-burn.

The amplitudes and characteristic scale lengths of the variations in visible radiance ("clutter") can be directly taken from these AMOS video images, and also would apply to the spatially-congruent infrared radiations. In addition straightforward extension of the hydrodynamic calculations applied here would provide the distributions in space and time of density and temperature of the combustion gases, which with their relative concentrations of the several infrared-active molecules listed in Table 2 leads directly to the thermal spectral radiances of the rocket-exhaust volumes. That is, "calibration" of the cylindrical-symmetry reactive flow model from these visible-emission data applies in determining the persisting infrared signature of the trail left by the Strypi-XI (and similar) solid thruster engines.

Experiments over a broader range of solid composite rocket operation and smolder altitudes, with much longer-duration staring-by wider-field cameras--plus, of course, measurement of the emission spectrum--, would further validate the dependence of the radiance distributions and lifetimes on [O], total air density, and thruster power output.

7.0   ACKNOWLEDGMENTS

8.0 REFERENCES

1. Erdman, P. W., E. C. Zipf, P. Espy, C. Howlett, R. Loda, R. J. Collins, D. A. Levin, and G. V. Candler, "Flight Measurements of Low Velocity Bow Shock Ultra-Violet Radiation", Paper AIAA 91-1410, *26th AIAA Thermophysics Conference*, Honolulu HI, June 1991.

2. Levin, D. A., L. H. Caveny, D. M. Mann, R. J. Collins, C. Howlett, P. Espy, R. W. Erdman, and E. Zipf, "Ultraviolet Emissions from In-flight Plume and Hardbody Flow Fields", *19th JANNAF Exhaust Plume Technology Conference*, 1991.

3. *AMOS User's Manual*, Revision 7, AERLM 1175, Avco Corp., Everett MA, 1989.

4. Murad, E., D. J. Knecht, R. A. Viereck, C. P. Pike, I. L. Kofsky, C. A. Trowbridge, D. L. A. Rall, G. Ashley, L. Twist, J. B. Elgin, A. Setayesh, A. T. Stair, Jr., and J. E. Blaha, "Visible light emission excited by interaction of space shuttle exhaust with the atmosphere", *Geophys. Res. Lett.* 17, 2205-2208, 1990.

5. Kofsky, I. L., D. L. A. Rall, M. A. Maris, N. H. Tran, E. Murad, C. P. Pike, D. J. Knecht, R. A. Viereck, A. T. Stair, Jr., and A. Setayesh, "Phenomenology of a water venting in low earth orbit", *Acta Astronautica* 26, 345-347, 1992.

6. Candler, G., D. A. Levin, J. Brandenburg, R. J. Collins, P. W. Erdman, E. C. Zipf, and C. Howlett, "Comparison of Theory with Plume Radiance Measurements form the Bow Shock Ultraviolet 2 Rocket Flight", Paper AIAA 92-0125, *30th Aerospace Sciences Meeting*, Reno NV, Jan 1992.

7. Erdman, P. W., E. C. Zipf, P. Espy, C. Howlett, R. J. Collins, C. Christou, D. A. Levin, and G. V. Candler, "In Situ Measurements of UV and VUV Radiation from a Rocket Plume and Re-Entry Bow Shock", Paper AIAA 92-0124, *30th Aerospace Sciences Meeting*, Reno NV, Jan 1992.

8. O'Neil, R. R., F. Bien, D. Burt, J. A. Sandock, and A. T. Stair, Jr., "Summarized results of the artificial auroral experiment, Precede", *J. Geophys. Res.* 83, 3273-3280, 1978.

9. Shorr, M., and A. J. Zahringer (eds.), *Solid Rocket Technology*, Wiley, New York, p. 367, 1967.

10. Hedin, A. E., "MSIS-86 thermospheric model", *J. Geophys. Res.* 92, 4649-4662, 1987.

11. Smathers, H. W., D. M. Horan, J. G. Cardon, E. R. Malaret, M. Singh, T. Sorensen, P. Laufer, M. Corson, J. A. McKay, and R. R. Strunce, Jr., *Naval Research Laboratory Draft Strypi Report* "Ultraviolet Plume Instrument Observations from Space: Strypi Rocket Plume", 28 October 1991.

12. Warren, Jr., W. H., "Documentation for the machine-readable character-coded version of the SkyMap Catalogue", NASA Report NSSDC/W DC-A-R&S, 05 July 1981.

13. Groves, G. V., "Initial expansion to ambient pressure of chemical explosive releases in the upper atmosphere", *J. Geophys. Res.* 68, 3033-3047, 1963.

14. NOAA/NASA/USAF, *U. S. Standard Atmosphere, 1976,* Washington DC, p. 7, 1976.

15. Golomb, D. and M. A. MacLeod, "Diffusion coefficients in the upper atmosphere from chemiluminous trails", *J. Geophys. Res.* 71, 2299-2305, 1966.

16. Bernhardt, P. A., "High altitude gas releases: Transition from collisionless flow to diffusive flow in a nonuniform atmosphere", *J. Geophys. Res.* 84, 4341-4354, 1979.

17. Bernhardt, P. A., B. A. Kashiwa, C. A. Tepley, and S. T. Noble, "Spacelab 2 upper atmospheric modification experiment over Arecibo, 1, Neutral gas dynamics", *Astrophys. Lett. Comm.* 27, 169-184, 1988.

18. Hoffman, H. S. and G. T. Best, "The initial behavior of high altitude barium releases—II. The expanding vapor cloud", *J. Atm. Terr. Phys.* 36, 1475-1486, 1974.

19. Rosenberg, N. W., "Chemical releases at high altitude", *Science* 152, 1017-1027, 1966.

20. Brode, H. L., "Blast wave from a spherical charge", *Phys. Fluids* 2, 217-229, 1959.

21. Brode, H. L., "Analysis of gas expansion in a rarefied atmosphere", *Phys. Fluids* 15, 1913-1917, 1972.

22. Klein, M. M., "Similarity solution for cylindrical gas cloud in rarefied atmosphere," *Phys. Fluids* 12, 964-965, 1968.

23. Slanger, T. G. and J. Black, "Reaction rate measurements of $O(^3P)$ atoms by resonance fluorescence II, $O(^3P) + CO + M \rightarrow CO_2 + M$; M = He, Ar, N_2", *J. Chem. Phys.* 53, 3722-3728, 1970.

24. Rosenberg, N. W., D. Golomb, and E. F. Allen, Jr., "Chemiluminescence of trimethyl aluminum released into the upper atmosphere", *J. Geophys. Res.* 68, 5895-5898, 1963.

25. Oblath, S. B. and J. L. Gole, "On the continuum emissions observed upon oxidation of aluminum and its compounds", *Combustion and Flame* 37, 293-312, 1980.

26. Golomb, D. and J. H. Brown, "Chemiluminescence of trimethyl aluminum in active oxygen and nitrogen", *Combustion and Flame* 27, 383-389, 1976.

TABLE 1.   STRYPI-XI TRAJECTORY PARAMETERS

Time [s]	Range [km][a]	Altitude [km]	Elevation [deg][a]	Azimuth [deg][a]	Aspect [deg][a]	Velocity [km s^{-1}]
150.0	457.6	104.4	9.4	290.0	43.1	0.317
155.1 - 0[b]	448.4	105.2	10.1	290.0	38.9	0.310
160.0	439.2	105.8	10.7	289.2	35.1	0.391
170.0	421.2	106.7	12.1	287.5	35.1	0.904
180.0	403.5	108.2	13.4	285.6	36.8	1.618
190.5 - 35.4[b]	386.2	110.9	14.6	283.6	39.3	2.567
205.0[c]	361.1	115.3	16.5	280.0	43.7	2.621
239.0[d]	308.8	118.8	19.9	269.7	57.7	2.616
245[e]	300.4	118.4	20.4	267.4	61.6	2.836
260.0[f]	281.4	116.5	21.3	261.2	75.8	3.65

[a]From AMOS [b]Antares ignition and burnout [c]After-burn, Figure 11
[d]Star 27 ignition [e]Star 27, Figure 13 [f]Camera tracking ends

TABLE 2. CHARACTERISTICS OF THE STRYPI-XI ROCKET ENGINES

	Antares II	Star 27
a) Dimensions		
Diameter of exit plane	68.6	48.6 cm
Effective half-angle of nozzle exit cone	15	17.2 °
b) Propellant (manufacturers' data)		
Grain segment pattern	2 x 120° & 60°	8 x 45°
Composition, nominal weight percent		
Al, *fuel*	20.6	16.0
Ammonium perchlorate, *oxidizer*	7.5	72.0
Cyclotetramethylynetetranitramine, *oxidizer*, HMX	15.0	
Nitrocellulose, *oxidizer-binder*	22.5	
Nitroglycerine, *oxidizer-plasticizer*	26.3	
Carboxy-terminated polybutadiene, *binder*		12.0
Triacetin, resorcinol, and 2-Nitro-diphenylamine, *plasticizer and stabilizer*	8.1	
c) Exhaust (calculated)		
Temperature at exit plane	2139	1507 K
Average mass outflow rate	33.3	9.81 kg/s
Molecule exhaustion rate per cm path	2½ x 10^{21}	7½ x 10^{20}
Composition, moles/100 g of propellant		
Al_2O_3 (particles)	0.367	0.297
CO	1.392	0.763
H_2 (H)	0.985 (0.018)	0.932
N_2	0.513	0.310
H_2O	0.171	0.630
HCl	0.060	0.608
CO_2	0.043	0.096
$AlCl_3$, AlCl, AlO, Al_2O, OH,...		*See text*
d) Performance		
Duration of burn (measured)	35	34 s
Average thrust (measured)	9370	2680 kgf
Exhaust velocity (calculated as thrust/mass loss rate)	2.65	2.93 km/s

19

2 s, 105.4 km

Profile (-3 s)

6 s

Fig. 4

Lower Edge

4 s

Fig. 4

16 s, 106.8 km

8 s

Fig. 9,10,11

10 s

Fig. 7

14 s

49 s

Fig. 12

35 s, 110.9 km
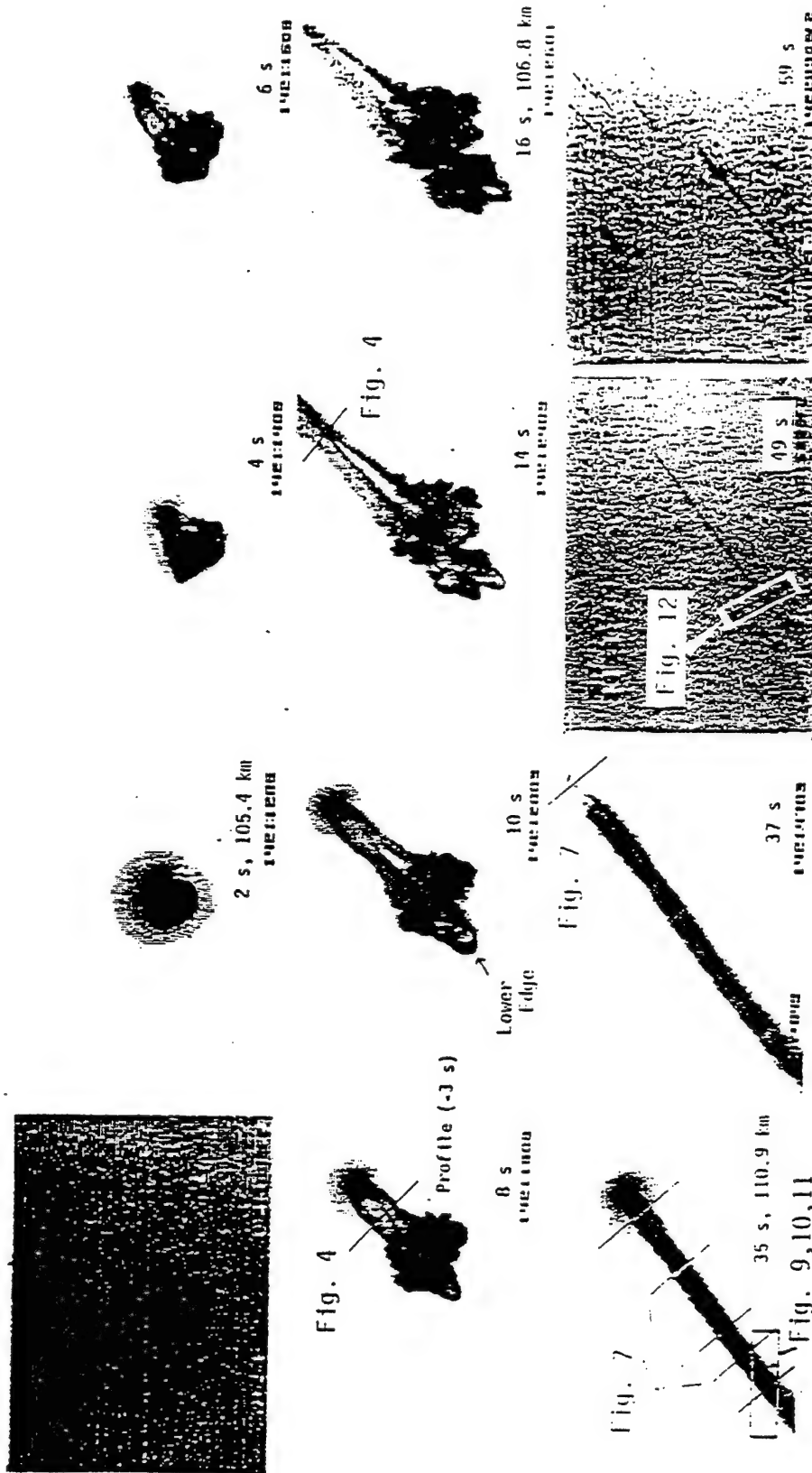
Fig. 7

37 s

59 s

Figure 1.   Montage of video photographs of the luminous wake trail left by the Antares IIa rocket engine.   (The glow from the lower thrust Star 27 was qualitatively similar.)   The diagonal field of view perpendicular to the line of sight is 23.5 km at ignition, and decreases to 18 km in the final frame shown; as the camera is on an AMOS astronomical mount, the angle between the bottom of the field and local horizontal changes from 75° to 83° over this period (the foreshortened trajectory is toward the camera's upper left; see Figure 2).   At 16 s after ignition the camera begins to track to maintain the rocket body within its field of view, so that the initial irregular emitting region goes below the field.   Photocurrents from the traces or image areas indicated are shown in Figures 4, 7, 9, 10, 11, and 12.

20

92
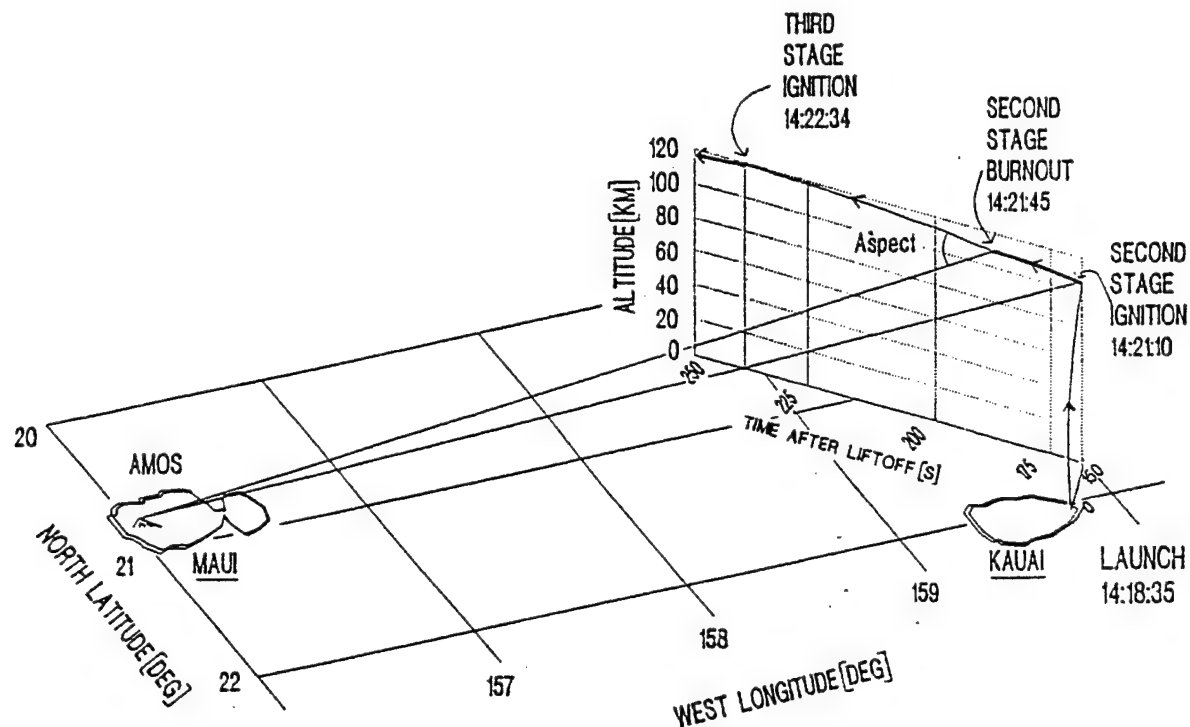
Figure 2. South-looking view of the trajectory of the Strypi-XI with the projection from AMOS.
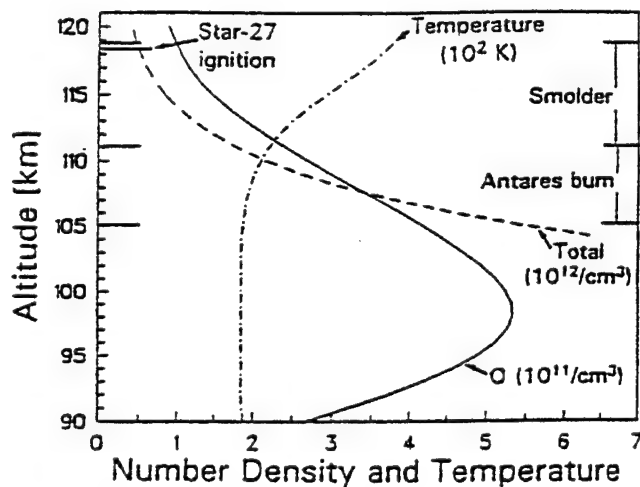
Figure 3. Atmospheric species concentrations and temperature during the Bow Shock 2/UV Diagnostic Experiment.
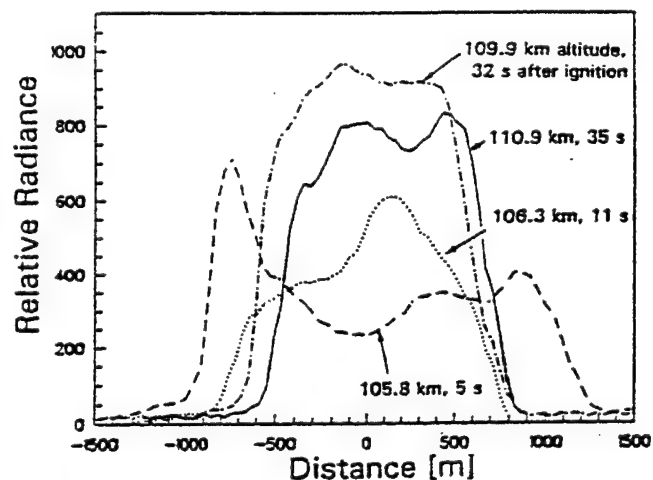
Figure 4. Crosswise photocurrent profiles 3 s after passage of the Antares thruster engine, normalized to fixed camera gain. The times stated refer to this passage. Representative trace lines are indicated on the images at 8 and 14 s after ignition (which refer to 5 and 11 s in Figure 4) in Figure 1.
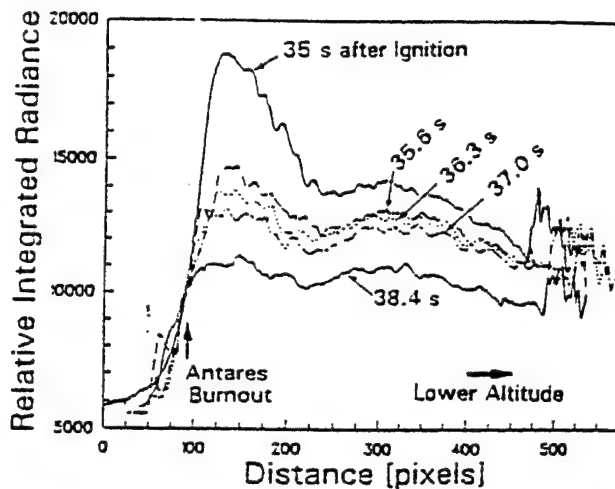
Figure 5. Transverse-summed photocurrent profiles along the long axis of the Antares exhaust trail, starting near engine burnout. The broad peak in the image at 35 s is thermal radiation from the condensed Al_2O_3 exhaust particles.
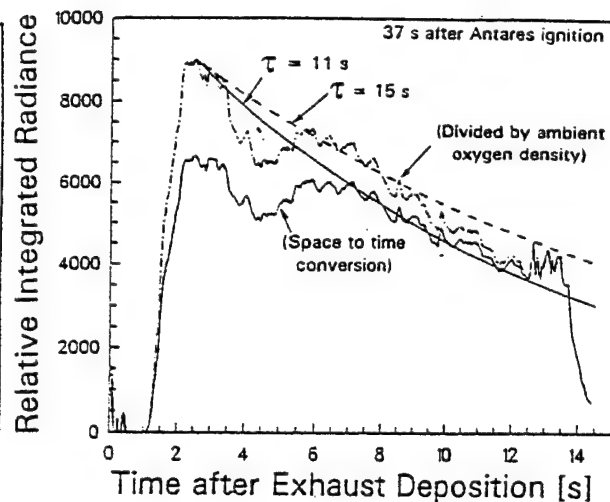
Figure 6. Longitudinal summed-photocurrent profile at 37 s corrected to derive an effective exponential lifetime of the total emission rate per unit path averaged over 108.2 – 110.9 km altitude.
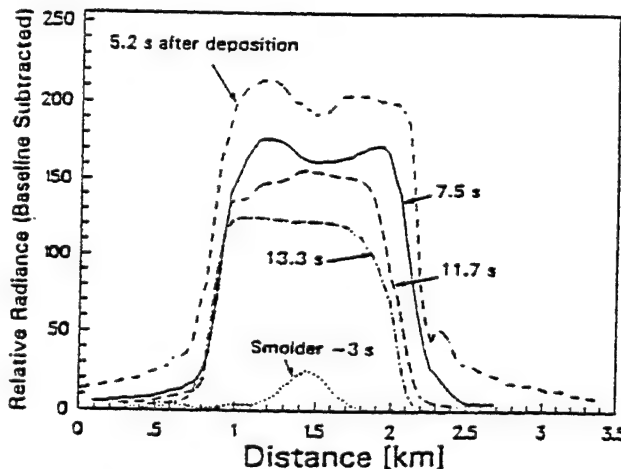
Figure 7. Transverse photocurrent traces across the Antares trail at 35 s after ignition. Smolder refers to 1 s after Antares burnout (111 km altitude).
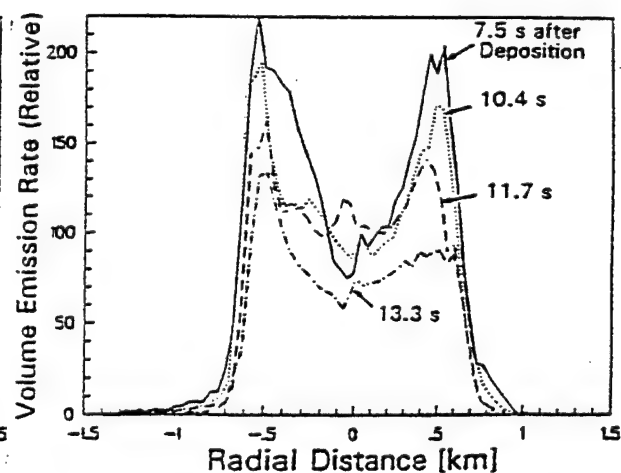
Figure 8. Volume emission from Abel inversions of the photocurrent traces in Figure 7.

94
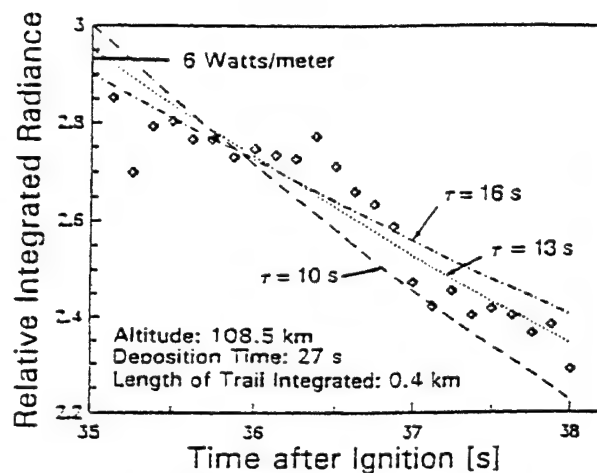
Figure 9. Spatially-summed photocurrents in the fixed rectangular image area near the bottom of the trail indicated in Figure 1 (altitude range 108.4 ± 0.2 km), with exponential lifetimes indicated.
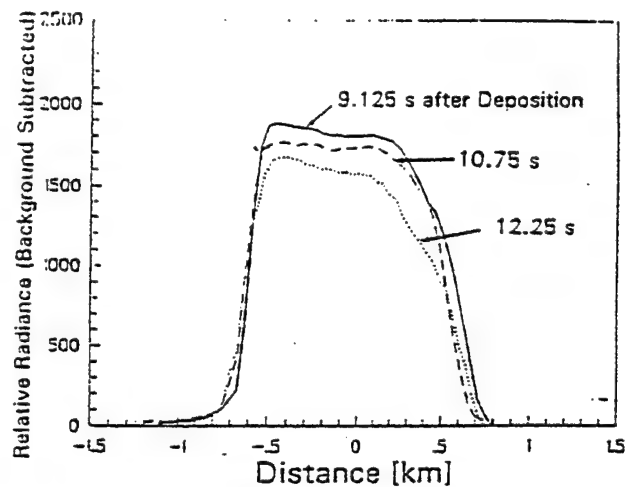
Figure 10. Transverse photocurrent traces across the Antares trail at 108.2 km altitude at three times after rocket passage.
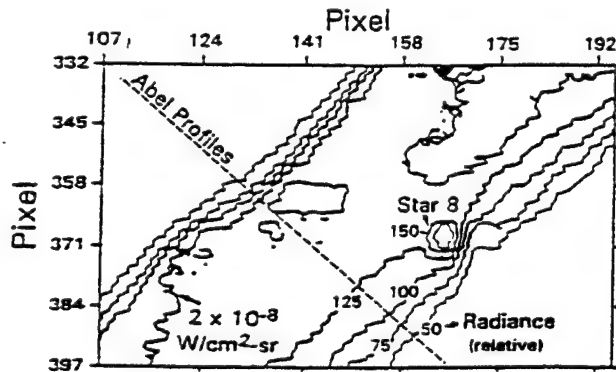

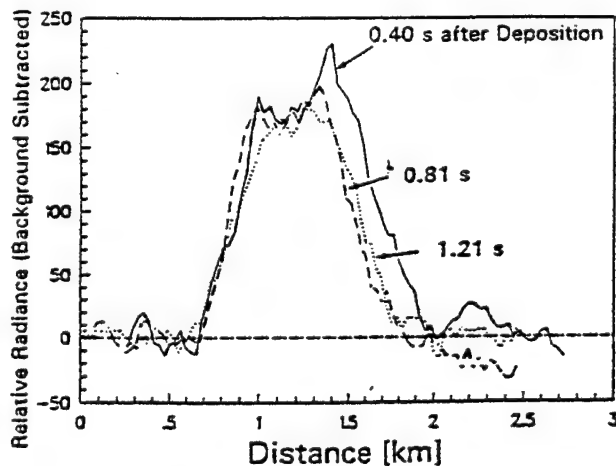Figure 11. Equi-photocurrent contour plot of the region of Antares image within the rectangular area centered at 108.4 km, at 37 s. The contour interval is 25 (of 255) units.

Figure 13. Transverse photocurrent traces across the Star 27 wake trail at three times after rocket passage (altitudes 118.6 – 118.4 km).
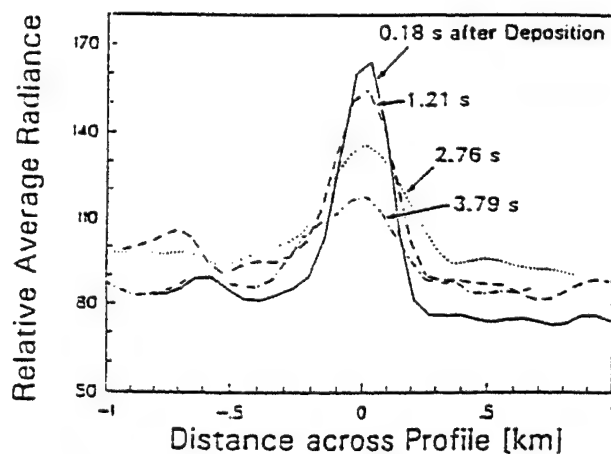
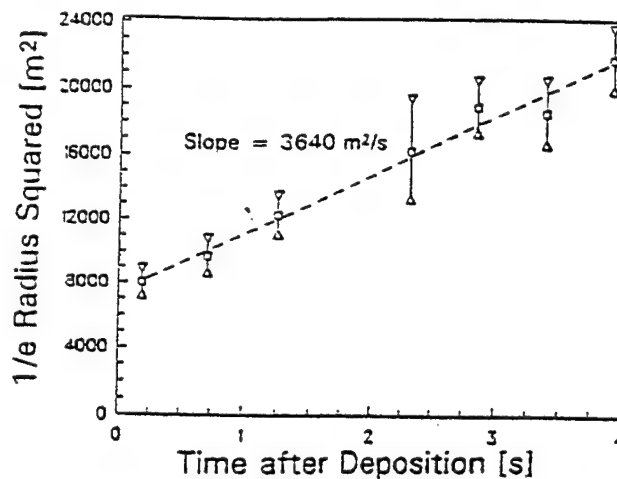Figure 12. a) Photocurrent traces in the Antares smolder area at 114.5 km. (See Figure 1)

Figure 12. b) Square of widths at 1/e-maximum photocurrents at 114.5 km, with a least-squares straight line best fit (the triangles represent 1σ error from a regression analysis).
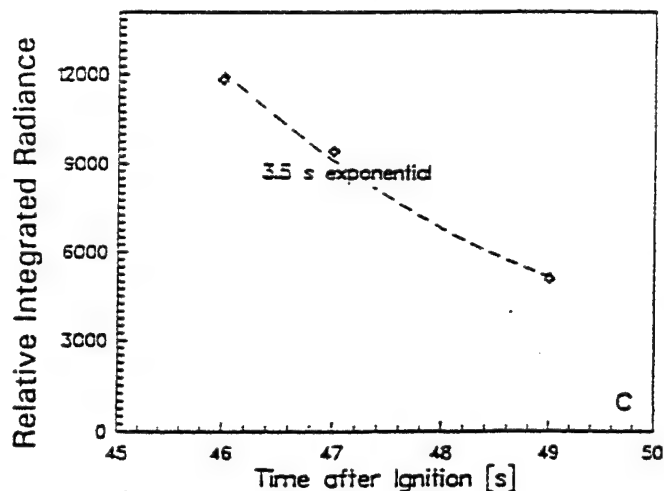
Figure 12. c) Total emission rate per unit length along the trajectory path of the Antares smolder.

Figure 14. Relative spectral response (in photon units) of the instruments used to view the Antares trail compared with the spectrum of emission from the reaction of tri-methyl aluminum with atomic oxygen[26]. The camera spectral response includes the LOWTRAN atmospheric transmission from space to AMOS used in the data analysis.
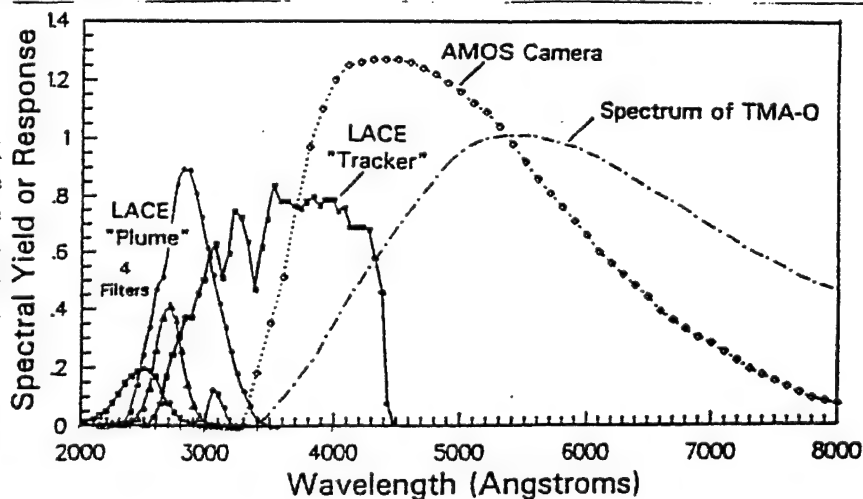
APPENDIX C

APPLICATION OF GLO TO CHARACTERIZING OPTICAL RADIATIONS ASSOCIATED WITH THE "MIR" MANNED SPACECRAFT

Rendezvous of Shuttle Orbiter with MIR provides an opportunity to measure the spectral and spatial distributions of spacecraft glows resulting from impingement of ambient and control-jet gases on exposed vehicle surfaces, determine the albedo and photometric function of aged on-orbit surface elements, and otherwise characterize the optical signature of a particular type of long-lived near-space object. In planning operation of the GLO sensor for this purpose we considered the elevation and azimuth of the Sun and Moon relative to the planned rendezvous and docking trajectory. Typical projections of the multi-channel spectrograph slits on MIR are illustrated in Figure C-1 (the original was in color to emphasize fields of view).
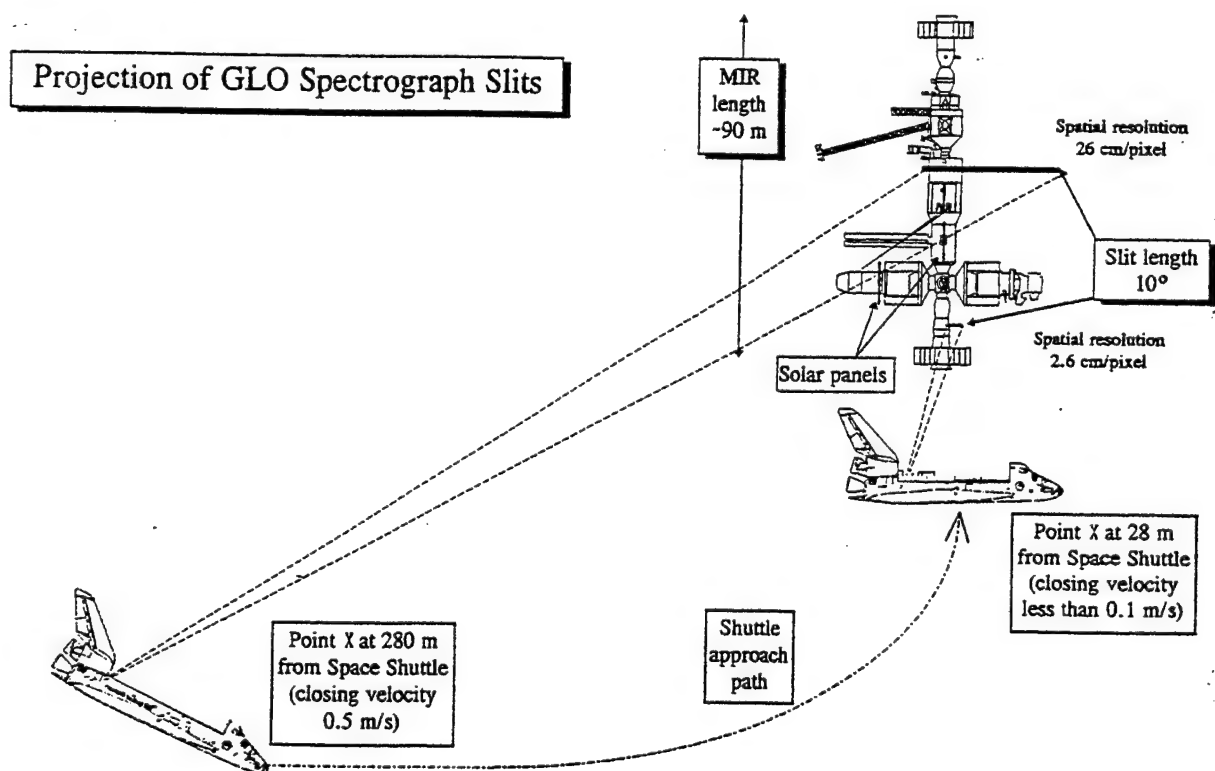

Figure 23. Projection of GLO spectrograph slits at two planned spatial separations from the "MIR" manned spacecraft.

APPENDIX D[*]

GUIDED-ION BEAM MEASUREMENTS OF
THE REACTION OF O^+ WITH C_2H_4 AND C_2D_4

Preliminary results from this laboratory investigation of the reactions of low-concentration fragments and pyrolysis products of thruster rocket fuels with atomic oxygen ions, the most abundant F-region charged species, are summarized here.

Experiment Method

Guided-ion beam technology[78] was applied to measure cross sections, product branching ratios, and product velocity distributions of the reactions of $C_2H_4(D_4)$ with O^+. These ion-neutral systems were studied at collision energies from near-thermal to just above 10 eV, characteristic of the available center-of-mass kinetic energies of low Earth orbit.

The oxygen ions were produced by impact of $\sim$25-eV electrons on CO_2. Thermodynamically, this electron energy is sufficient to cause dissociative ionization of CO_2 to CO and $O^+(^4S)$ (which requires about 19.1 eV), while low enough to minimize production of electronically-excited metastable ground-configuration oxygen ions (^2D, ^2P) that could complicate interpretation of the experiment. The ions are passed through a Wien velocity filter for mass selection, and are then decelerated and injected into two rf octopole electric fields in series; their energy within the injection electrode is kept to less than 1 eV, which aids in preserving the initial half-width of the translational energy distribution, 300-400 meV. A 10 Mhz rf voltage applied to the octopoles creates a cylindrical ion trapping potential. The first octopole field extends through a collision cell containing the $C_2H_4(D_4)$ gas. Product and reactant ions are guided into the second octopole, from which they are extracted and focused into a quadrupole mass analyzer, and then detected with an off-axis channel plate. Reaction cross sections (σ) are determined from the integrated currents I of the reactant and product ions:

$$\sigma = \frac{I_{prod}}{(I_{reac} + \Sigma I_{prod}) \cdot n\ell},$$

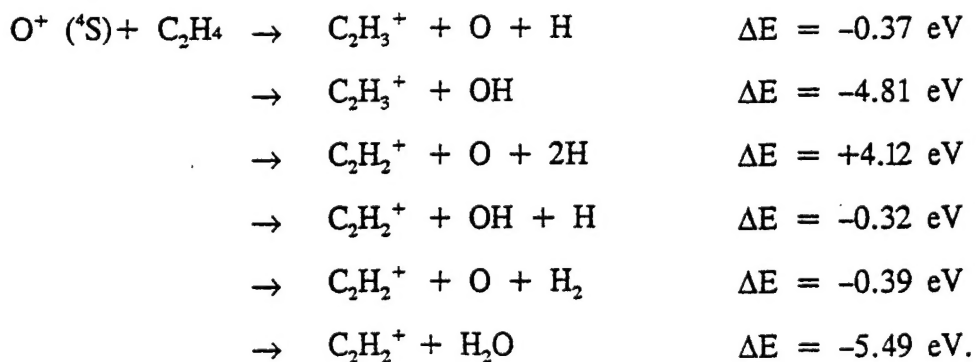where n is the density of target molecules in the cell of length ℓ.

With C_2H_4, primary product ions were observed at mass-to-charge ratios of 26-28. Higher mass ions were also detected, which are provisionally interpreted as corresponding to products of secondary reactions of the $C_2H_n^+$ initially formed with C_2H_4 molecules. These heavier ions were also included in calculating the total empirical cross section, but were not considered in determining branching ratios. While these secondary reactions would be expected to exhibit a different pressure dependence than primary products, within the limited range of accessible gas pressures no clear difference could be detected. Although single-collision conditions prevail for the primary reactant ions throughout the pressure range studied the secondary reactions most notably involve primary product ions formed with very low translational energy, which are rf-trapped in the reaction cell long enough to encounter a second neutral reaction partner. (In general, secondary product ions constituted less than 10-15% of the total.)

Distributions of product ion velocities were measured by time-of-flight methods involving pulsing the reactant ion beam into the collision cell and timing the arrival of product ions at the downstream detector. Times-of-flight were measured for conditions of high rf trapping voltage on the octopoles, so that all product ions are collected, and for low rf voltages, which result in loss of product ions having large transverse velocity components. The difference between the resulting velocity distributions provides an indication of the anisotropy of the angular distribution of the product ions.

Results and Discussion

The reaction of O^+ with C_2H_4 forms three primary ionic products throughout the collision energy range studied, in order of abundance $C_2H_2^+$, $C_2H_3^+$, and $C_2H_4^+$. Formation of $C_2H_4^+$ clearly takes place by charge transfer, and is 3.11 eV exothermic. The other ion species may be formed by either dissociative charge transfer or by hydride transfers. The relevant thermochemistry is[79]

$$
\begin{aligned}
O^+\ (^4S) + C_2H_4 \ &\rightarrow\ C_2H_3^+ + O + H && \Delta E = -0.37\ \text{eV} \\
&\rightarrow\ C_2H_3^+ + OH && \Delta E = -4.81\ \text{eV} \\
&\rightarrow\ C_2H_2^+ + O + 2H && \Delta E = +4.12\ \text{eV} \\
&\rightarrow\ C_2H_2^+ + OH + H && \Delta E = -0.32\ \text{eV} \\
&\rightarrow\ C_2H_2^+ + O + H_2 && \Delta E = -0.39\ \text{eV} \\
&\rightarrow\ C_2H_2^+ + H_2O && \Delta E = -5.49\ \text{eV.}
\end{aligned}
$$

It will be noted that all but one of these reactions are exothermic ($\Delta E > 0$) for ground-state oxygen ions. As the energetics for the several mechanisms that form $C_2H_3^+$ or $C_2H_2^+$ differ strongly, detailed kinetic energy analysis would allow determination of those mechanisms active in the range studied.

Figure 24 shows the partial cross sections for reaction of O^+ with C_2H_4 as a function of collision energy. The total cross section is about 120Å^2 at 0.2 eV, and decreases with approximately an (energy)$^{-\frac{1}{2}}$ dependence until about 1 eV, where it levels off at 80Å^2. The cross sections for producing one of the secondary product ions ($C_2H_5^+$) are included in Figure 24. Only $C_2H_2^+$, which may be formed by four separate mechanisms with very different energetics, shows a significant dependence on collision energy. Its high formation cross section at low energy with negative energy dependence implies that the major reaction pathway is exothermic, i.e., one of the three last listed. The cross section data alone are not sufficient to distinguish among these mechanisms.

The total cross sections for $O^+ + C_2D_4$ (Figure 25), while slightly higher, display similar dependence on energy. The branching ratios, however, are noticeably different from those of the reaction with C_2H_4: $C_2D_4^+$ is more abundant than $C_2D_3^+$ over the full energy range, and is almost as prominent as $C_2D_2^+$. This finding almost certainly results from the primary kinetic isotope effect that favors cleavage of C-H bonds over C-D bonds. The less exothermic reactions would be expected to show stronger kinetic isotope effects than the strongly exothermic other reactions listed. The consistency of these observed isotope effects with the relative rates of the weakly or strongly exothermic reactions can be determined by detailed kinetic analysis.

In both reactions the $C_2H_4(D_4)^+$ ion is the sole product showing significant collision energy dependence. This observation may indicate intermediacy of an ion-molecule complex whose formation is disfavored at higher energies. $C_2H_2(D_2)^+$ and $C_2H_3(D_3)^+$ can be formed exothermically by both long-range change transfer and short-range atom transfer; this last process may also involve a collision complex.

As the cross-section measurements are by themselves insufficient to deduce the reaction pathways, we performed product ion velocity measurements. Times-of-flight were determined for each of the three primary product ions, and converted to axial velocity distributions. An example, for formation of $C_2H_2^+$ at 2.2 eV, is shown in Figure 26. The velocity distributions peak near zero and drop off rapidly, which indicates that the products are formed with relatively little translational energy, as in a long-range (large impact parameter) charge transfer. Similarity between the two distributions further
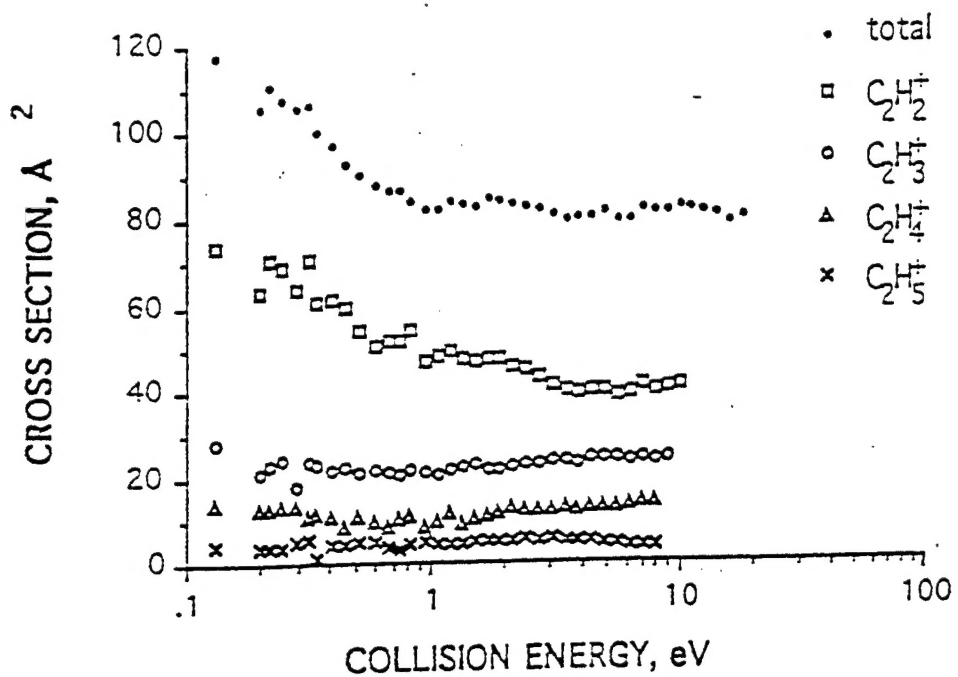
100

Figure 24. Collision energy dependence of the cross sections for reaction of O^+ with
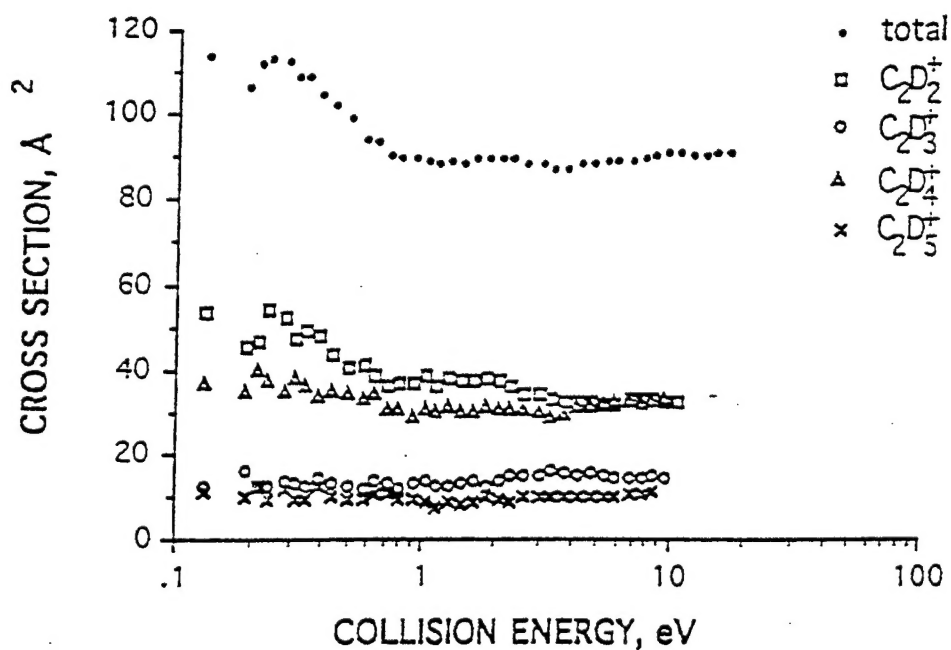

Figure 25. Collision energy dependence of the cross sections for reaction of O^+ with C_2D_4.

indicates that the reaction products are formed with relatively small transverse velocities. Moreover, the shape suggests that the $C_2H_4^+$ products are not formed in long-lived collision complexes, which would result in forward-scattered products with large axial velocities. This finding does not, however, address the intermediacy of long-lived collision complexes in the reaction with C_2H_4; such complexes would lead to formation of $C_2H_3^+$ and $C_2H_2^+$. Further analysis of the velocity distributions for the $C_2H_3^+$ and $C_2H_2^+$ products will contribute to understanding the process(es) by which these product species are formed.
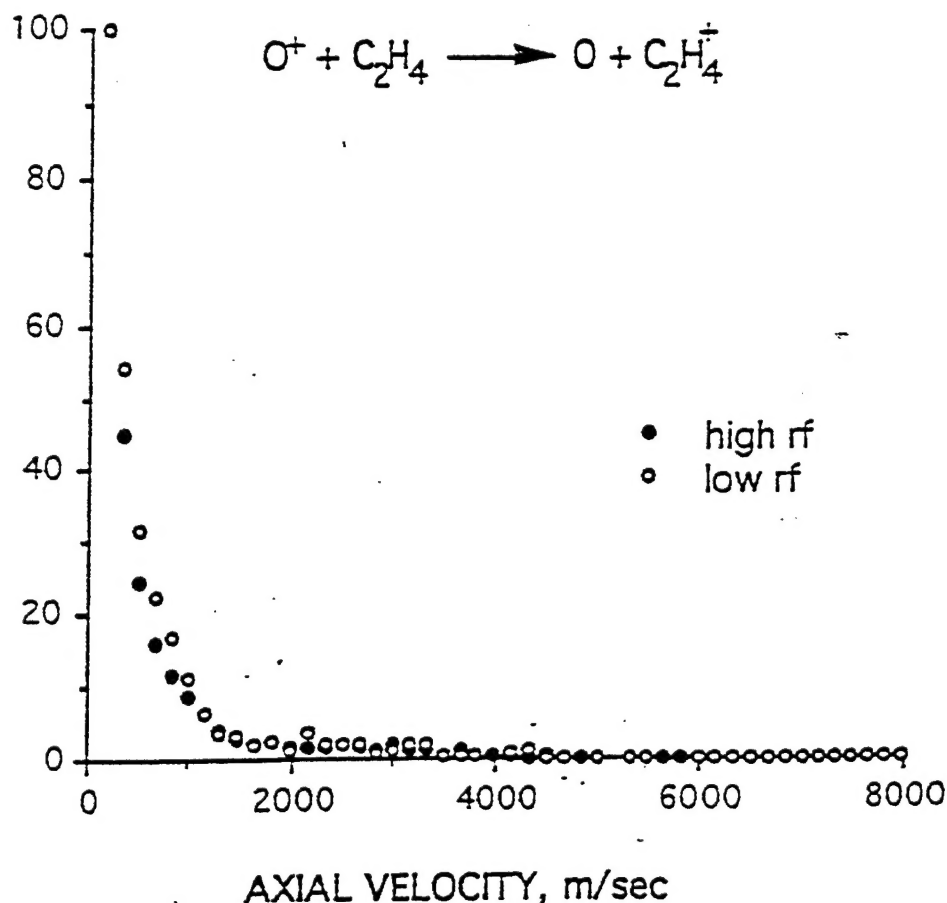

Figure 26. Axial velocity distributions of the $C_2H_4^+$ product from the reaction of O^+ with C_2H_4 at 2.2 eV center-of-mass collision energy. The open circles refer to the measurement at low rf trapping voltage, so that product ions with large components of transverse velocity are inefficiently collected; the closed circles are the measurements with "complete" ion collection.